Master thesis

Is retained austenite controlling the mechanical properties of Q&P steels ?

Written by: Arnold Johannes Kolk
Master student Materials Science and Engineering,
Delft University of Technology

August 2014

Under supervision of: Dr. M.J. Santofimia Navarro & Prof.dr.ir. J. Sietsma

TU Delft Delft University of Technology

Colophon

Printed and distributed by:

A.J. Kolk
Koolmeesstraat 39
3145 NB Maassluis
The Netherlands
a.j.kolk@gmail.com

Delft University of Technology
Faculty Mechanical, Maritime and Materials Engineering (3ME)
Department Materials Science and Engineering
Mekelweg 2
2628 CD Delft
The Netherlands

Illustrations by: A.J. Kolk

Printing: Department of Materials Science and Engineering at the Delft University of Technology

Kolk, Arnold

Is retained austenite controlling the mechanical properties of Q&P steel ?

M. Sc. Thesis, Delft University of Technology

Keywords: Quenching and Partitioning (Q&P) steels, Retained austenite, Mechanical properties ,TRIP-effect, In situ X-ray diffraction

Preface

The thesis presents the results of an investigation into the retained austenite phase controlling the mechanical properties via the TRIP-effect on Quenching and Partitioning (Q&P) steel. The thesis is a contribution to a research project NEWQP (RFSR-CT-2011-00017) of Research Fund for Coal and Steel from the European Commission. This thesis is written by a student with a preceding background in mechanical engineering at different levels (B. Eng. and Technical and Vocational Education and Training (TVET)). This thesis is written for engineers and students with a general understanding of material science.

The writer wants to thanks the following persons for their contribution to this master thesis, Maria Santofimia and Jilt Sietsma for their dedicated supervision, Michael Janssen and Amarante Böttger for being in the graduation committee, Ruud Hendrikx, Niek van der Pers and Richard Huizenga for the setup of the (In situ) X-ray diffraction experiments and feedback on the results, Lie Zhao for his experience of experiments with In situ X-ray diffraction, Farideh Hajy Akbary for her support with the Deben Microtest machine and feedback on the results, Ruud Planken for the fabrication of (temporary) spare parts of the Deben Microtest machine, DEMO for fabrication of the tensile specimens, Sander van Asperen for the tensile (surface) preparation, Pina Mecozzi for her ThermoCalc calculations, Tjerk Koopmans for supplying the Magnetometer results of the materials, Dorien de Knijf for supplying the OCAS material and feedback on the results, Richard Thiessen for supplying the Thyssenkrupp material, and the following persons at the MPMP section of Materials Science and Engineering: Olga, Tungky, Alfonso, Ashwath, Bij-Na, Xiaoqin, Jun, Konstantinos, Gözde, Peter, Roumen, Leo, Erik, Nico, Hans, Ankit, Ron, Pieter, Andrew, Emmy, Janneke, Marios for the good times together.

‘t leven leeft in elke lente voort

Life will live in every spring forth

(N. Benschop, Lentedroom in het park, Met heel mijn hart / druk 1: nagelaten gedichten)

In dierbare herinnering aan:
In loving memory of:

Johannes Bernardus Kolk
*15-03-1943 — †02-05-2006

Abstract

Stronger and more ductile steels are increasingly demanded in important industry sectors such as automotive, gas transport ad power generation. One of the classes of Advanced High Strength Steels (AHSS) that are attracting researchers and industries are the so-called Quenching and Partitioning (Q&P) steels. The microstructure of these steels, formed by laths of low-carbon martensite separated by films of carbon enriched retained austenite, are responsible for these properties. Although both constituents are certainly, steel developers and scientists do not get an agreement about which one of these constituents is actually controlling the response of the material upon deformation.

The way in which retained austenite is believed to contribute to the strain (work) hardening of these steels is via the TRansformation Induced Plasticity (TRIP) effect, by which austenite transforms to martensite during deformation. Therefore, the actual research question is: Is the TRIP-effect playing a role in the response of Q&P steels upon deformation?

The crystal structure of the retained austenite is different from the martensite, and these differences can be detected with X-ray diffraction. In this project, the evolution of the crystal structure of different Q&P specimens were studied in Situ using a X-ray diffraction meter equipped with a micro-tensile tester and if necessary a sample heater. The formation of martensite during the tensile tests was divined form the decrease of austenite diffraction peaks. These experiments allowed detecting the possible occurrence (or absence) of the TRIP-effect.

Table of Contents

List of symbols

Symbol:		Unit:
α	Ratio between fillet zone elongation and the parallel zone elongation	-
α'	Martensite phase	-
β	Constant	-
γ	(Retained) Austenite phase	-
γ_0	Magnitude of the shear	-
ε	Engineering strain	N/m^2
ε_c	Critical strain	N/m^2
ε_n	Normal dilation	-
ϵ	True strain	N/m^2
$\epsilon_{1,2}$	True strain at two intervals	N/m^2
Δa	Lattice parameter reduction	10^{-10} m (Å)
Δf^{γ}	Difference between initial retained austenite volume fraction and austenite volume fraction at QT	[-]
ΔG^{ch}	Chemical driving force	J/mol
$\Delta G_T^{\alpha' \rightarrow \gamma}$	Gibbs free energy difference between the martensite(α') phase and the retained austenite(γ) phase	J/mol
$\Delta G^{\gamma \rightarrow \alpha'}$	Gibbs free energy difference between the retained austenite(γ) phase and the martensite(α') phase	J/mol
$\Delta G_{M_s}^{\gamma \rightarrow \alpha'}$	Gibbs free energy difference between the retained austenite(γ) phase and the martensite(α') phase at M_S temperature	J/mol
$\Delta G_T^{\gamma \rightarrow \alpha'}$	Gibbs free energy difference between the retained austenite(γ) phase and the martensite(α') phase at a temperature between M_S and M_s^{σ}.	J/mol
ΔG^{σ}	Mechanical driving force	J/mol
Δl_f	Elongation of tensile specimen parallel zone part	m
$\Delta \mathrm{l}_m$	Elongation of Deben Microtest machine	m
Δl_p	Elongation of tensile specimen filled zone part	m
$\Delta\sigma$	Stress step	N/m^2
θ	Bragg angle	°
λ	Wavelength	10^{-10} m (Å)
$\sigma_{1,2}$	True stress	N/m^2
σ_e	Engineering stress	N/m^2
σ_n	Resolved shear stress normal to invariant plane	N/m^2
τ_s	Resolved shear stress along invariant plane	N/m^2
K_1	Empirical fitting constant	-
a	Lattice parameter	10^{-10} m (Å)
a_0	Lattice parameter of unalloyed retained austenite phase	10^{-10} m (Å)
K_2	Empirical fitting constant	-
b	Burgers vector	m
A	Temperature per carbon concentration	-
A_{gt}	Total extension at maximum force	-
A_t	Total extension at maximum fracture	-
B	Prefactor grain volume term	-
d_{hkl}	Spacing between atomic planes	10^{-10} m (Å)

d_γ	Average austenite grain size diameter	10^{-6} m (μm)
e_t	Elastic deformation	-
E	Young's modulus	N/m^2
f	First detectible martensite phase fraction	-
$f^{\alpha'}$	Martensite volume fraction	-
f^{γ}	Retained austenite volume fraction	-
f_0^{γ}	Initial retained austenite volume fraction	-
I	Net area intensity	Cps *2θ
$I_{corrected}$	Corrected net area intensity	Cps *2θ
$I_{measured}$	Measured net area intensity	Cps *2θ
$I_{hkl}^{\alpha'}$	Net area intensity of the martensite phase with a specific plane	Cps *2θ
I_{hkl}^{γ}	Net area intensity of the retained austenite phase with a specific plane	Cps *2θ
G	Shear modulus	N/m^2
hkl	Miller index of specific plane	-
k_p	Stability of retained austenite due to deformation	-
K_f	Stiffness of tensile specimen filled zone part	N/m
K_m	Stiffness of Deben Microtest machine	N/m
K_p	Stiffness of tensile specimen parallel zone part	N/m
L	Parameter related to the austenite grain	
m	Aspect ratio of the martensite plate	-
M_d	Strain-induced martensite start temperature	K or °C
M_S	Martensite start temperature	K or °C
M_S^0	Martensite start temperature where the austenite grain has a infinite grain size	K or °C
M_{S0}	Martensite start temperature with dependence on alloying elements or internal stress	K or °C
M_s^{σ}	Stress-assisted martensite start temperature	K or °C
n	Instantaneous strain hardening	-
$n_{1,2}$	The number of intensity peaks for selected phase	-
$n_{\alpha'}$	Total amount of martensite intensity peaks	-
n_{γ}	Total amount of retained austenite intensity peaks	-
p	Autocatalytic effect of martensite nucleation	-
Pt	Partitioning time	sec
PT	Partitioning temperature	K or °C
$P_{hkl}^{\alpha'}$	Texture parameter for the martensite phase with a specific plane	-
P_{hkl}^{γ}	Texture parameter for the retained austenite phase with a specific plane	-
$R_{\alpha'}$	Calculated net area intensity of martensite phase for all planes	Cps *2θ
$R_{hkl}^{\alpha'}$	Calculated net area intensity of martensite phase with a specific plane	Cps *2θ
R_{γ}	Calculated net area intensity of retained austenite phase for all planes	Cps *2θ
R_{hkl}^{γ}	Calculated net area intensity of retained austenite phase with a specific plane	Cps *2θ
R_a	Surface roughness	10^{-6} m (μm)

R_m	Ultimate tensile stress	N/m^2
$R_{p\,0,2}$	Yield stress	N/m^2
T	Temperature	K or °C
T_0	Temperature at which the Gibbs free energy of retained austenite(γ) phase and the martensite(α') phase are in equilibrium	K or °C
U'	Mechanical energy	J/mol
$U'_{strain-induced}$	Strain-induced mechanical energy	J/mol
$U'_{stress-assisted}$	Stress-assisted mechanical energy	J/mol
v	Poisson's ratio	-
V_γ	Average austenite grain volume	
QT	Quenching temperature	K or °C
X_c	Fraction of carbon	Mol or mass%

List of figures

List of tables

1. Introduction

The automotive industry is one of the main industries developing new steel types. The main desirable improvement is the reduction of the mass of the car body shell without sacrificing the mechanical properties. This is because the reduction of the mass of the body shell will increase the fuel efficiency of the car. In order to reduce the mass of the body shell while maintaining the mechanical properties of the body shell an improvement of the material performance is needed. The mechanical properties which are related to the strength and elongation of the material that the material can withstand was a choice between the two parameters (strength or elongation). The industry is developing new types of steels so called Advanced High Strength Steels (AHSS) to improve the material performance. The AHSS materials will increase one of these parameters (strength or elongation) without of sacrificing the other.

One of the new AHSS types is Quenching and Partitioning (Q&P) steels where phase transformation are playing a key role for improving both the mechanical properties of steel. The microstructure of Q&P steels contains two phases: retained austenite and martensite phases. In Q&P steels the retained austenite is a metastable phase which can transform to the martensite phase. To start this transformation a minimum mechanical deformation (energy) for the retained austenite phase is required. This effect of applying a mechanical deformation on the retained austenite phase to initiate a phase transformation to the martensite phase is called the TRIP-effect, which is an abbreviation of TRansformation Induced Plasticity effect.

To study if the TRIP-effect (phase transformation) is playing a role in improving the mechanical properties of the material In situ X-ray diffraction is applied. In this way a mechanical deformation is applied with a tensile machine on the material to acquire an phase transformation which can be studied with X-ray diffraction. The tensile machine will apply the mechanical deformation to obtain a stress-strain curve. At a certain stress level intervals the retained austenite and martensite volume fraction are measured to determine if there is a decrease of the retained austenite phase and an increase of the martensite phase.

In this thesis a background of the Q&P steels, martensitic formation, the Q&P heat treatment and the phase transformation occurring during TRIP-effect are given in chapter 2. In chapter 3 the experimental setup of the In situ X-ray diffraction experiment are described in detail. Chapter 4 represents the results of the In situ X-ray diffraction experiment and discusses the In situ X-ray diffraction experiments results and the interpretation. Chapter 5 presents the conclusion and the recommendations.

2. Background

2.1. Introduction

The automotive industry is the second largest (after the construction) consumer of steel [1]. The aim for the automotive industry and specific the car industry is to manufacture more energy efficient vehicles. In order to have an energy reduction (in the terms of manufacturing and consumption) the industry is reducing the mass of the body shell of the vehicles. The body shells are made from thinner sheets of steel and to have the same structural integrity the steels used must have improved mechanical properties. In steels there is a trade-off between two mechanical properties: strength and elongation. If one of these mechanical properties is increased the other will be deceased.

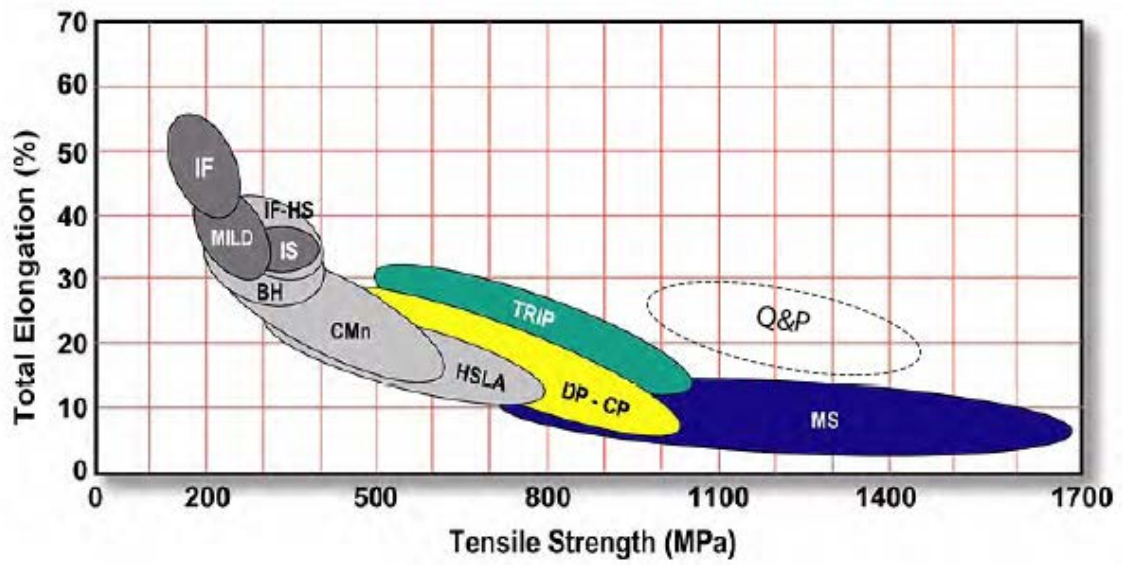

Figure 2.1: Steel diagram strength vs. elongation (obtained from [1] and adapted)

In steels different microstructural phases will give different mechanical properties to the steel. Different microstructure are obtained through different heat treatments. The objective is to enhance mechanical properties of the steel so that there is a maximum strength and maximum elongation(strain). figure 2.1 shows the relation between the elongation and the tensile strength of Advanced High Strength Steels (AHSS): dual phase (DP), transformation-induced plasticity (TRIP), complex phase (CP), and martensitic steels (MS) which have increased the mechanical performance of the steels. Now Q&P steels are researched to increase both of these mechanical properties.

2.2. The Q&P process

To obtain the desired microstructure of the Q&P steel a specific heat treatment is used. This particular heat treatment can be seen in figure 2.2.

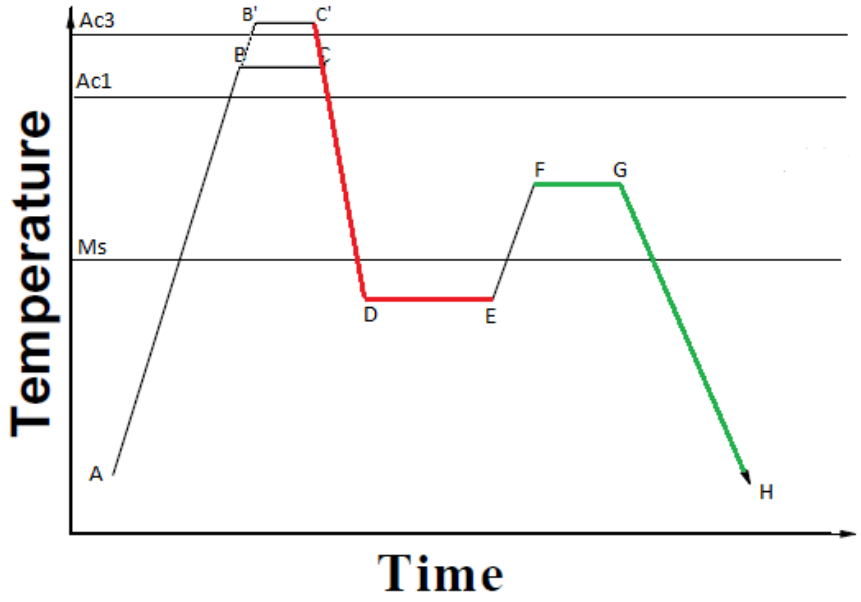

Figure 2.2: Heat treatment process Q&P.

The heat treatment starts at point A with a temperature increase to point B or B'. Where at point B the steel has a partial austenite phase and at point B' it has the full austenite phase. The quenching step is indicated by the red line in figure 2.2. From point C to D there is quenching or rapid cooling of the metal below the M_S temperature. Point D is called the quenching temperature (QT). In Q&P steels the time between points D to E is very short, otherwise martensite (α') phase will growth and this is not desirable. The time between points F to G is the partitioning time (Pt) and at the partitioning temperature (PT) there is carbon diffusion from the martensite phase to the austenite phase. The PT is always at or above the M_S temperature otherwise martensite volume fraction will growth and this is not desirable. Then there is a second quench from points G to H where point H is at room temperature (RT). The isothermal quench step between points C or C' and E is called the quenching step and the isothermal step between points F and G is called the partitioning step the green line in figure 2.2.

2.3. The quenching step

The quenching step in the Q&P steel heat treatment is to produces a microstructure which contents the austenite phase and the martensite phase. To acquire the martensite phase the austenite phase needs to transform into martensite phase. First the material is at point A where the initial ferrite phase is heated to a temperature above AC_1 or AC_3 (points C or C') where there is a phase transformation to the austenite/ferrite phase or austenite phase. Then there is second phase transformation due to the rapid cooling or quenching from the austenite/ferrite or austenite phase to the martensite phase to point D. The second phase transformation start at the M_S temperature (between points C and D in figure 2.2).

The martensite start temperature (M_S) is related to the alloying elements of the austenite phase and the size of the austenite grain when the martensite phase starts to nucleate. Alloying elements in the austenite phase will influence the phase transformation from the austenite phase to the martensite phase. The M_S can be related to the alloy composition which can alter the M_S temperature. An example of a M_S is equation 2.1 in table 2.1 or with equation 2.2 in table 2.1.

Table 2.1: Martensite start temperature calculations

Eq.	Martensite start temperature	Ref.
2.1	$M_S(°C) = 539 - 423C - 30.4Mn - 17.7Ni - 12.1Cr - 11.0Si - 7.0Mo\ (mass\%)$	[2]
2.2	$M_s(℃) = 565 - 31Mn + 13Si + 10Cr + 18Ni + 12Mo - 600\left[1 - e^{(0{,}96C)}\right]\ (mass\%)$	[3]
2.3	$M_S = M_{S0} - K_1 x_c - K_2 V_\gamma^{-1/3}$ a	[4]
2.4	$M_S^0 - T = \frac{1}{b}\ln[\frac{1}{aV_\gamma}\{exp\langle -\frac{\ln(1-f)}{m}\rangle - 1\} + 1]$ b	[5]
2.5	$M_S(°C) = 475.9 - 335.1C - 34.5Mn - 1.3Si - 15.5Ni - 13.1Cr - 10.7Cr - 10.7Mo - 9.6Cu + 11.67\ln(d_\gamma)\ (mass\%)(\mu m)$ c	[6]

a Where M_{S0} is a martensite start temperature that depends on the alloying elements or the internal stress or strain at the interphase interface between the two phases, A is a temperature per carbon concentration, B is a prefactor grain volume term, V_γ is the average austenite grain volume and x_c is carbon concentration in mass percentage.
b Where K_1 and K_2 are empirical fitting constants, f is the first detectible martensite phase fraction, m is the aspect ratio of the martensite plate, M_S^0 is the martensite start temperature for a infinitely larges austenite grain size, V_γ is the average austenite grain volume and T is the amount of undercooling below M_S^0.
c Where $d_\gamma$is the average austenite grain size diameter.

The M_S can is also dependent on the austenite grains size. Martensite phase forms as plates or lenses within the austenite grains. The number of detectible martensite plates per unit volume in austenite is related to the grain size of the austenite. So that the fraction of martensite in austenite phase needs to increases as the austenite grain volume size decreases. For smaller and therefore larger amounts of austenite grains per unit volume there are more nucleation sites for the martensite phase. So that the austenite grain sizes therefore influence the M_S.

In a study by E. Jimenez-Melero et al. (2007) [4] there is concluded that there is a relation between the M_S and the austenite grain size (AGS). In this study a TRansformation Induced Plasticity (TRIP) steel is used for the determination of the M_S with equation 2.3 in table 2.1. H-S.Yang and H.K.D.H. Bhadeshia (2009)[5] have also obtained equation 2.4 in table 2.1 to determine the effect of austenite grain sizes on the M_S. Alloy elements are not used as input parameter but only the volume, fraction or ratio of the phases. If $M_S^0 - T$ where T is the temperature at which martensite start to form within a austenite grain (which can be lower than the first detectible martensite), becomes $M_S^0 - M_S$ is the first detectible martensite in the austenite then the martensite grain volume fraction is set to a value of the first detectible martensite. When $V_\gamma \to \infty$ then the average austenite grain is infinite than M_S^0 in equal to M_S to that $M_S^0 - T$ becomes $M_S - T$.

In a recent study by S.-J. Lee and K.-S. Park (2013) [6] the influence of the alloying elements coupled with the average austenite grain size (AGS) let to a new M_S temperature equation 2.5 in table 2.1.

Then D.P. Koistinen and R.E. Marburger(1959) [7] has published a paper with equation 2.6 to calculate the amount of austenite which is independent of austenite grain size and is therefore depends on the volume fraction or ratio of the austenite phase.

$$1 - V_\gamma = exp(\beta(M_S^0 - T) \quad (2.6)$$

Where $\beta \approx -0.011\ K^{-1}$, M_S^0 is the fundamental martensite-start temperature and V_γ is the average austenite volume fraction.

2.4.The partitioning step

In the partitioning step there is carbon(C) diffusion from the martensite phase to the austenite phase (points F to G in figure 2.2). So that the austenite becomes enriched with Carbon (C) and in this way it remains metastable at RT forming what is called “retained austenite”. The carbon concentration in the retained austenite is a time depended factor and it is related to diffusion. The stability (explained in chapter 2.5) of the retained austenite depended on the carbon concentration of each grain. To have stable retained austenite grains at room temperature the amount of carbon concentration in each grain must be higher than equation 2.1. In equation 2.1 the alloying elements play an important factor to determine the M_S temperature or the carbon concentration at which the retained austenite is stable at room temperature.

The interphase interface between the martensite phase and the austenite phase has an important influence for the diffusion of carbon atoms. There are different models proposed for the diffusion of carbon atoms from the martensite phase to the austenite phase.

J. Speer et al. (2003) [8] introduced the carbon constrained equilibrium (CCE) model where there are only interstitial diffusion of carbon atoms through the interphase interface due to the low partitioning temperature(PT). The interphase interface is stationary so that the chemical potential of carbon (C) atoms in the martensite phase and the austenite phase are the same.

N. Zhong et al. (2006) [9] have shown that the interphase interface is not stationary and there is a migration of the interphase interface. In the model of M. Santofimia et al. (2009) [10] their have simulated three cases of different interphase interface characteristics. The difference between the three cases are the activation energy for interphase interface mobility. The interphase interface migrations of the medium and low activation energy at long partitioning times (Pt) is from martensite phase into the austenite phase. At the low activation energy there is initially a high carbon content at the interphase interface so that

the interface moves from the austenite phase to the martensite phase and after 0,1 and 1 second the interphase interface reverses into the austenite phase.

Alloying elements such as manganese (Mn), nickel (Ni) and chromium (Cr) elements will retard or inhibit the formation of unwanted phases such as ferrite, perlite and bainite during the partitioning step. Carbide precipitates are unwanted phases as their will act as “sinkholes” for carbon atoms diffusing from the martensite phase to the austenite phase. This lowers the carbon concentration of retained austenite and therefore reducing the stable retained austenite phase at room temperature (RT). To inhibit the formation of carbide precipitates the alloying element of silicon (Si) is added.

2.4.1. Partitioning time

Partitioning time (Pt) is the time that carbon atoms can diffuse from the martensite phase into the austenite phase. Carbon atoms first encounters the interphase interface of the martensite /austenite phase and then they diffuse by interstitional diffusion in the austenite grain. If the partitioning time is long enough then there will be a homogenous distribution of carbon atoms through the austenite grain. There is a difference in carbon concentration between different austenite grains as concluded by M. De Meyer et al. (1999) [11] and simulated by Y. Takahama et al. (2012) [12].

2.5. Mechanical stability of retained austenite phase

The mechanical stability of retained austenite phase is the stability against the formation of martensite phase under the influence of deformation. Critically, if the retained austenite to martensite phase transformation occurs at small strains it is unable to retard the necking of the material. If it is to stable (not phase transformations at large strains) then it will not contribute to the TRIP-effect (J. Hyun Ryu et al. (2010)) [13, 14].

The mechanical stability of retained austenite phase is investigated in literature. For TRIP [14-23], for Q&P [17, 24-26] and for other material [27] . For TRIP steels we distinguish that the phases surrounding the retained austenite are bainite, ferrite and the martensite phase. The retained austenite can be divided in too two different microstructures. These microstructures are film-like and blocky type retained austenite (figure 2.3) [28].

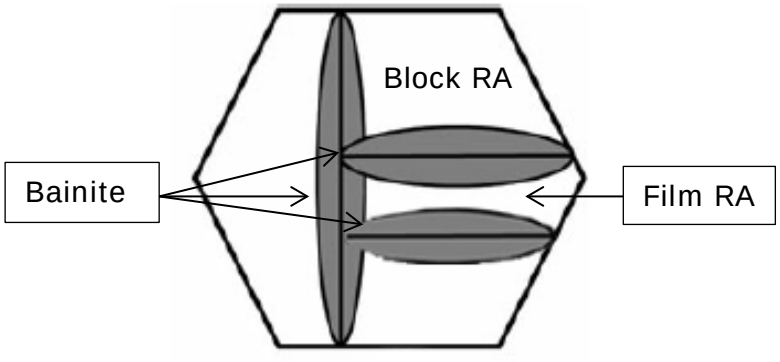

Figure 2.3: Austenite grain with film-like and blocky retained austenite [29] (and adapted)

If the retained austenite is situated in between martensite laths then it's Film-like retained austenite (X.C. Xiong et al. (2012)[26]) or surrounded by bainitic ferrite and then is called interlath film-like austenite (S. van der Zwaag et al. (2002) [22]).

The blocky type retained austenite is the retained austenite between the bainite-ferrite boundary and it's called intergranular austenite (A. Dimatteo et al. (2006)[30]) and/or inside the ferritic grains and it's called inter-ferritic austenite (X.C. Xiong et al. (2012) [26]).

If the surrounding laths of film-like in a TRIP steel is of bainitic ferrite (interlath film-like austenite) or martensite laths (E. De Moor et al. (2008)[17], A. Talapatra (2013) [31]) the film-like retained austenite is more mechanical stable than blocky type retained austenite due to the fact that it is carbon enriched from both sides (X.C. Xiong et al. (2012) [26]). This enrichment of carbon will increase the mechanical stability of retained austenite [26]. For TRIP steels the retained austenite grain orientation with respect to the applied stress has an influence on the mechanical stability of retained austenite (S. van der Zwaag et al. (2002)[22], S.O. Kruijver et al. (2003a) [23], S.O. Kruijver et al. (2003b)[21], I.B. Timokhina et al. (2003) [16]). The retained austenite phase is one of the hardest phases present in the TRIP steels (Q. Furnémont et al. (2002) [32]) so that the retained austenite phase experience less of the deformation then the average elongation in the tensile specimen (J. Hyun Ryu et al. (2010) [13]). Alloying elements in the steel such as C and Mn will be retained austenite stabilizers which increases the mechanical stability of retained austenite in TRIP steels (S. Lee et al. (2011) [33]).

In Q&P steel there is inhomogeneous distribution of carbon concentration throughout the retained austenite grains and this will increase the mechanical stability of the retained austenite (A. Takahama et al. (2012) [12]). For Q&P steels we distinguish that the phases surrounding the retained austenite are (potential) ferrite and martenisite. The retained austenite can be divided into two morphologies. These morphologies are film-like and blocky type retained

austenite (C.Y. Wang et al. (2010) [17, 34, 35]. In Q&P steels the film-like retained austenite is more stable than the blocky type retained austenite (X.C. Xiong et al. (2012)[26]). In Q&P steels the mechanical stability of retained austenite produces a TRIP-effect (M. De Moor et al. (2008) [17], M. Santofimia et al. (2011)[36], C.Y. Wang et al. (2012) [37]).

2.5.1. The TRIP-effect

The TRIP-effect is based on the idea that when a mechanical deformation is applied on a austenite phase it will undergo a phase transformation to the martensite phase and there is a strain hardening effect which retard necking of the material. Deformation induced retained austenite to martensite phase transformation is a temperature dependent phase transformation. It can be distinguished between stress-assisted nucleation or strain-induced nucleation of the martensite phase.

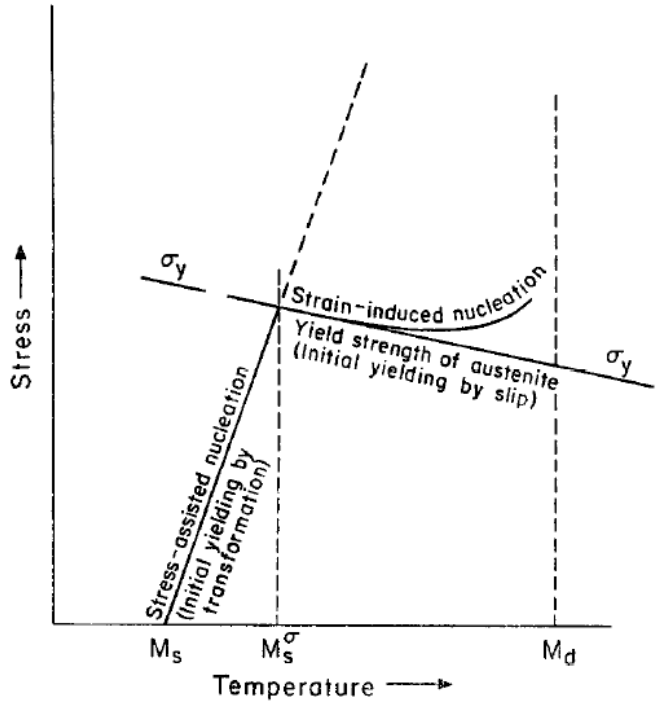

Figure 2.4: Stress-assisted (obtained from [38])

Figure 2.4 displays a stress vs. temperature diagram for the nucleation of martensite phase from the austenite phase. There are three main temperatures indicated and these are: M_s, M_s^σ and M_d. If the material temperature is at or below M_s then there is an unstable austenite phase and the will be a nucleation to the martensite phase a this nucleation process is a athermal nucleation process where no thermal activation is needed to have nucleation of the martensite phase it is only depended on a sufficient cooling to M_s temperature or below.

In the temperature range between M_s and M_s^σ there is a metastable (retained) austenite phase where only nucleation to the martensite phase can be achieved when stress is applied. The nucleation of martensite phase is a athermal process whereby the nucleation is performed at a constant temperature (D.E. Laughlin et al. (2009) [39]). If nucleation of the martensite phase is between M_s and M_s^σ temperate range then the stress levels applied to the austenite phase are at or below the yield stress. This martensite phase nucleation is called stress-assisted nucleation.

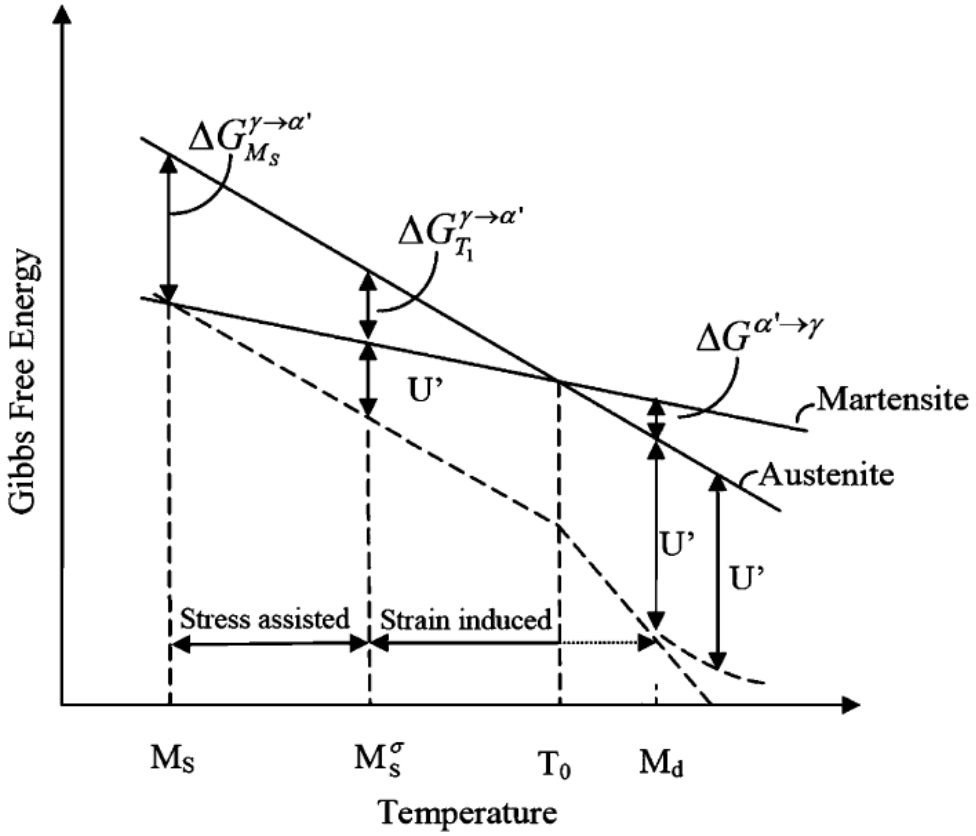

Figure 2.5: Gibbs Free energy vs. Temperature (obtained from [40])

To calculated the stress that is needed to have stress-assisted nucleation the free energy of the nucleation of the martensite phase from the austenite phase ($\Delta G^{\gamma\to\alpha\prime}$) is explained equation 2.7.

$$\Delta G_{M_s}^{\gamma\to\alpha\prime} = \Delta G_{T_\#}^{\gamma\to\alpha\prime} + U' \tag{2.7}$$

Where $\Delta G_{T_\#}^{\gamma\to\alpha\prime}$ is the free energy (at a temperature between M_s and M_s^σ) for the nucleation of the martensite phase from the austenite phase and U' is the mechanical energy, Given by:

$$U'_{stress-assisted} = \tau_s\gamma_0 + \sigma_n\varepsilon_n \tag{2.8}$$

Where τ_s is the resolved shear stress along the invariant plane of the interface between (parent) (retained) austenite and martensite phase, γ_0 is the magnitude of the shear, σ_n is the resolved shear stress normal to the invariant plane and ε_n is the normal dilation.

The martensite phase nucleation in stress-assisted nucleation takes place at the same sites or embryo locations as “normal” (M_s) martensite phase nucleation (G.B. Olson and M. Cohen (1972) [38]).

In the temperature range between M_s^σ and M_d, there is a metastable (retained) austenite phase whereas stress is needed to be applied in order to have the martensite phase nucleation above the yield stress of the austenite phase and therefore it is called the strain-induced nucleation.

To calculated the stress that is needed to have strain-induced nucleation equation 2.7 is used where $\Delta G_{M_s}^{\gamma\rightarrow\alpha'}$ is the free energy at a temperature between M_s^σ and M_d to have nucleation of the martensite phase from the austenite phase and U' is the mechanical energy but now given by equation 2.9. (S. Chatterjee and H.K.D.H. Bhadeshia (2007)[41]).

$$U'_{strain-induced} = \frac{1}{8\pi(1-\nu)} G b^{1/2} \left(\frac{\varepsilon_c}{L}\right)^{1/2} + \tau_s \qquad (2.9)$$

Where b is the Burgers vector, G is the shear modulus, L is the parameter related to the austenite grain, ν is Poisson’s ratio, τ_s is the resolved shear stress along the invariant plane and ε_c is the critical strain.

At temperature T_0 (figure 2.5) the Gibbs free energy of the austenite phase is in equilibrium with the martensite phase, so that at a temperature between T_0 and M_d the $\Delta G_T^{\gamma\rightarrow\alpha'}$ is negative and becomes $\Delta G_T^{\alpha'\rightarrow\gamma}$ therefore the mechanical energy (U') needs to be increased in order to compensate for the negative $\Delta G_T^{\gamma\rightarrow\alpha'}$ and to have a phase transformation from austenite to the martensite phase.

The strain-induced martensite nucleation’s occurs at new sites or embryo locations (G.B. Olson and M. Cohen (1972) [38]).

If the temperature is at M_d or above there is a stable retained austenite phase where nucleation of martensite phase cannot be accomplished with applied a stress of any magnitude and ε_c in equation 2.9 acts as a critical value.

In the partitioning step the austenite phase is enriched with carbon and this has an effect on the mechanical stability of the austenite phase at room temperature (RT). The carbon concentration will shift the M_s temperature below the RT to a temperature between M_s and M_d of Figure 2.4 and Figure 2.5. Between this temperature range of the M_s and M_d, the (retained) austenite phase with a high

carbon concentration becomes a metastable (retained) austenite phase and within a temperature range between M_s and M_s^σ and the stress needed to have a phase transformation is below the yield stress of the austenite phase. If the carbon concentration is further increased so that RT is between M_s^σ and M_d range then the stress needed to transform the retained austenite phase into martenite phase is above the yield stress of the (retained) austenite phase. If the carbon concentration is at a level that RT is above M_d so that there is no phase transformation due to stress possible.

Q. Furnémont et al. (2002) [32] has stated that the increase of the yield stress of retained austenite is related to the increase of the carbon content in the austenite phase. The yield stress of the austenite phase determines the transition point between stress-assisted and strain-induced martensite nucleation. In study by S. Chatterjee and H.K.D.H. Bhadeshia (2007) [41] have concluded that the TRIP-effect started when there is stress-assisted plasticity and Q. Furnémont et al. (2002) [32], S.O. Kruijver (2003a) [23], M-Y. Zhang et.al. (2011) [42] when there is strain-induced plasticity.

2.5.2. Inhomogeneous distribution of carbon in austenite phase

The carbon concentration in the retained austenite phase is inhomogeneous distributed so that individual austenite grains have different carbon concentrations. The inhomogeneous distribution of carbon concentration is beneficial for the TRIP-effect. If the retained austenite grains have different carbon concentrations the phase transformation from retained austenite phase to martensite phase start at different strains when force is applied to the steel and it will start at stress-assisted or and strain-induced nucleation. This retard and distribute the nucleation of the martensite phase in the material.

2.6. In situ X-ray diffraction for TRIP-steels and Q&P-steels

The In situ X-ray diffraction is mainly used for material that has a phase transformation when a mechanical deformation is applied to obtain the mechanical- and microstructural properties of the material. We can distinguish two different types of In situ X-ray diffraction. These types are conventional- and synchrotron In situ X-ray diffraction. Using a conventional X-ray diffraction and synchrotron the difference between the two types is the wavelengths used to obtain the diffraction peaks.

Conventional: For conventional In situ X-ray diffraction a wavelength of 10^{-1} nanometre is used with a X-radiation energies up to 10 KeV. The penetration depth as which the crystal structure of the material can be calculated with Beer-Lambert equation 2.20

$$\frac{I}{I_0} = e^{(-\frac{\mu}{\rho}\rho x)} \tag{2.20}$$

Where I is the intensity, I_0 is the initial intensity, $-\frac{\mu}{\rho}$ is the mass absorption coefficient, ρ is the density and x is the penetration depth. In order to calculate

the penetration depth the intensity of x-rays traveling through the metal will decrease to $\frac{1}{e} \approx 0{,}37$ [43] from the surface value so that $(\frac{\mu}{\rho})\rho x = 1$. The penetration depth in iron (Fe) when cobalt (Co) is used as a X-ray source to create a wavelength then the maximum penetration depth is 23 µm.

Synchrotron: For synchrotron In situ X-ray diffraction 10^{-2} nanometre wavelengths are needed which can only be generated with high X-radiation energies of 400 KeV. Synchrotron In situ X-ray diffraction is used to obtain three-dimensional imagine information of an individual grain of the microstructure. Whereas conventional In situ X-ray diffraction cannot be related to individual grain but to multiple grains of the microstructure. In synchrotron there is transmission of the X-ray beam through the tensile specimen so that no penetration depth.

The purpose of these experiments focus on the mechanical stability of the material when it's mechanically deformed which can be related to the retained austenite, the carbon concentration in the retained austenite, the influence of other alloying elements then carbon and the martensitic nucleation rate.

In work by L. Zhao et al. [44] on TRIP steel with conventional In situ X-ray diffraction at the main focus of this research is the dislocation density of the material and the inhomogeneous carbon concentration of different austenite grains controlling the phase transformation from retained austenite phase to the martensite phase. The outcome is that the carbon concentration in the retained austenite is major controlling parameter for the phase transformation (the TRIP-effect).

S. Van der Zwaag et al. [22] researched on TRIP steel with conventional- and synchrotron In situ X-ray diffraction the influence of carbon concentration in retained austenite grains and the (mechanical) stability in different orientations. The conclusion is that the carbon concentration in the retained austenite grains has a influence on the mechanical stability and so on phase transformation when mechanical deformation is applied. The k_p value of the Ludwigson and Berger relation (equation 4.7) is strongly orientation-relation dependent.

S. Kruijver et al [23] used Synchrotron In situ X-ray diffraction on TRIP steel to investigate the mechanical stability with Ludwigson and Berger relation (equation 4.7) on different grain orientation relative to the tensile direction. The grains that are orientated with 0° and 90° in relation to the tensile direction have a preferential orientations for phase transformation and therefor the lowest stability is can probably related to the carbon concentration of the retained austenite grain.

In an article by A. Itami et al. [45] the plastic stability of TRIP steel is investigated with conventional (In situ) X-ray diffraction, whereby bainite is a controlling parameter which has an influence on the carbon concentration retained austenite when there is carbon diffusion from the martensite to the

austenite phase. The bainite phase is situated along the lath boundary with retained austenite in the microstructure. This will have an influence on the stability of the retained austenite which is calculated with Ludwigson and Berger relation (equation 4.7) and also a model of Takahashi et al. with the total driving force (equation 4.13) is used to predict at a certain applied strain the Ludwigson and Berger equation. They concluded that the stability of retained austenite increases when the carbon concentration in the retained austenite is increased. The phase transformation from retained austenite to martensite occurs on plastically unstable retained austenite with a low carbon concentration.

P.J. Gibbs et al. [15] used a TRIP steel with high (7,09 mass%) manganese (Mn) alloying element to investigate the retained austenite stability with conventional (In situ) X-ray diffraction . In this Mn-TRIP steel where intercritical annealing is used, the Mn has the same function then carbon in retained austenite when it diffuses from the martensite phase to the austenite phase then there is a increase of retained austenite bcc crystal lattice distortion. This distortion will increase the total driving force needed to have a phase transformation from retained austenite to martensite phase when mechanical deformation is applied. To calculated the stability of the retained austenite the Ludwigson and Berger relation (equation 4.7) is used. The conclusion is that increasing the annealing temperature decreases the retained austenite stability and increased the strain hardening due to the TRIP-effect.

E. De Moor et al. [17] described on a Q&P steel with conventional (In situ) X-ray diffraction the dependence of the mechanical properties on the heat treatment of the material. To calculated the stability of the retained austenite the instantaneous strain hardening (equation 4.1) and the Ludwigson and Berger relation (equation 4.7) were used. It is concluded that the tensile strength/total elongation is depended on the partitioning conditions and that the strain hardening has a significant dependence on the partitioning temperature and partitioning time. The TRIP-effect occurs in Q&P steel and has its contribution to the strain hardening.

3. Experimental

3.1. Introduction

In this chapter the experimental set-up is described in particular the type of research, the specimen preparations and the In situ X-ray diffraction measurements.

3.2. Type of research

The type of research used in this thesis is a quantitative research whereby the outcome of this research can be used to explain mechanical properties of the quenching and partitioning (Q&P) steels. There is limited numbers of samples used for this experiment, so that the accuracy can be increased when the number of equivalent experiments is also increased.

3.3. Q&P Materials

There are three different Q&P materials studied and these materials are obtained from two different material suppliers namely OnderzoeksCentrum voor Aanwending van Staal (OCAS) NV and Thyssenkrupp Steel Europe AG (TKS). The difference between the obtained materials are chemical compositions and the heat treatment properties which related to the austenite to martensite phase transformation and the carbon diffusion. The different chemical and heat treatment properties of the OCAS NV materials can be seen in table 3.1. The obtained material from Thyssenkrupp Steel Europe AG has two different heat treatment properties: The C28-QT240 material has undergone a ‘standard’ Q&P two-step heat treatment process with the exception of that the partitioning stage is not isothermal and the C28-QT280 material has undergone a one-step Q&P heat treatment process. The different chemical and Q&P heat treatment properties of the TKS can be seen in table 3.1 A schematic heat treatment representation for a normal heat treatment as for C25 & C30 material is given by figure 3.1. For the non-isothermal heat treatment for C28-QT240 material can be seen in figure 3.2 and the one step heat treatment for the C28-QT280 material can be seen in figure 3.3.

Table 3.1: Chemical and heat treatment properties of the OCAS and TKS Q&P steels

Provider	Sample	C, mass%	Si, mass%	Mn, mass%	M_s,°C	QT,°C	PT, °C	Pt,s
OCAS	C25-QT244-50	0,25	1,5	3	326	244	400	500
	C25-QT224-50					224		
	C25-QT244-25					244		250
OCAS	C30-QT237-50	0,3			303	237		500
	C30-QT217-50					217		
TKS	C28-QT240	0,278	1,92	2,53	321	240	450	44
	C28-QT280					280	0	0

*The main chemical compositions (C, Si and Mn), (M_s) martensite start temperature, (QT) quenching temperatures, (PT) partitioning temperature and (Pt) partitioning times

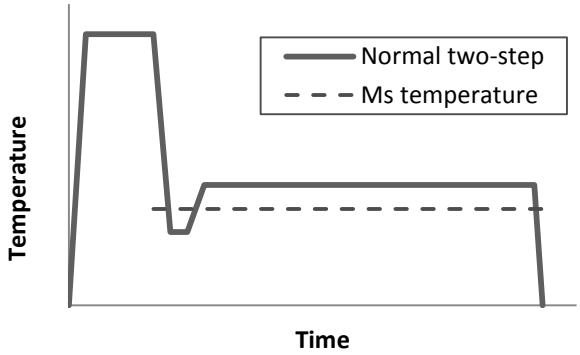

Figure 3.1: Normal two-step Q&P heat treatment

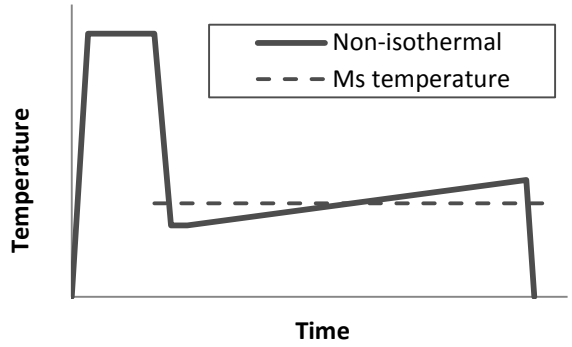

Figure 3.2: Non-isothermal Q&P heat treatment

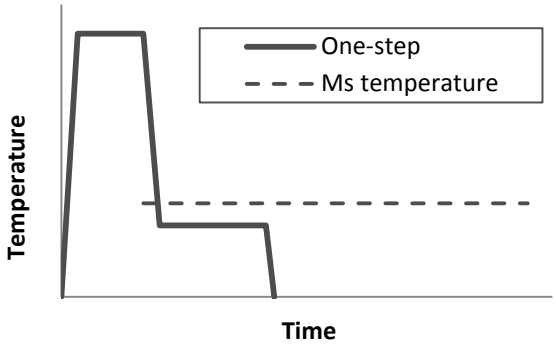

Figure 3.3: One-step Q&P heat treatment

In order to optimise the In situ X-ray diffraction experiments with limited amount of supplied experiment material a test matrix is used (table 3.2). A standalone test is performed to verify the mechanical properties of the designed tensile specimen geometry for the use in the Deben Microtest machine in combination with X-ray diffraction.

Table 3.2: Test matrix of supplied Q&P steels

Sample material	Number of tensile test specimens	
	Standalone tensile test	In situ X-ray diffraction
C25-QT244-50		1
C25-QT224-50	1	1
C25-QT244-25		1
C30-QT237-50		1
C30-QT217-50		1
C28-QT280		1
C28-QT240		1

3.4. Preparation of specimen geometry

The Deben Microtest machine is used in this work (see figure 3.4) and is capable to obtain a maximum tensile specimen size with length and width of 54,5 and 40 mm.

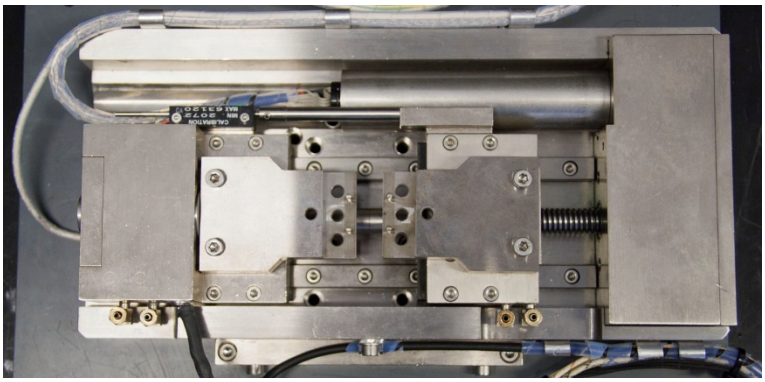

Figure 3.4: Deben Microtest machine

The supplied Q&P material which is used for the experiments can be described as strip material. The strips need to be fabricated into dog bone tensile specimens (see figure 3.5). Wire electro-discharge machining (WEDM) is used to produce the dog bone geometry. Also a production drawing is created see Appendix A. The Deben Microtest machine tensile specimens (figure 3.5) have an different dimension compared to a standard tensile specimen *ISO 6892-1:2009,IDT standard* see figure 3.6. Where a_o is the original thickness of the tensile specimen, b_o is the original width of the tensile specimen, L_c is the parallel length, L_o is the original gauge length, L_t is the total length of tensile specimen and S_o is the original cross-section area of the parallel length.

To optimizes the cross-section area of the parallel length (14,5, figure 3.5 with reference S_o, figure 3.6) (width and thickness) of the tensile specimen taking account with the combination (In situ) of tensile test and X-ray diffraction, where the surface area (14,5 × 3,3 mm, figure 3.5 with reference L_o x B_0, figure 3.6) of the tensile specimen is used for the X-ray diffraction and the thickness (0,8 mm, figure 3.4 with reference a_0, Figure 3.6) for the tensile specimen.

For the C28-QT280 tensile specimen thickness is reduced from the standard 0,8 mm (see figure 3.5) down to 0,65 mm to compensate for the higher mechanical properties of the material.

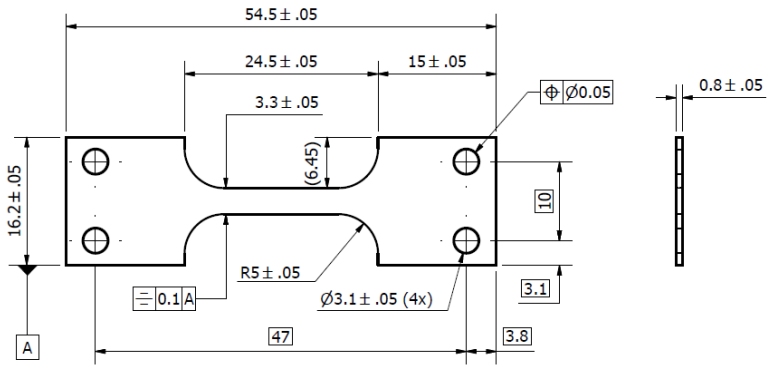

Figure 3.5: Tensile specimen (dimensions are in mm)

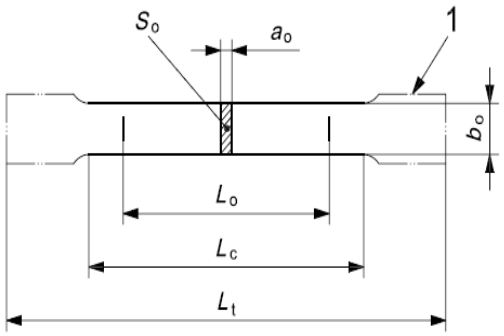

Figure 3.6: Standard ISO 6892-1 tensile specimen obtained from ISO 6892-1:2009, IDT standard

3.5. Tensile measurement

A uniaxial tensile measurement with Deben Microtest machine was performed to verify if the mechanical properties of the tensile specimens fabricated for the Deben Microtest machine in comparison with the already known mechanical properties of the material obtained from the material supplier. The Deben Microtest machine is controlled with an PC using control software version 5.4.6 and can apply a maximum force to the tensile specimen of 5 kN. The dimensions of the cross-section area of the tensile specimen are designed to create fracture below a force of 5 kN and for the tensile surface optimisation for X-ray diffraction. Any deviation in the mechanical properties can be explained as geometrically alteration due to stress concentrations as the cross-section area (3,3 × 0,8 mm, figure 3.5 with reference S_o, figure 3.6) of the parallel length is reduced. To conduct the tensile test, test parameters of the ISO 6892-1:2009 standard with an strain control rate of 6×10^{-4} s^{-1} at room temperature (RT) are used.

3.6. Preparation of specimen surface

When the tensile specimens are machined the will have the Deben Microtest tensile specimen geometry and the surface roughness of R_a = ±0,8 µm. To avoid scattering (noise) of the X-ray signals, a smooth surface is required. In order to create a smooth surface (R_a = ±0,4 µm), multiple polishing steps are to be performed to refine the surface so that the diffraction of X-ray waves are at its optimum. There multiple types of polishing treatments to create the smooth surface needed for X-ray diffraction.

Method 1: Is the mechanical (frictional) polishing where the tensile specimens are mechanical polished using a Struers LaboPol-21 machine for grinding with grit sizes: FEPA P800, P1200 and P2000 and a Struers LaboPol-5 machine for polishing with MD-Mol cloth with diamond abrasive of 3 µm grain size and MD-Nap cloth with diamond abrasive of 1 µm grain size.

Method 2: Is with electro-chemical polishing where the tensile specimens are first mechanical polished and then placed in an electro-chemical polishing machine where the tensile specimen is the anode and the electro-chemical polishing machine is the cathode. The rough surface has a larger surface area per unit volume than a smooth surface, so that the rough surface will oxidize easier than a smooth surface therefore decreasing the roughness of the surface.

With mechanical (frictional) polishing, heat is introduced on the surface of the tensile specimen so that the volume fraction of retained austenite (equation 4.4) at the surface layer can be different then the bulk of the tensile specimen [46]. In order to exclude that there is a phase transformation of the retained austenite to the martensite phase at the surface layer, a second mechanical polishing is preformed after the first mechanical polishing step in one specific specimen to confirm if there is volume fraction retained austenite difference between each polishing step. The results can be seen in table 3.3.

Table 3.3: Two mechanical polishing steps on C25-QT244-50 sample

Mechanical polishing step	Tensile specimen thickness, mm	Retained austenite volume fraction (f^{γ})	Counting Statistical Error (CSE) for f^{γ} *
1	0,795	0,21	0,014
2	0,725	0,20	0,014

*The Counting Statistical Error (CSE) for X-ray diffraction (see Appendix B)

In table 3.3 there is a difference of 1,56% between the retained austenite volume fractions after the two polishing steps. The thickness reduction of the surface layer is 70 µm and this is almost three times the penetration depth for X-ray diffraction. There is no difference in retained austenite volume fraction between the two steps and the assumption is made that it's also valid for the other sample material due to the limited amount of material.

3.7. In situ X-ray diffraction measurements

In order to study the phase transformation of retained austenite into the martensite the phase transformation is measured with In situ X-ray diffraction see figure 3.8. For the In situ X-ray diffraction measurements a Deben Microtest machine is mounted on the Bruker D8 Discover X-ray diffraction machine to conduct simultaneously X-ray diffraction on specimen during tensile testing. The Bruker D8 Discover X-ray diffraction machine (see figure 3.7) produces a parallel beam radiation with Cobalt (Cokα) radiation at 45 KV and 25 mA, see figure 3.9. In the X-ray diffraction, the X-rays are diffracted and they have a maximum penetration depth of 22,5 µm with a wavelength (λ) of 1,79026 nm in Iron (Fe) with Cobalt radiation.

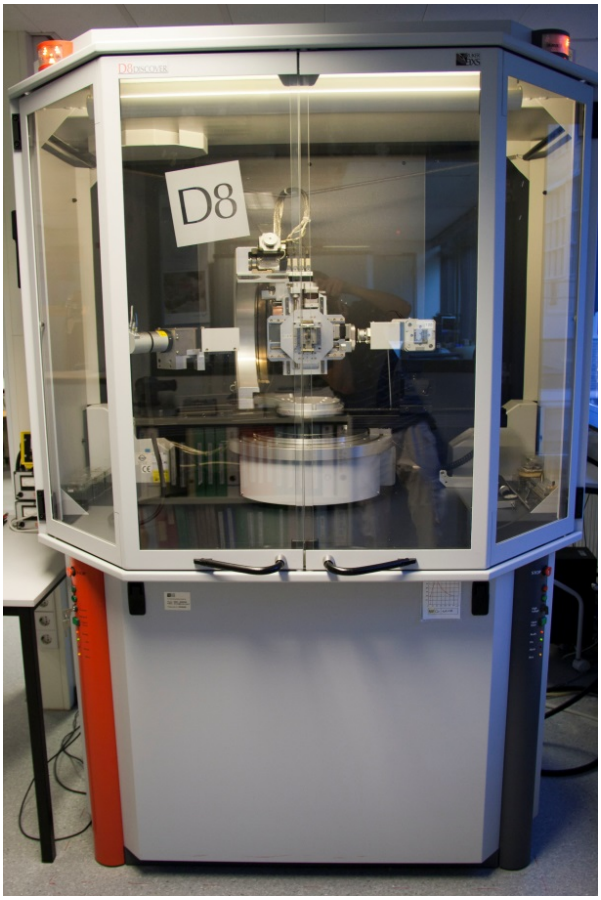

Figure 3.7: Bruker D8 Discover X-ray diffraction machine

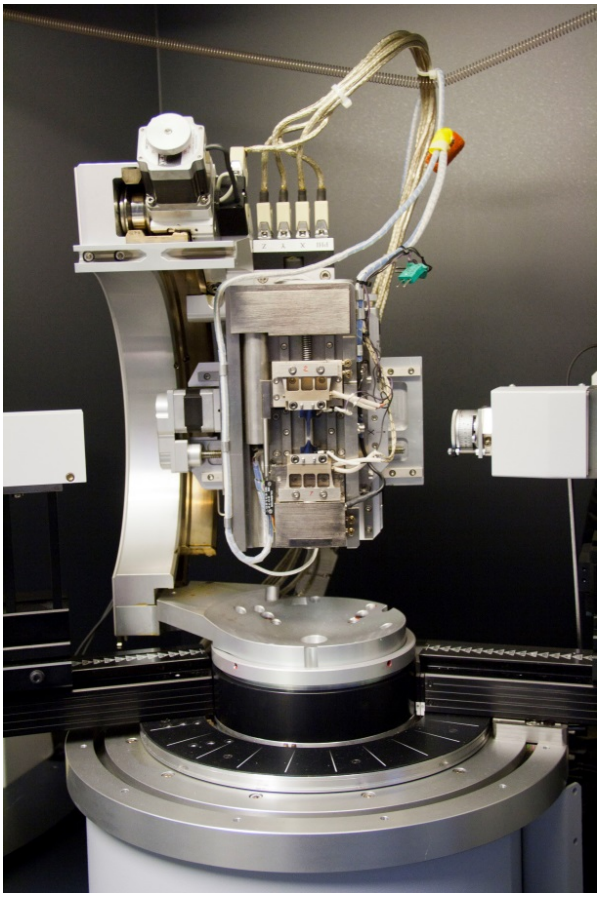

Figure 3.8: In situ X-ray diffraction experimental setup

The radiated surface area that is created with the X-ray diffraction machine has the dimensions of 3 mm of parallel beam height and 4 mm of parallel beam width. Which relates to the tensile specimen with 4 mm width and 3 mm of height of the tensile specimen. The radiated area is larger than the tensile specimen area of the tensile specimen so that the measure intensities needs to be corrected (equation 3.1). It is due to over radiating of tensile specimen with the X-ray beam. The tensile specimen area becomes larger with increasing of the Bragg angle (θ).

$$I_{corrected} = \frac{I_{measured}}{\sin\theta} \quad (3.1)$$

Where $I_{measured}$ is the measured intensity and θ is the Bragg angle. The corrected intensities are evaluated (smoothed) with Bruker DIFFRAC.EVA version 3.0 software.

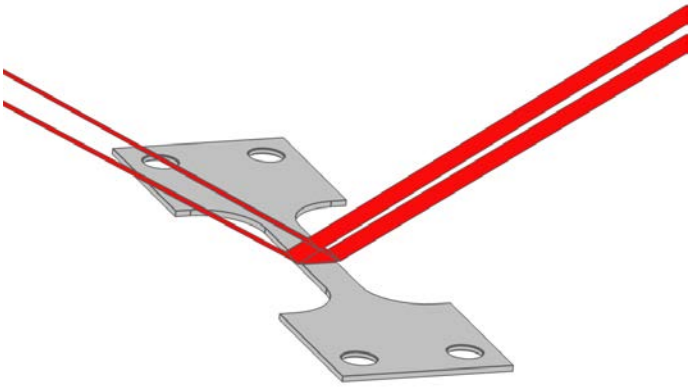

Figure 3.9: Parallel beam radiation

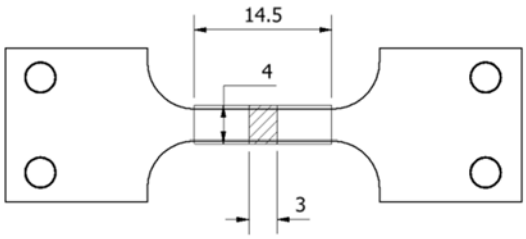

Figure 3.10: Radiated area of the tensile specimen

The radiated surface area (4×3 mm) is approximately 1/5 of the parallel specimen surface area (4×14,5 mm), see figure 3.10. This implies that when necking of tensile specimen starts it's possible that it's not in the radiated surface area.

The tensile specimens are mechanically deformed with a strain control rate of 6×10^{-4} s^{-1} in stress steps ($\Delta\sigma$) of 100 MPa. The optimum for requiring the TRIP-effect is performing the mechanical deformation with strain steps due to fact that plasticity is related to the strain and not the stress of the material. For the Deben Microtest machine the strain parameter is not a controlling parameter when the tensile experiment is executed. The controlling parameter of the Deben Microtest machine is the applied force on the tensile specimen. Therefore the inaccurate measurement of the strain with the Deben Microtest machine is the main reason to prefer for the stress step measurements. After each stress step a X-ray diffraction scan is obtained to measure the diffracted intensities at certain Bragg angles. In figure 3.11 the engineering stress vs. time is represented with the stress steps of 100 MPa are visible.

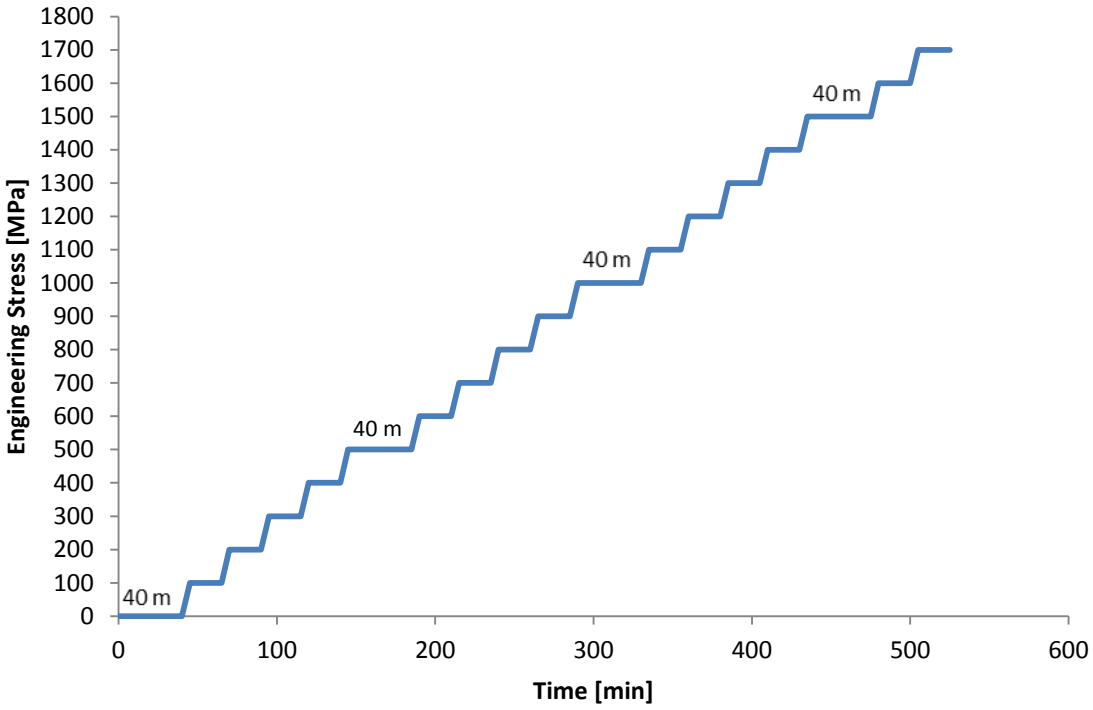

Figure 3.11: Stress steps vs. X-ray diffraction scan time

To restrict the duration of each stress step at which the material can alter its properties when the tensile specimen are scanned with different Bragg angle ranges. The first range was at the stress levels of 0, 500, 1000 and 1500 MPa and the X-ray diffraction scan consisted of the 2θ = 40° until 2θ = 135° Bragg angle range which consisted of the retained austenite $\{111\}_{\gamma}$, $\{200\}_{\gamma}$, $\{220\}_{\gamma}$ and $\{311\}_{\gamma}$ Bragg peaks and the martensite $\{110\}_{\alpha'}$, $\{200\}_{\alpha'}$,$\{211\}_{\alpha'}$ and $\{220\}_{\alpha'}$ Bragg peaks (figure 3.12). The counting time was 1 second per step, with a step size of 0,05° and the total 2θ scan time was approximately 40 minutes.

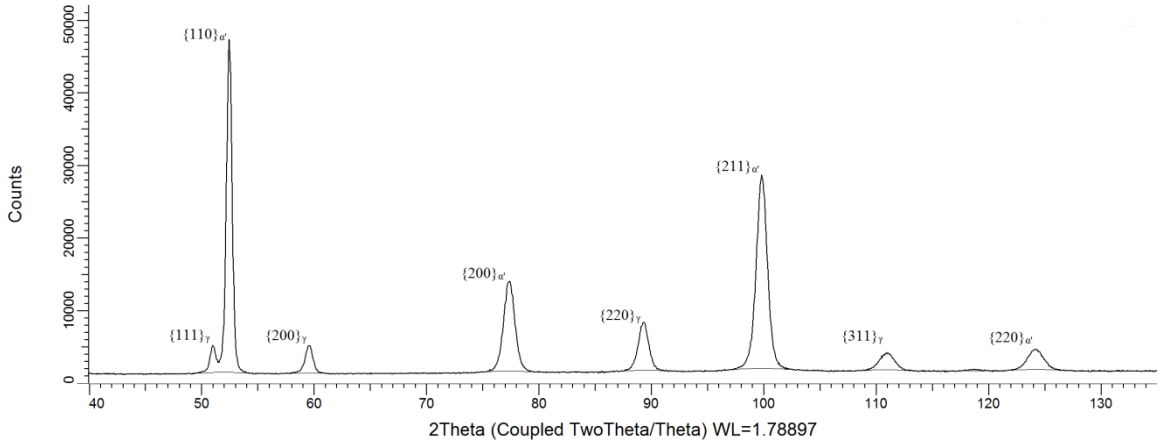

Figure 3.12: Example of X-ray diffraction scan of 2θ = 40° until 135° angle

The second range which was used at the intermediate stress levels the X-ray diffraction scan consisted of the 2θ = 55° until 2θ = 105° Bragg angle range which consisted of the retained austenite $\{200\}_{\gamma}$, $\{220\}_{\gamma}$ Bragg peaks and martensite $\{200\}_{\alpha'}$, $\{211\}_{\alpha'}$ Bragg peaks (figure 3.13). The counting time was in 1 second per step, with a step size of 0,05° and the total 2θ scan time was approximately 20 minutes.

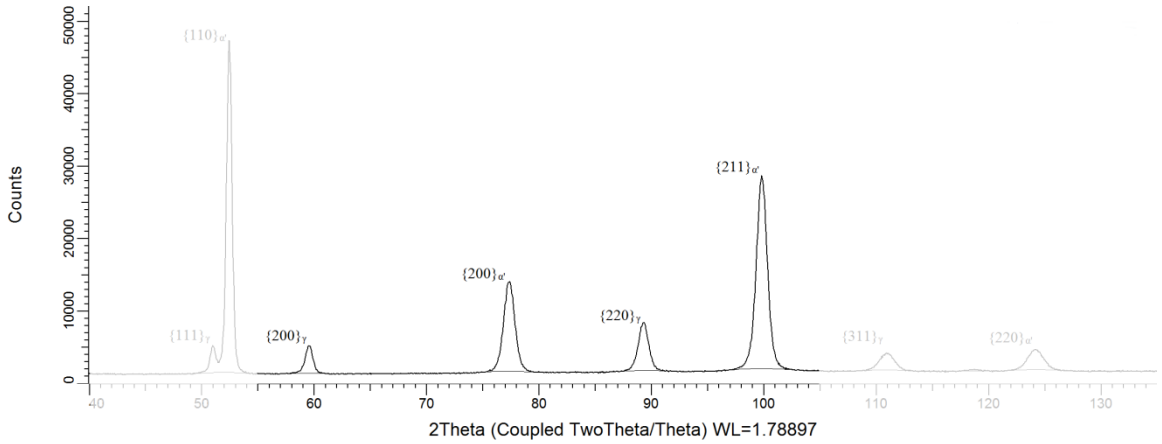

Figure 3.13: Example of X-ray diffraction scan of 2θ = 55° until 105° angle

To clarify the difference between the two ranges and the obtained hkl planes with the corresponding 2θ peaks can be seen in table 3.4.

Table 3.4: Investigated Bragg diffraction ranges

	Retained austenite(γ)				Martensite(α')			
hkl	$\{111\}_{\gamma}$	$\{200\}_{\gamma}$	$\{220\}_{\gamma}$	$\{311\}_{\gamma}$	$\{110\}_{\alpha'}$	$\{200\}_{\alpha'}$	$\{211\}_{\alpha'}$	$\{220\}_{\alpha'}$
2θ	±51,7°	±60,5°	±90,8°	±113,2°	±52,3°	±77,1°	±99,5°	±123,7°
Range 1	x	x	x	x	x	x	x	x
Range 2		x	x			x	x	

From the measured Bragg angles, lattice parameters of the different phase can be obtained. The lattice parameter of the different can be calculated with the following (equations 3.2, 3.3 and 3.4).

$$n\lambda = 2d_{hkl}\sin\theta \qquad (3.2)$$

Where n is the integer and depending on h parameter of the Miller indices (hkl) so that n is the n^{th} order of reflexion, λ is the wavelength, d_{hkl} is the spacing between atomic planes and θ is the Bragg angle between the incoming wave and the crystal lattice surface.

The lattice parameter is derived from the atomic spacing with the following equation.

$$d_{hkl} = \frac{a}{\sqrt{h^2+k^2+l^2}} \quad (3.3)$$

Where a is the lattice parameter and h, k, l are the Miller indices.

Equation 3.2 and 3.3 can be substituted leading in to the following equation to obtain the lattice parameter a.

$$a = \frac{n\lambda\sqrt{h^2+k^2+l^2}}{2\sin\theta} \quad (3.4)$$

4. Results and Discussion

4.1. Introduction

In this chapter the outcome of the experimental work is presented and discussed. The outcome of the mechanical testing in combination with (In situ) X-ray diffraction tests are: the mechanical properties of the material, the strain hardening and the retained austenite volume fraction at each stress step, the crystal lattice stress of the two phases with an orientation relation, the retained austenite stability under mechanical deformation and carbon concentration in the retained austenite phase. The obtained data with these experiments is limited so that this experimental work gives an indication of the TRIP-effect in Quenching and Partitioning (Q&P) steels. In table 4.1 the initial volume fraction of measured retained austenite volume fraction (f_0^γ) with In situ X-ray diffraction is shown.

Table 4.1: Initial volume fraction of retained austenite volume fraction

Specimen material	C25-QT244-50	C25-QT224-50	C25-QT244-25	C30-QT237-50	C30-QT217-50	C28-QT240	C28-QT280
f_0^γ	0,222± 0,006	0,190± 0,005	0,185± 0,005	0,179± 0,007	0,244± 0,005	0,237± 0,005	0,055± 0,006

4.2. Mechanical properties

The stress-strain curve of the different tensile specimens are obtained by the Deben Microtest machine and are shown in figure 4.1. The measured mechanical properties of the Q&P material can be seen in table 4.3 The obtained stress-strain curves deviates from the “normal steel” stress-strain curves expected for steel. The total elastic deformation (e_t) at the yield stress ($R_{p\,0,2}$) is approximately 0,05 and this value is ten times larger than expected (5×10^{-3}) for steel. In relation to the larger e_t, the total extension at maximum force (A_{gt}) also increased with 0,05. The yield stress and the ultimate tensile strength (UTS) or R_m are at expected values.

The measured mechanical properties can be compared to the obtained mechanical properties from the suppliers table 4.2. The Young's modulus of the measured stress-strain curve is a factor of ten times smaller the obtained Young's modules values from the suppliers, this is due to the Young's modulus relation with strain.

$$E = \frac{\sigma_e}{\varepsilon} \tag{4.1}$$

Where σ_e is the engineering stress and ε is the engineering strain. The measurement is conducted without measuring the strain with a extensometers but with the elongation of the tensile specimen 'grip' ends. To correct for the low Young's modulus values of the measured stress-strain curves a correction equation [47] is used which corrects for the stiffness of the Deben Microtest machine and the dimensions of the tensile specimen. The stiffness can be represented as a series of springs of the Deben Microtest machine (K_m), the tensile specimen filled zone part (K_f) and the tensile specimen parallel zone part (K_p). The stiffness can be converted into the elongations which are Δl_m , Δl_f and Δl_p. For more details of the conversion the author would like to refer to the article [47]. The ratio between filled zone elongation and the parallel zone elongation ($\Delta l_f / \Delta l_p = \alpha$) is 0,24. A remark for the corrected stress-strain curve is that only the Young's modulus is corrected and this corresponds only to the elastic part of the stress-strain curve. The plastic part of the stress-strain curve is not corrected with the correction equation. The corrected stress-strain curves can be seen in figure 4.2. The corrected stress-strain curves are shifted in negative strain value for the foot correction [48]. The foot correction corrects for the straightening of the tensile specimen in the tensile machine or the initial speed of testing. The corrected mechanical properties can be seen in table 4.4

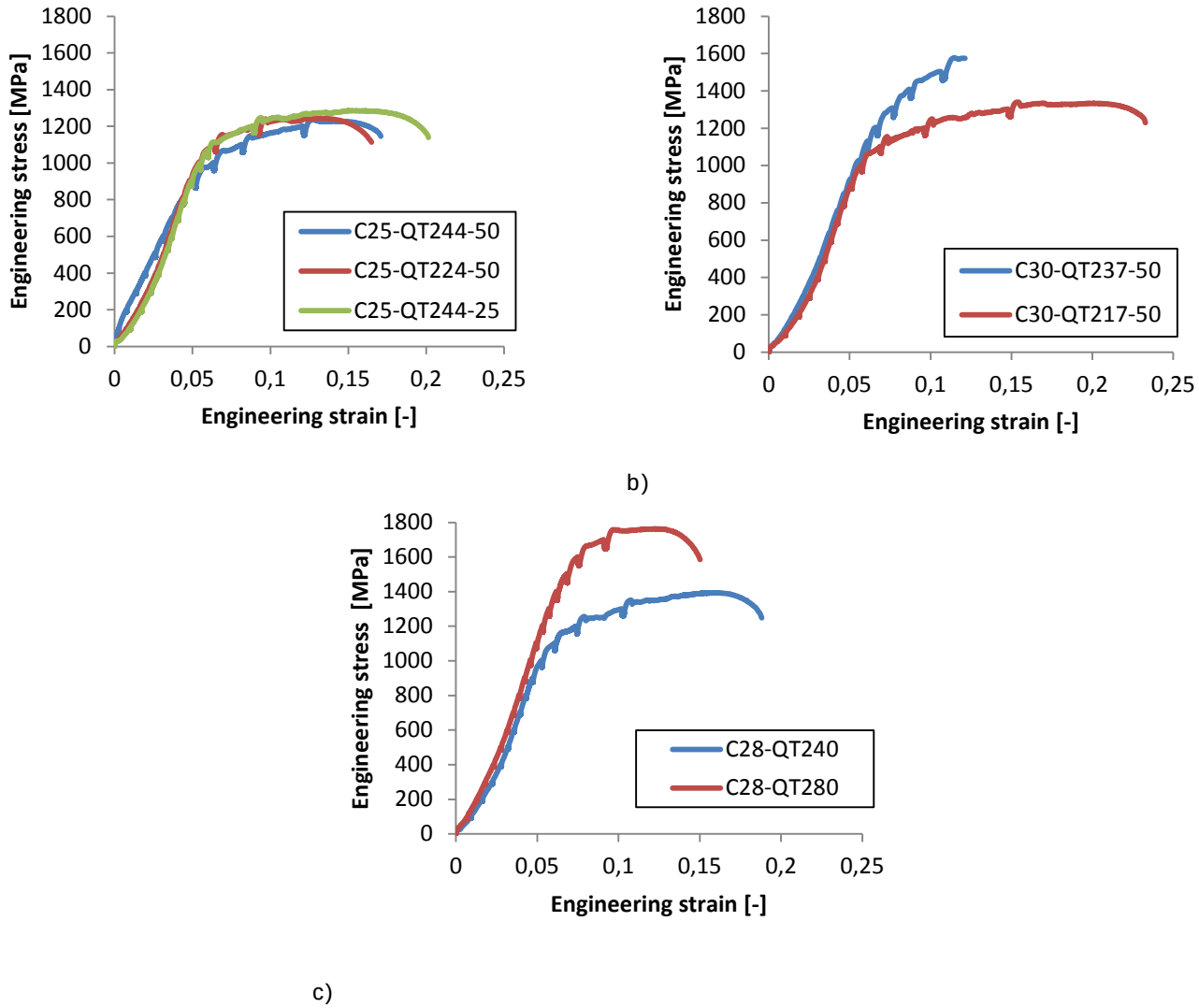

Figure 4.1: Measured Stress-strain plot for a) the C25 material, b) the C30 material and c) the C28 material

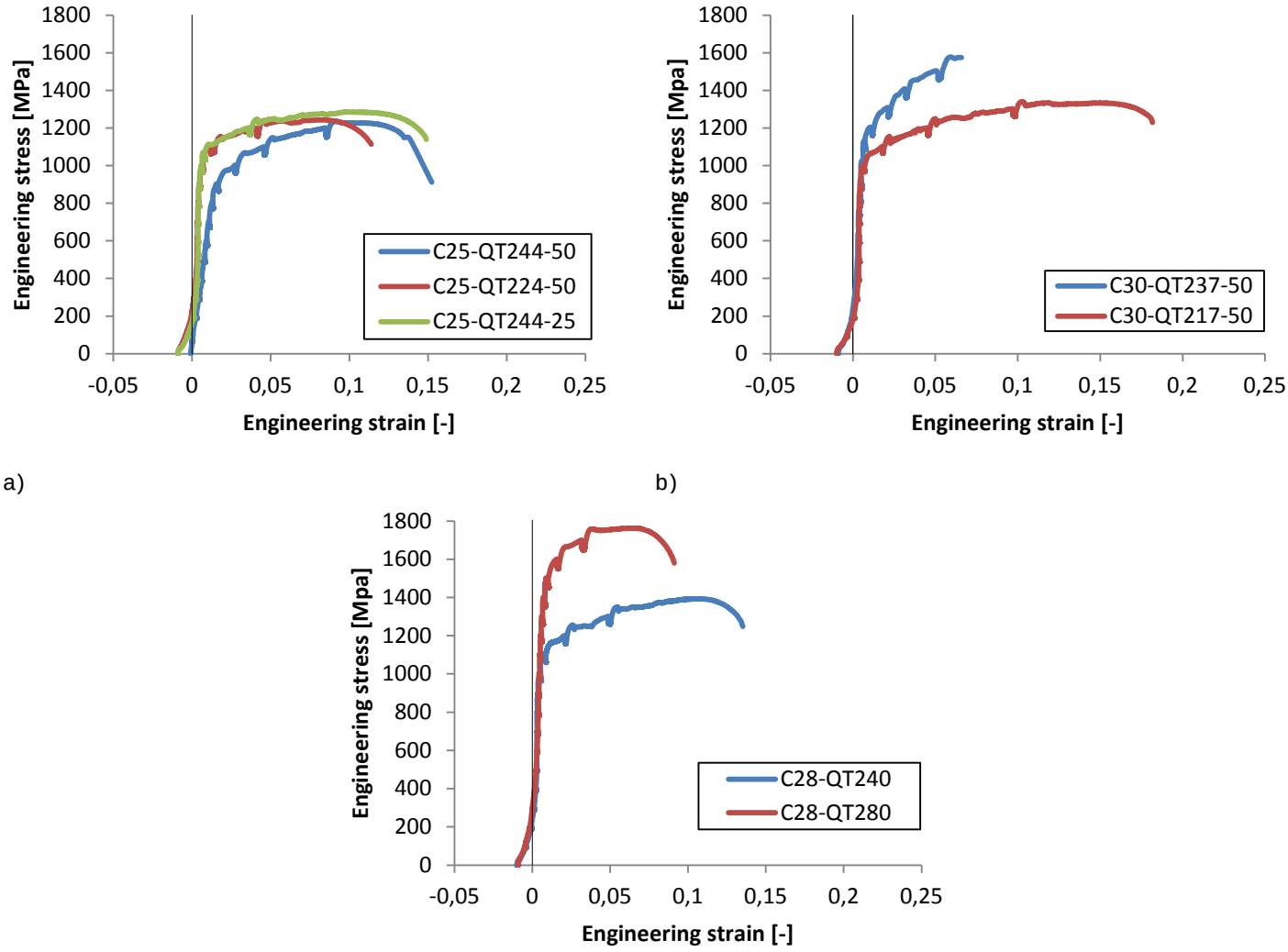

Figure 4.2: Corrected Stress-strain plot for a) the C25 material, b) the C30 material and c) the C28 material

Table 4.2: Mechanical properties obtained from OCAS NV and Thyssenkrupp Steel Europe AG

Sample material	Sample orientation	$R_{p\,0,2}$, MPa	Young's modulus, GPa	R_m (UTS), MPa	Strain at UTS
C25-QT244-50	TD	1008	207	1345	0,09
C25-QT224-50	TD	1092	213	1354	0,065
C25-QT244-25	TD	832	208	1345	0,09
C30-QT237-50	TD	832	207	1435	0,099
C30-QT217-50	TD	986	208	1431	0,096
C28-QT240	TD	1036	-	1403	0,112
C28-QT280	TD	1129	-	1784	0,042

Table 4.3: Measured mechanical properties obtained with Deben Microtest machine

Sample material	Sample orientation	$R_{p\,0,2}$, MPa	Young's modulus, GPa	R_m (UTS), MPa	Strain at UTS
C25-QT244-50	TD	975	*16,7*	1230	0,13
C25-QT224-50	TD	1040	*18,0*	1240	0,135
C25-QT244-25	TD	1130	*16,4*	1285	0,15
C30-QT237-50	TD	1210	*18,0*	1575	0,12
C30-QT217-50	TD	1055	*16,8*	1333	0,20
C28-QT240	TD	1110	*18,1*	1395	0,16
C28-QT280	TD	1565	*21,6*	1760	0,125

Table 4.4: Corrected mechanical properties obtained with Deben Microtest machine

Sample material	Sample orientation	$R_{p\,0,2}$, MPa	Young's modulus, GPa	R_m (UTS), MPa	Strain at UTS
C25-QT244-50	TD	900	66	1345	0,09
C25-QT224-50	TD	1070	184	1354	0,08
C25-QT244-25	TD	1070	194	1345	0,095
C30-QT237-50	TD	1145	207	1575	0,062
C30-QT217-50	TD	987	198	1431	0,14
C28-QT240	TD	1098	203	1403	0,10
C28-QT280	TD	1499	203	1784	0,064

The corrected mechanical properties are in range with the mechanical properties of the suppliers, only the C25-QT244-50 tensile sample has a Young's modulus deviation. For all the further calculations the corrected values are used. The C25-QT244-50 was the first sample tested in the In situ X-ray diffraction experiment and it led to a linear stress-strain curve. All the other samples that where tested afterwards have also a starting convex deviation from the starting linear stress-strain curve. After the first test there was an error in the Deben Microtest machine with the recording of the force at certain time intervals. It seems that the time intervals increased which is not possible due to the fact that the time interval was fixed on 0,5 seconds at the start of the experiment. The time intervals only increased above a certain force which was lower than the yield strength. The error was only observed for the C25-QT224-50 and the C30-QT237-50 sample material. For the remaining samples this error was not seen.

The mechanical properties obtained from the in situ X-ray diffraction experiments show that there are different yields strengths, ultimate tensile strengths (UTS) and UTS at different strains.

The C25-QT244-50 sample was the first sample tested in the In situ X-ray diffraction experiment and it obtained a deviation from the linear stress-strain curve whereby the Young's modulus has a lower value then all the other samples that where tested afterwards. The difference in yield stresses, UTS and strains at UTS of the different tensile specimens can be related to the applied heat treatment of the Q&P material.

For the C25 material the difference in mechanical properties between the C25-QT244-50, C25-QT224-50 and C25-QT244-25 is more difficult to explain due to the low Young's modulus value of C25-QT244-50 that shifts the stress-strain curve so that a influence of the QT and Pt on the yield strain (e_t) and strain at UTS (A_{gt}) of the C25 material is not quite clear.

For the C30 material there is a substantial difference in mechanical properties between C30-QT237-50 and C30-QT217-50 in terms of UTS and strain at UTS. The C30-QT217-50 has a larger strain at UTS which maybe can related to a larger initial retained austenite phase in comparison with C30-QT237-50.

For the C28 material there is a large difference between the two tensile specimens related to the heat treatment. The C28-QT240 consists of a retained austenite and martensite phase so that there can be a phase transformation occurring where there is stress or strain applied. Whereas C28-QT280 is mainly martensite so that the mechanical properties can be related to the martensite phase if the retained austenite phase is the second phase in this microstructure with a small influence.

4.3. Strain hardening

The strain hardening is an indication of the material to postpone the necking of the tensile specimen. When the necking is postponed the strain at UTS will increase. The strain hardening is described with the instantaneous strain hardening defined as coefficient.

$$n = \frac{\partial \ln \sigma}{\partial \ln \epsilon} = \frac{\ln \sigma_2 - \ln \sigma_1}{\ln \epsilon_2 - \ln \epsilon_1} \qquad (4.2)$$

Where $\sigma_{1,2}$ is the true stress and σ_1 has a lower value then σ_2 and $\epsilon_{1,2}$ is the true strain where ϵ_1 has a lower value then ϵ_2. The n -values are only obtained below the UTS due to the experimental setup of stress steps where the strain is not a controlling parameter (see chapter 3.7). When the instantaneous strain hardening in the specimen has a value 1 or larger then there is elastic strain and if the value becomes smaller than 1 then there is plastic strain. This will not imply that this transition point is the strain at yield stress. The n-value vs. the true strain can be seen in figure 4.3.

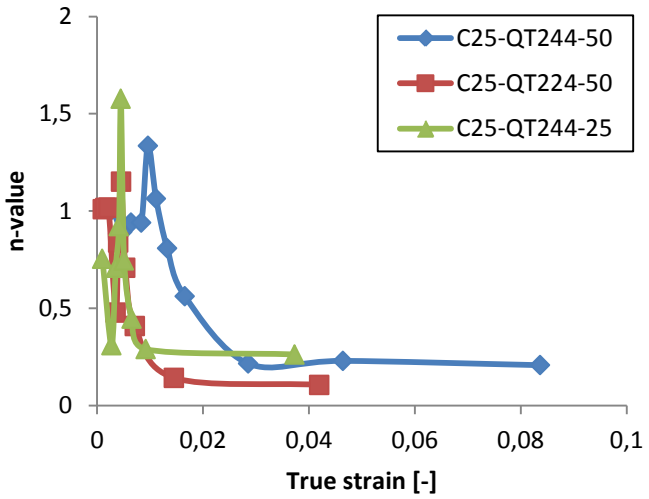

a)

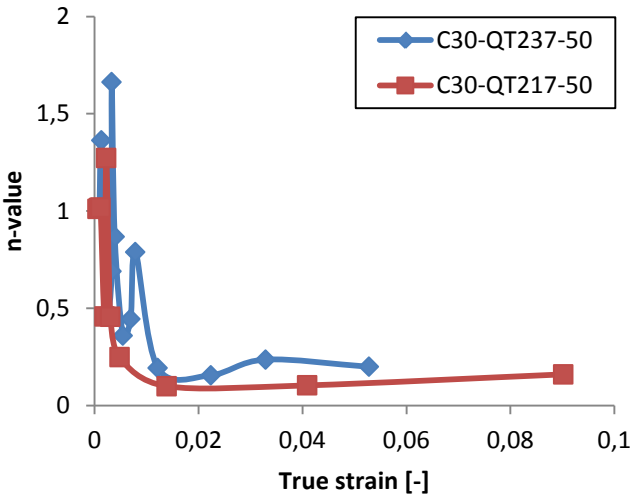

b)

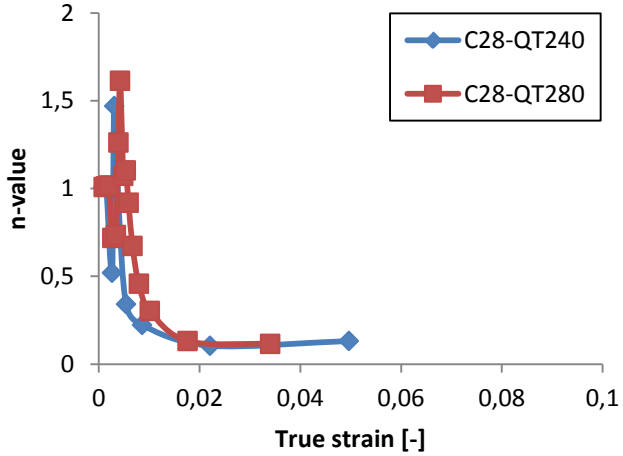

c)

Figure 4.3: n-value vs. the true strain for a) the C25 material, b) the C30 material and c) the C28 material

In the elastic part of the tensile specimen the n -value has a large scatter and in the plastic part the strain hardening value is in the range of 0,1 to 0,2. The measured n -values are lower in relation to other steel materials (n-value of 0,2 to 0,5). The stable n -value implies that strain hardening is stable until the UTS so that strain hardening has its contribution to the 'larger' strain. For the C25 material there is a stable strain hardening until the UTS so that the TRIP-effect has its contribution the increased plastic strain. For the C30 material there is for the C30-QT217-50 in comparison with C30-QT237-50 an increase of strain hardening and this can be related to a more stable retained austenite phase which increases the maximum strain. For the material C28-QT240 there is a larger contribution of strain hardening to the strain and this contribution can be related to the TRIP-effect.

4.4. Retained austenite volume fraction

For obtaining the retained austenite volume fraction the $\{111\}_\gamma$, $\{200\}_\gamma$, $\{220\}_\gamma$ and $\{311\}_\gamma$ reflections of retained austenite and the $\{110\}_{\alpha'}$, $\{200\}_{\alpha'}$, $\{211\}_{\alpha'}$ and $\{220\}_{\alpha'}$ reflections of martensite were used. Two Bragg angle ranges were selected for obtaining retained austenite volume fraction. The two ranges, with the obtained reflections and Bragg angles, can be seen in table 3.4.

To investigate if there is a preferred orientation (texture) in the material the first diffraction range is used.

First the peak intensity ratio between the $\{220\}_\gamma$ / $\{200\}_\gamma$ is calculated and if it is between the theoretical intensity ratio of 1,2 and 1,8 with a mean value of 1,47 then it is assumed that there is no preferred orientation in the material (see table 4.5) [49].

Table 4.5: Peak intensity ratio between the austenite peaks $\{220\}_\gamma$ / $\{200\}_\gamma$

Specimen material	C25-QT244-50	C25-QT224-50	C25-QT244-25	C30-QT237-50	C30-QT217-50	C28-QT240	C28-QT280
$\{220\}_\gamma$ / $\{200\}_\gamma$	3,09	2,70	2,92	4,13	2,25	1,68	1,07

From table 4.5 only C28-QT240 can be considered as a material without preferred orientation.

Second there is preferred orientation in almost all the materials so that a selection of peaks is needed for the measuring of the retained austenite volume fraction. With the texture parameter [50] each diffraction peak can be individual calculated with equation 4.3.

$$P_{hkl}^{\alpha\prime} = \frac{\frac{I_{hkl}^{\alpha\prime}}{R_{hkl}^{\alpha\prime}}}{\frac{1}{n_{\alpha\prime}}\sum_0^{n_{\alpha\prime}}\left(\frac{I_{\alpha\prime}}{R_{\alpha\prime}}\right)} \tag{4.3}$$

Where $P_{hkl}^{\alpha\prime}$ is the texture parameter of the martensite phase with the hkl miller indices, $I_{hkl}^{\alpha\prime}$ is the obtained intensity from a certain martensite peak, $R_{hkl}^{\alpha\prime}$ is the calculated intensity of martensite from a certain martensite peak, $I_{\alpha\prime}$ is the obtained intensity of the all the martensite peaks, $R_{\alpha\prime}$ is the calculated intensity of martensite from all the martensite peaks and $n_{\alpha\prime}$ is the total amount of intensity peaks used for the martensite phase. The intensities R_{hkl}^{γ} and $R_{hkl}^{\alpha\prime}$ are calculated with the structure sequence of Jatczak [49] in Appendix C due to the difference of carbon concentration in the samples. The R-values can be seen in table 4.6.

Table 4.6: Calculated R-value

Sample material	R_{hkl}							
	{111}γ	{200}γ	{220}γ	{311}γ	{110}α'	{200}α'	{211}α'	{220}α'
C25-QT244-50	88,8644	38,1947	20,8961	32,7243	114,9223	14,9632	31,7208	15,0993
C25-QT224-50	88,8644	38,1947	20,8961	32,7243	114,9223	14,9632	31,7208	15,0993
C25-QT244-25	88,8644	38,1947	20,8961	32,7243	114,9223	14,9632	31,7208	15,0993
C30-QT237-50	88,8622	38,1937	20,8957	32,7231	114,1997	14,8681	31,3501	14,7879
C30-QT217-50	88,8622	38,1937	20,8957	32,7231	114,1997	14,8681	31,3501	14,7879
C28-QT240	88,8637	38,1945	20,8959	32,7236	114,5171	14,9098	31,5121	14,9235
C28-QT280	88,8637	38,1945	20,8959	32,7236	114,5171	14,9098	31,5121	14,9235

When $P_{hkl}^{\alpha' or \gamma}$ > 1 then the hkl planes are the preferentially oriented planes parallel to the plane of selection. When $P_{hkl}^{\alpha' or \gamma}$ < 1 these planes are preferentially avoided and if $P_{hkl}^{\alpha' or \gamma}$ = 1 there is a random orientation [50].

In table 4.7 the $\frac{1}{n_\gamma}\sum_0^{n\gamma}\left(\frac{I_\gamma}{R_\gamma}\right)$ or $\frac{1}{n_{\alpha'}}\sum_0^{n_{\alpha'}}\left(\frac{I_{\alpha'}}{R_{\alpha'}}\right)$ and the P_{hkl}^{γ} or $P_{hkl}^{\alpha'}$ of the first range are shown for the different materials at the initial value 0 MPa of stress.

Table 4.7: Texture parameter of the range 1 hkl planes

Sample material	$\frac{1}{n}\sum_0^n\left(\frac{I}{R}\right)$		P_{hkl}							
	γ	α'	$\{111\}_\gamma$	$\{200\}_\gamma$	$\{220\}_\gamma$	$\{311\}_\gamma$	$\{110\}_{\alpha'}$	$\{200\}_{\alpha'}$	$\{211\}_{\alpha'}$	$\{220\}_{\alpha'}$
C25-QT244-50	3,7708	21,3082	0	0,5114	2,8876	0,6010	0,2761	1,8035	1,6975	0,2228
C25-QT224-50	3,2794	21,0334	0,0662	0,5539	2,7285	0,6514	0,3762	1,8258	1,5742	0,2238
C25-QT244-25	2,8720	20,9629	0,0480	0,5536	2,9580	0,4404	0,4360	1,7969	1,5855	0,1817
C30-QT237-50	2,5255	19,5848	0,0124	0,4095	3,0918	0,4863	0,3616	1,8500	1,7085	0,0799
C30-QT217-50	3,8927	19,4141	0,0371	0,6869	2,8274	0,4487	0,4318	1,7765	1,6387	0,1530
C28-QT240	5,2613	24,0694	0,1663	0,7801	2,3996	0,6540	0,5486	1,6920	1,3766	0,3828
C28-QT280	1,0680	25,6816	0	1,1352	2,2228	0,6420	0,6613	1,5801	1,2926	0,4660

The $\{200\}_\gamma$ & $\{220\}_\gamma$ planes of retained austenite and $\{200\}_{\alpha'}$ & $\{211\}_{\alpha'}$ planes of martensite have P_{hkl} value larger than 1. The material is 'highly' textured and this can have an influence on the retained austenite volume fraction measurements. In order to determine the texture stability during the mechanical deformation the texture parameters are calculated with range 2 (see chapter 3.7) at each stress step for the $\{220\}_\gamma$ and $\{200\}_{\alpha'}$ planes. The texture stability can be seen in Appendix D. Also the $\{220\}_\gamma$ and $\{200\}_{\alpha'}$ planes have a Bain orientation-relation [51] which each other. The Bain orientation-relation uses the Bain strain (BS) model of Furubayashi et al. [52] and discussed by Ray et al. [53] which is based on the relation of the applied tensile stress which translate into two compression stresses of the Bain compression axis (BSA). The $\{220\}_\gamma$ and $\{200\}_{\alpha'}$ planes are used to calculate retained austenite volume fraction with equation 4.4.

$$f^{\gamma} = \frac{\frac{1}{n_1}\sum_1^{n_1}\frac{I_{hkl}^{\gamma}}{R_{hkl}^{\gamma}}}{\frac{1}{n_2}\sum_1^{n_2}\frac{I_{hkl}^{\alpha'}}{R_{hkl}^{\alpha'}}+\frac{1}{n_1}\sum_1^{n_1}\frac{I_{hkl}^{\gamma}}{R_{hkl}^{\gamma}}} \quad (4.4)$$

Where I_{hkl}^{γ} is the obtained intensity from the retained austenite peaks, $I_{hkl}^{\alpha'}$ is the obtained intensity from the marteniste peaks, R_{hkl}^{γ} is the calculated intensity of retained austenite, $R_{hkl}^{\alpha'}$ is the calculated intensity of martensite and $n_{1,2}$ are the amount of intensity peaks used for each phase. The results of the retained austenite volume fraction are shown in figure 4.4, the error bars indicate the Counting Statistical Error (CSE) for X-ray diffraction [54].

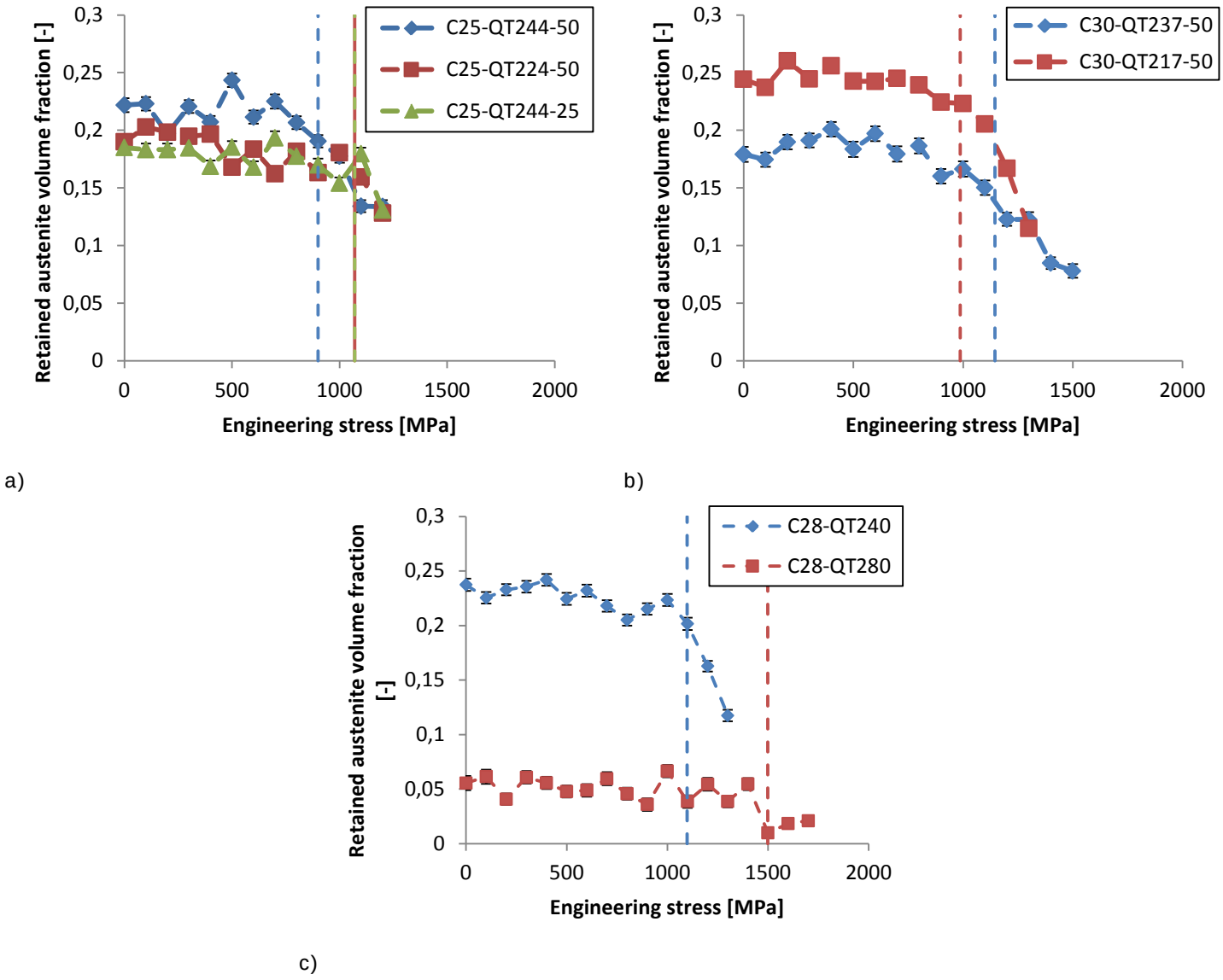

Figure 4.4: Retained austenite volume fraction vs. Engineering stress plot for a) the C25 material, b) the C30 material and c) the C28 material, yield stress are indicated with vertical dotted lines

The initial retained austenite volume fraction is between 0,05 and 0,25 (see table 4.1). The decrease in retained austenite volume fraction start at stress values nearby the yield stress. Remark: the yield stress of the C25-QT224-50 and C25-QT244-25 material has the same value so that their appear in one single (dotted) line see figure 4.4 a).

4.4.1. The initial retained austenite volume fraction

The initial retained austenite volume fraction (f_0^γ) which is measured with In situ X-ray diffraction is compared to the austenite volume fraction (f_{QT}^γ) at the quenching temperature (QT) which has been calculated (see table 4.8). The Koistinen–Marburger [7] equation 4.5 which is an adjustment from equation 2.6.

$$f_{QT}^\gamma = e^{(-1{,}1*10^{-2}(M_s - QT))}\ (°C) \qquad (4.5)$$

Where M_s is the martensite start temperature and QT is the quenching temperature.

Table 4.8: Austenite volume fraction at QT, initial retained austenite volume fraction and difference

Specimen material	C25-QT244-50	C25-QT224-50	C25-QT244-25	C30-QT237-50	C30-QT217-50	C28-QT240	C28-QT280
f_{QT}^γ	0,405	0,325	0,405	0,484	0,388	0,408	0,634
f_0^γ	0,222	0,190	0,185	0,179	0,244	0,237	0,055
Δf^γ	0,183	0,135	0,220	0,305	0,144	0,171	0,579

The difference between the initial retained austenite volume fraction (f_0^γ) and the austenite volume fraction (f_{QT}^γ) can give an indication of the QT and carbon diffusion in the partitioning stage in relation with the Pt. For the C25 materials there is an indication that the C25-QT224-50 has less decrease of austenite and therefore a more stable austenite phase than C25-QT244-50. The decrease in the partitioning time (Pt) will result in a lower initial retained austenite volume fraction which can be seen in the retained austenite volume fraction values of C25-QT244-50 and C25-QT244-25. For the C30 material there is a indication that the C30-QT237-50 has an higher decrease in austenite volume faction than C30-QT217-50 material. The C28 materials are obtained with two different heat treatments (see chapter 3.3) so that a comparison between the C28-QT240 and C28-QT280 materials in relation with the austenite volume fraction is not representative.

4.4.2. The retained austenite volume fraction at mechanical deformation

When the normalized retained austenite volume fraction is compared with the engineering stress divided by the yield stress. The decrease in retained austenite volume fraction starts in the range of the yield stress of the materials see figure 4.5 (error bars indicate the standard error).

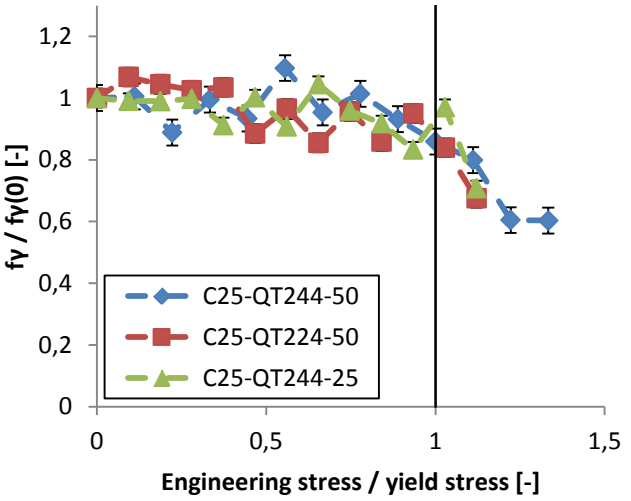

a)

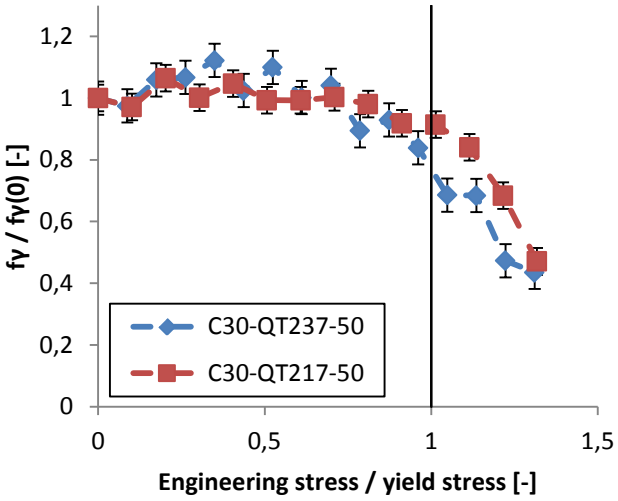

b)

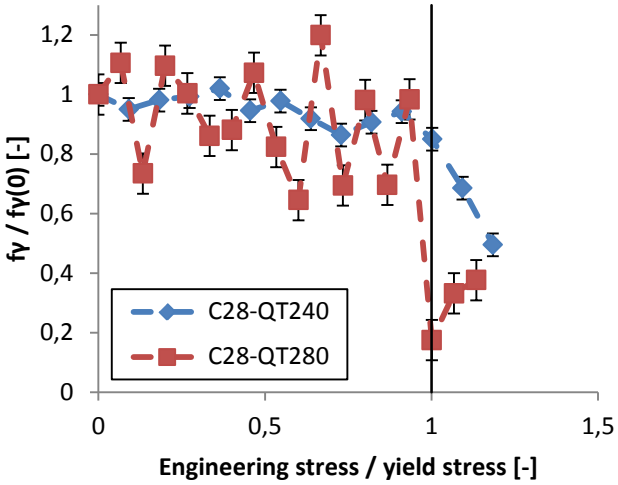

c)

Figure 4.5: Normalized retained austenite volume fraction vs. Engineering stress / yield stress plot for a) the C25 material, b) the C30 and c) the C28 material

For the TRIP-effect the relation between the retained austenite volume fraction and the (engineering) strain is important. The retained austenite volume fraction starts to decrease at a certain value when the strain is increased. This is due to the phase transformation from the retained austenite phase to the martensite phase. The decrease of retained austenite can be seen in figure 4.6

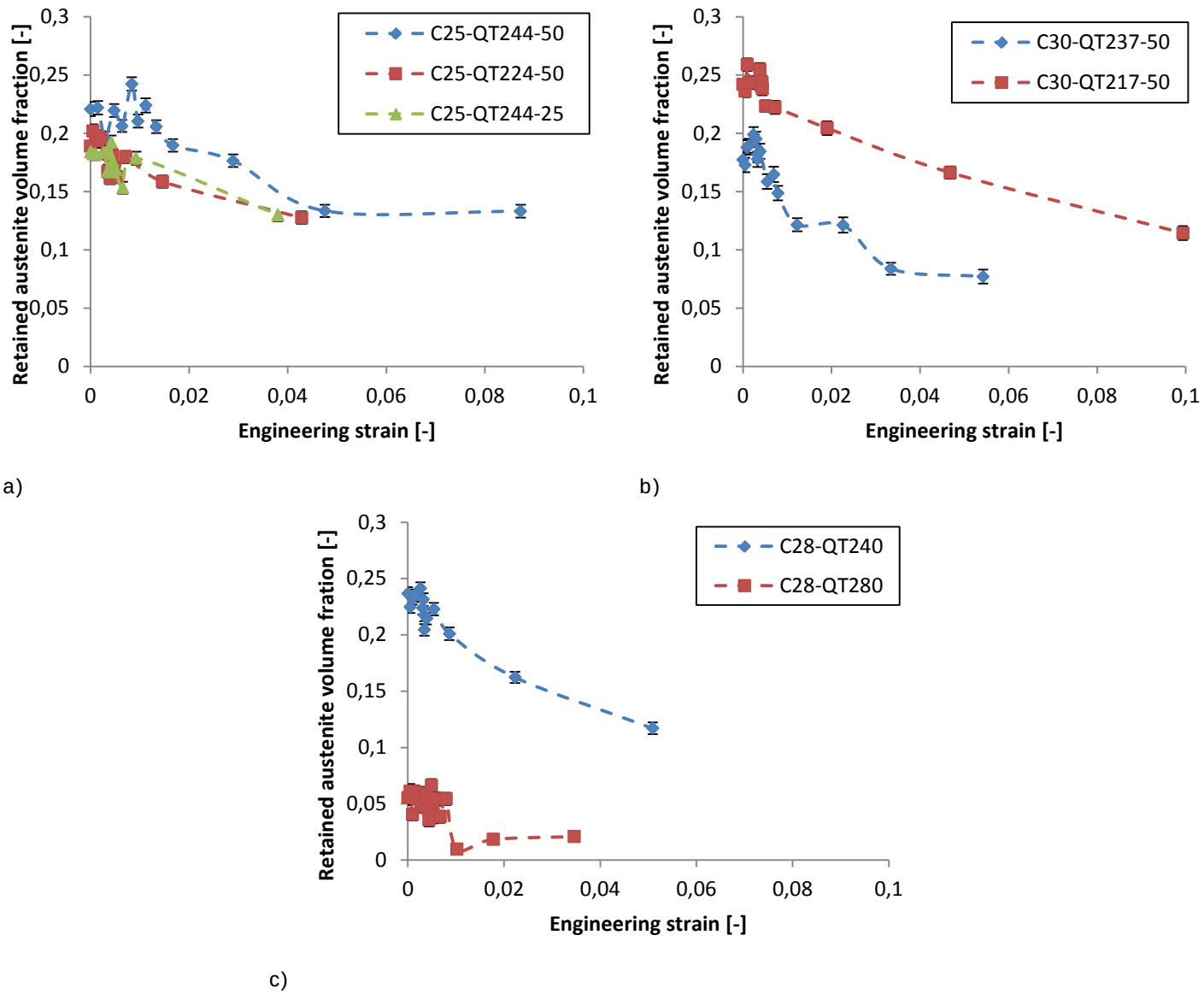

Figure 4.6: Retained austenite volume fraction decrease with strain for a) the C25 material, b) the C30 material and c) the C28 material

The retained austenite volume fraction of the materials start to decrease when the material enters the strain region of plastic deformation. There is a minimal scattering observed in the elastic strain region of the retained austenite phase and this scattering in the elastic strain region is also observed in the texture parameter of the austenite phase (see Appendix D). After the scatter there is a normal decrease in the retained austenite fraction. If the scatter of the retained austenite phase is not related to the x-ray diffraction measurement errors then it could be texture evolution which is a stress-assisted transformation investigated by Hilkhuijsen et al. [55]. Their describing for a austenitic stainless steel that there is an influence of austenite texture on the retained austenite to martensite phase transformation. In their experiment an uniaxial tensile test is performed on the rolling direction (RD) and the transverse direction (TD) of the material. For the phase transformation in the RD the martensite texture has a large

relation with the parent austenite texture. For the phase transformation in TD there are two mechanisms working on the material. First there is a phase transformation and second there is a texture evolution (crystal rotation) when an mechanical deformation is applied and there is little relation between the martensite texture and the parent austenite texture.

4.4.3. The retained austenite volume fraction stability

The stability of the retained austenite can be quantified as the kinetics of the deformation-induced martensitic phase transformation as a function of the true strain. To indicate the stability of the retained austenite the Ludwigson and Berger relation [56] is used.

$$\frac{1}{f^{\gamma}} - \frac{1}{f_0^{\gamma}} = \left(\frac{k_p}{p}\right)\epsilon^p \qquad (4.7)$$

Where f^{γ} is the retained austenite volume fraction at strain values larger than one, f_0^{γ} is the initial retained austenite volume fraction, k_p is a constant relating to the stability of the retained austenite with respect to the deformation, p is the autocatalytic effect of martensite phase transformation to accelerate the creation of additional martensite and ϵ is the true strain. A higher k_p indicates a less stable retained austenite. The autocatalytic effect (p) have different values for different austenitic / martensitic materials. Such as for duplex stainless steels (DP) $p = 2$, for austenitic stainless steels $p = 3$ and for TRIP steels $p = 1$. When the value of f^{γ} is obtained at the elastic deformation is lower than the f_0^{γ} than the absolute value of $\frac{1}{f^{\gamma}} - \frac{1}{f_0^{\gamma}}$ is used. Otherwise k_p or p value becomes negative. In figure 4.7 the change of $\frac{1}{f^{\gamma}} - \frac{1}{f_0^{\gamma}}$ with true strain can be observed. A lower inclination of the linear line indicates that the material is more stable.

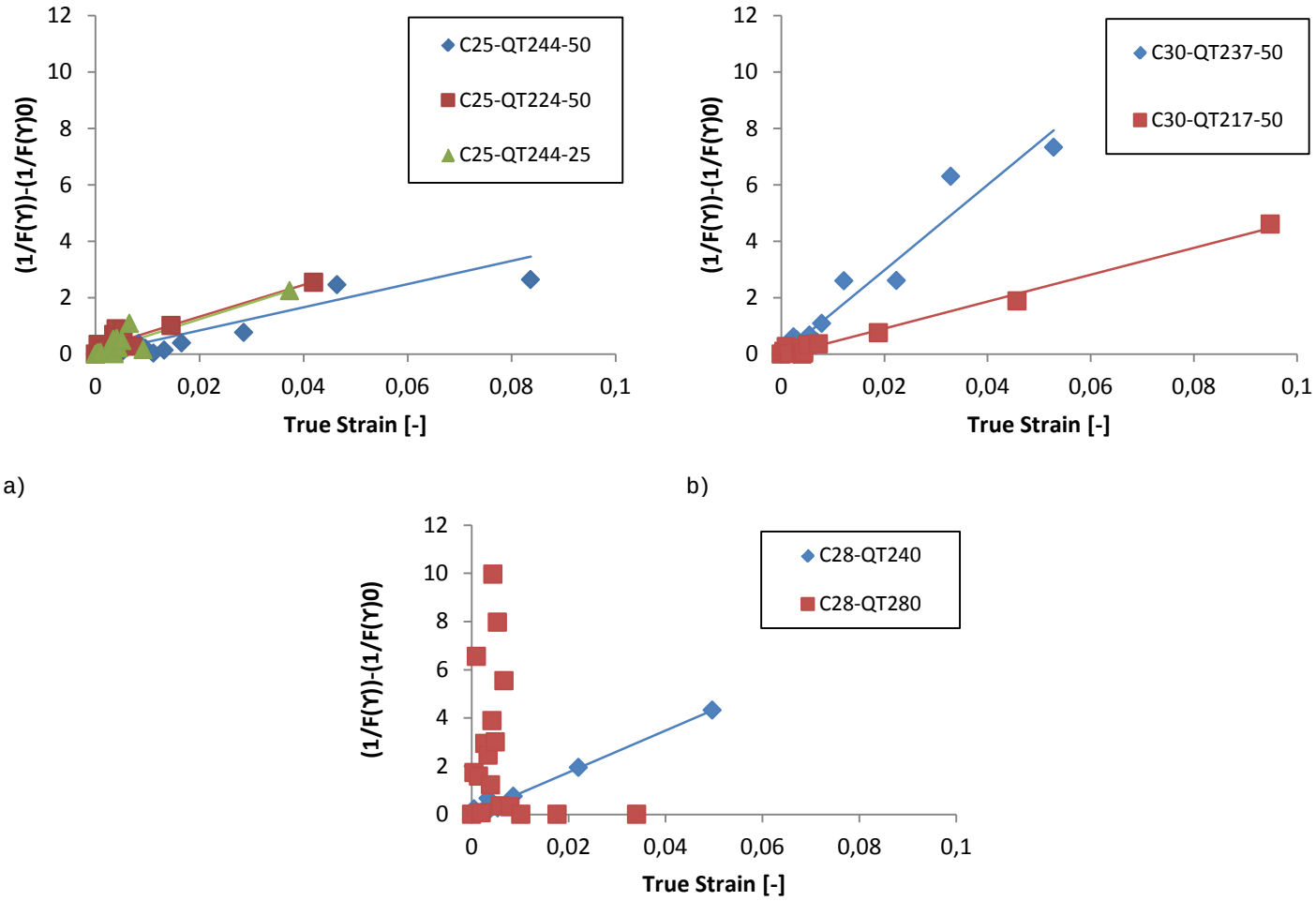

Figure 4.7: Change of $\frac{1}{f^{\gamma}} - \frac{1}{f_0^{\gamma}}$ with true strain for a) the C25 material, b) the C30 material and c) the C28 material

In a 'normal' Ludwigson and Berger relation there is a significant decrease of the f^{γ} after the f_0^{γ} when true strain is applied. This can be related to the amount of f^{γ} measured at plastic deformation.

In this case the f^{γ} has a scatter in the elastic deformation and start to decrease (increase of the $f^{\alpha\prime}$) in the plastic deformation. When plastic deformation started, the f^{γ} start to decrease until the f^{γ} reached a minimum value. The lowest obtained f^{γ} is a value below the UTS of the material due to the measuring procedure of stress steps (see chapter 3.7). The change of f^{γ} in relation with the f_0^{γ} below the yield stress of the material is that the points are scattered (see figure 4.6). Below the yield stress of the material the stability is lower which correlates in the data points. Above the yield stress of the material the points can be fitted to a linear line (figure 4.7). In order to indicate the accuracy of the linear line the linear correction coefficient is calculated. The average values of k_p, p and the linear correlation coefficient ($r(x,y)$) of the linear line for the samples are shown in table 4.9.

Table 4.9: Fitted k_p, p values (elastic-plastic deformation) and the linear correlation coefficient for the different material

Sample material	k_p	p	$r(x,y)$
C25-QT244-50	1,0±0,3	0,23±0,06	0,923
C25-QT224-50	2,4±0,2	0,45±0,04	0,930
C25-QT244-25	2,3±0,2	0,48±0,06	0,901
C30-QT237-50	2,2±0,2	0,40±0,05	0,971
C30-QT217-50	1,4±0,2	0,46±0,05	0,993
C28-QT240	2,1±0,2	0,45±0,05	0,991
C28-QT280	2,4±0,2	0,22±0,04	-

The k_p values of the samples are very low compared to values that are already reported in several other articles (K_p of 16 until 120) [15, 17]. This can be related to the high f_0^γ value and the small decrease in f^γ when strain is increased (see figure 4.6). The p values are in range with the already reported in several other articles [15, 17]. The initial stability of the retained austenite (k_p) is related to the amount of data points 'scattering' in figure 4.6. The autocatalytic effect (p) of martensite to form new martensite is influence by QT and Pt for the C25 material. For the C30 material the influence of QT has little to none effect on p. The C28-QT280 material has a high amount of "scattering" of the data point and a relative low linear correction coefficient compared with the other samples. The explanation could be that the sample has undergone only a one-step non-isothermal annealing process of the material, so that the amount of initial and final retained austenite volume fraction is low in comparison with the other C28-QT240 material. To make a good comparison of the k_p and p values in relation with other articles [15, 17] only retained austenite volume fraction of the plastic deformation are displayed in table 4.10.

Table 4.10: Fitted k_p, p values (plastic deformation) and the linear correlation coefficient for the different material

Sample material	k_p	p	$r(x,y)$
C25-QT244-50	2,4±0	0,36±0,04	0,755
C25-QT224-50	2,3±0,2	0,45±0,04	0,997
C25-QT244-25	2,4±0,2	0,45±0,09	0,943
C30-QT237-50	2,2±0,2	0,40±0,05	0,919
C30-QT217-50	2,0±0,1	0,37±0,04	0,966
C28-QT240	2,4±0	0,34±0,05	0,999
C28-QT280	2,6±0	0	-

The k_p values have slight increase in comparison with table 4.9 due to that the material is already plastic deforming and the stability of the retained austenite becomes lower. The p values are acquired at larger strain values so that autocatalytic effect has already decreased due to the increase of the amount of the martensite phase.

4.5. Lattice parameter

The lattice parameters of the retained austenite (fcc) and martensite (bcc) phase react differently to the mechanical deformation. Under the influence of the elastic strain the lattice parameter will decrease due to contraction of the tensile specimen when measured with parallel beam X-ray diffraction. The contraction will shift the intensity peak which can be measured with Bragg angle. The change in lattice parameter of the $\{220\}_{\gamma}$ plane and $\{200\}_{\alpha'}$ plane can be calculated with the following equations 3.2, 3.3 and 3.3.

An increase of the lattice parameter will reduce the Bragg angle. The lattice parameter for the retained austenite $\{220\}_{\gamma}$ plane has continuous decrease with mechanical deformation while for the martensite $\{200\}_{\alpha'}$ plane there is a minimum lattice parameter (range of the yields stress the vertical dotted line) after which the lattice parameter starts to increase again with mechanical deformation and this can be seen in figure 4.8 for example. In figure 4.8 the lattice parameters of both phases are converted into the atomic radius for comparison with equation 4.8 for the fcc unit cell and equation 4.9 for the bcc unit cell.

$$R_{fcc} = \frac{a}{2\sqrt{2}} \tag{4.8}$$

$$R_{bcc} = \frac{a\sqrt{3}}{4} \tag{4.9}$$

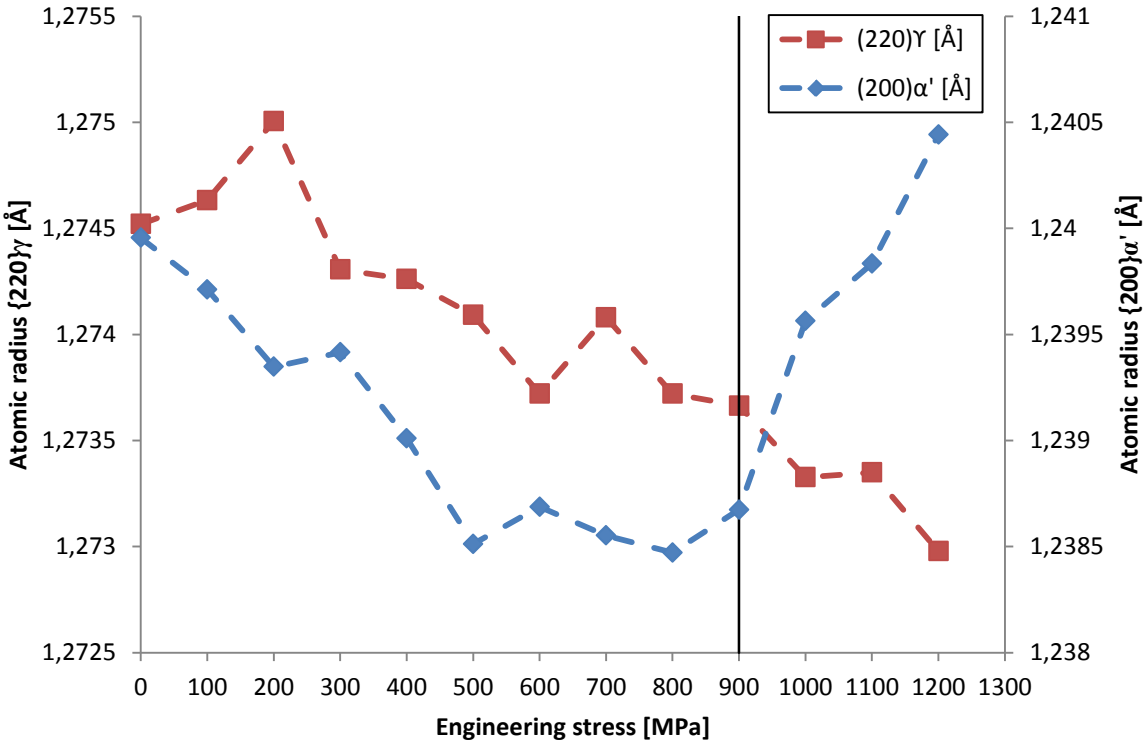

Figure 4.8: Atomic radius of retained austenite (γ) and martensite (α') phases of C25-QT244-50

The lattice parameter martensite of the $\{200\}_{\alpha'}$ plane of the C25, C30, C28 material and the vertical line of yield stresses can be seen in figure 4.9.

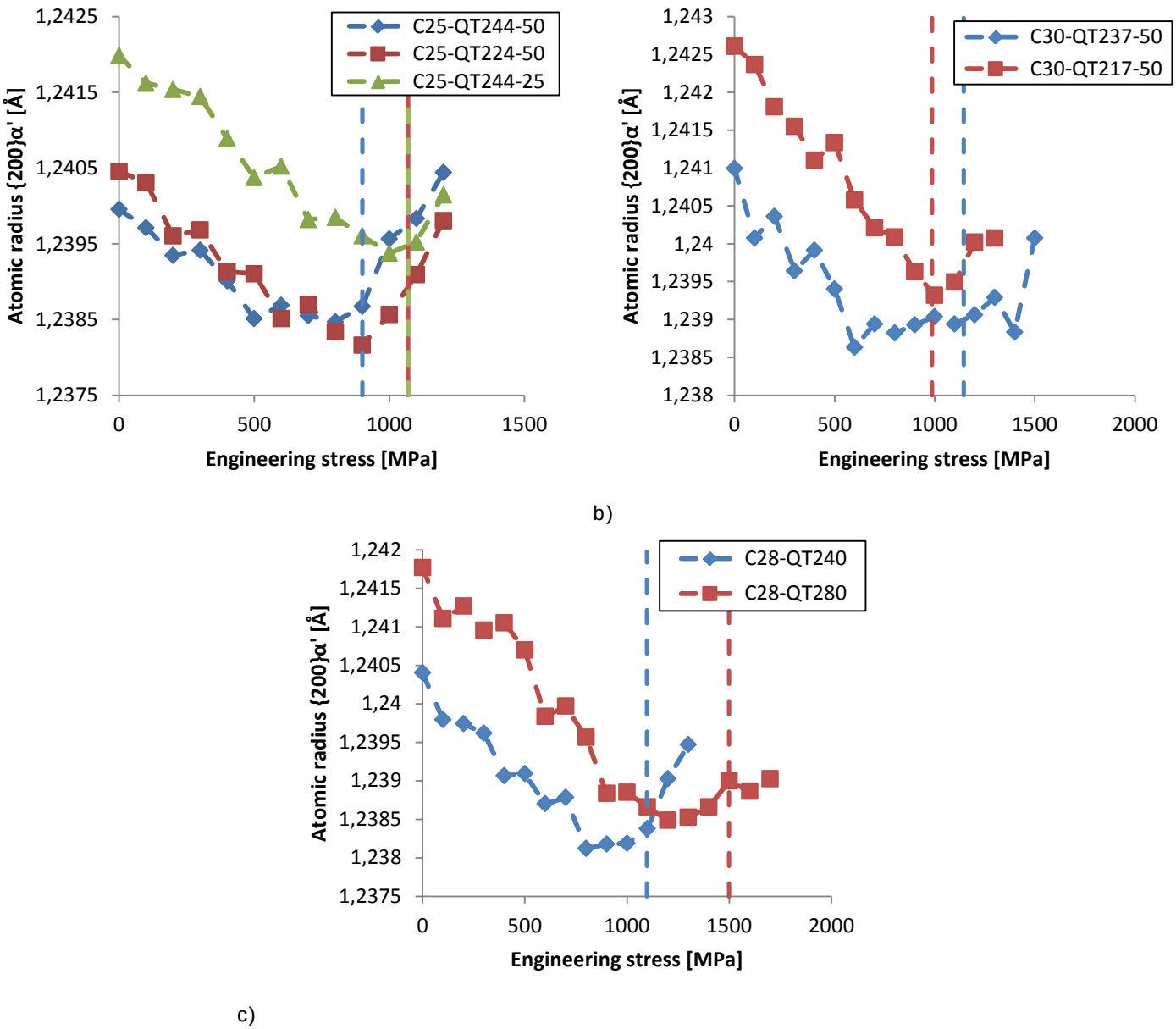

Figure 4.9: Atomic radius of the {200}α' planes vs. engineering stress for a) the C25 material, b) the C30 material and c) the C28 material

4.6. The carbon concentration

4.6.1. The initial carbon concentration

To verify the initial carbon concentration at room temperature (RT) the total driving force for phase transformation ($\Delta G^{\gamma \rightarrow \alpha'}$) of retained austenite to martensite is calculated at the M_s temperature. The phase transformation is an athermal phase transformation which not requires to overcome a thermal activation barrier only a certain temperature which is time independent [39]. The total driving force can be calculated with the following equation.

$$\Delta G^{\gamma \rightarrow \alpha'} = \Delta G^{ch} + \Delta G^{\sigma} \qquad (4.10)$$

Where the ΔG^{ch} is the chemical driving force and ΔG^{σ} is the mechanical driving force. The chemical driving force (ΔG^{ch}) is independent for the concentration and type of alloying elements. At the M_s temperature the total driving force consists only of a chemical driving force (ΔG^{ch}) (see figure 2.5 and figure 4.10) it is assumed to have a constant value [57].

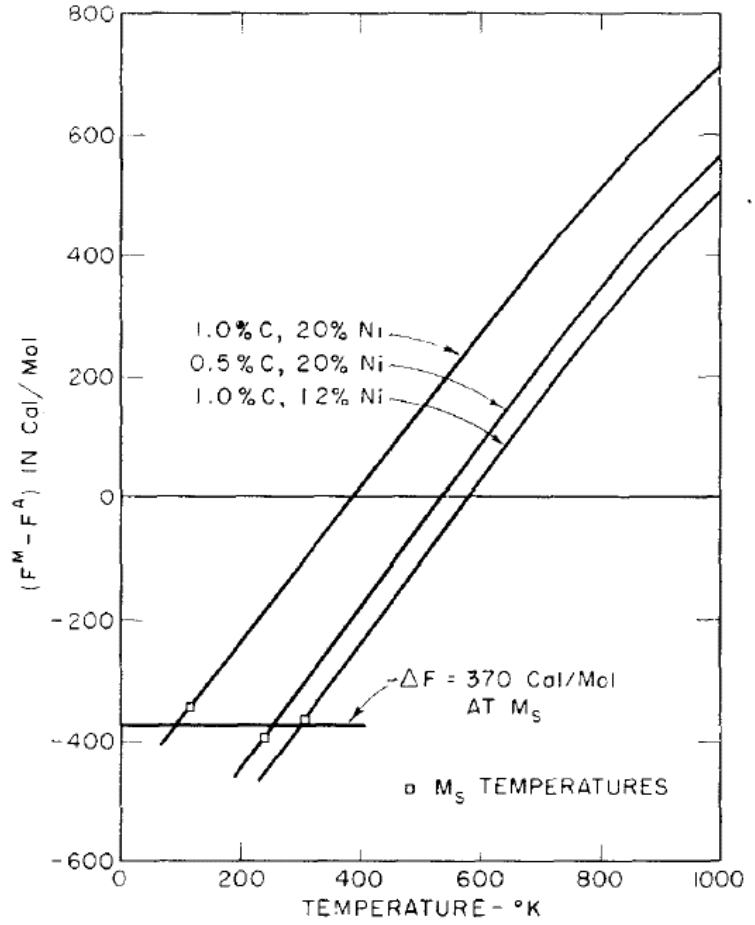

Figure 4.10: Change in chemical free energy attending to the austenite to martensite phase transformation in Fe-C-Ni alloys [57]

The chemical driving force can be obtained with a thermodynamic software such as Thermocalc®. The authors knowledge of this software program limited. Therefore the chemical driving force is calculated with a formula derived from Thermcalc® of G.N. Haidemenopoulos et al. [58].

$$\Delta G^{ch} = -5157{,}3 + 57979X_c - 37{,}353X_cT + 8{,}28T \qquad (4.11)$$

Where X_c is the mole fraction of carbon in the austenite and T is the temperature in Celsius. The chemical driving force of austenite with the initial carbon concentration at M_s temperature is the maximum (due to negative free energy) driving force for martensitic phase transformation for stable austenite at the M_s temperature. To acquire stable retained austenite at room temperature (RT) ($M_{s(@\,RT)}$) the driving force for martensitic phase transformation has to be equivalent to the driving force for phase transformation at the M_s temperature. To obtain the $M_{s(@\,RT)}$ temperature the carbon concentration needs to increase so that the retained austenite is stable at RT. The increase of carbon concentration via diffusion in the retained austenite is obtained in the partitioning stage of the heat treatment.

The chemical driving force of the retained austenite at M_s temperature with initial carbon concentration is used to calculate the carbon concentration of stable retained austenite at room temperature (RT) with equation 4.11 see table 4.11.

Table 4.11: The initial carbon concentration of stable retained austenite at room temperature

Sample material	M_s [°C]	ΔG^{ch} [J/mol]	X_C at RT(24°C) [mass%]	
			Experimental	Calculated
C25-QT244-50	325	-1933	1,11	1,14
C25-QT224-50	325	-1933	1,12	1,14
C25-QT244-25	325	-1933	1,16	1,14
C30-QT237-50	301	-2015	1,10	1,10
C30-QT217-50	301	-2015	1,17	1,10
C28-QT240	320	-1917	1,06	1,14
C28-QT280	320	-1917	1	1,14

The experimental and the calculated carbon concentration values are in the range with each other. If the calculated (with equation 4.14) carbon concentration at RT is assumed to be valid then the carbon concentrations for measured materials have (almost) acquired their homogeneous carbon distribution within the observed grains and the homogeneous carbon concentration is the minimum carbon concentration necessary to obtain stable austenite. With the exceptions of the C30 and C28 material where there is for the C30-QT217-50 material a carbon concentration in the retained austenite has a higher value than necessary for sable austenite [59]. Which indicate that the inhomogeneous carbon distribution in the C30-QT217-50 material will create a more stable austenite phase. For the C28 material the difference in Q&P heat treatments will influence the carbon concentration at RT. Where for the C28-

QT240 material the non-isothermal heat treatment will shorten time for carbon partitioning so that the carbon concentration is smaller than calculated. For the C28-QT280 the limited amount of austenite phase present in the material is due to the carbon concentration of the individual austenite grains prior to the quenching step.

4.6.2. The carbon concentration under stress

The carbon concentration in retained austenite can be measured as an increase of the unit cell lattice parameter of the phase, which is related to a shift of the intensity peaks on the Bragg angle. The carbon concentration in lattice parameter of the retained austenite is calculated with the following equation [49].

$$a = a_0 + 4{,}4 * 10^{-3}(mass\%)X_c\ [\text{Å}] \quad (4.12)$$

Where a_0 is the lattice parameter of unalloyed austenite unit cell with the fcc crystal structure and $4{,}4 * 10^{-3}(mass\%)C$ is the lattice parameter increase due to the presence of interstitial carbon in the lattice.
For the measurements of the carbon concentration at stress levels higher than 0 MPa the elastic stresses need to subtracted from the carbon concentration measurement. Due to the parallel beam X-ray diffraction measurement the lattice parameter (a) is decreasing (contraction) with increase stress. The contraction of a is a cross contraction which relate to the expansion of the tensile specimen via the Poisson's ratio (ν) which has a value of 0,3 [60]. The compression (contraction) strain can be obtained with the following equation.

$$\varepsilon = \frac{\Delta a}{a} = \frac{\nu\sigma}{E} \quad (4.13)$$

Where Δa is the lattice parameter reduction with each stress step, a is the initial lattice parameter at 0 MPa, ν is the Poisson's ratio, σ is the applied stress and E is the Young's modulus for the specific plane. The Young's modulus can have a large difference (anisotropy) in texture strengthening between different planes.

To obtain the Young's modulus for each plane a linear regression line (Appendix E) line is plotted along the measured lattice parameter values until the stress levels have reached the yield stress of the material. In table 4.12 the obtained Young's modulus for the fcc plane ($\{200\}_\gamma$ and $\{220\}_\gamma$) have a large deviation between the lowest and highest Young's modulus value. For the bcc planes ($\{200\}_{\alpha'}$ and $\{211\}_{\alpha'}$) the relation between the bcc plane has a small deviation see table 4.12.

Table 4.12: Young's modulus calculation

Sample material	$E_{\{200\}_\gamma}^{regression}\ [GPa]$	$E_{\{220\}_\gamma}^{regression}\ [GPa]$	$E_{\{200\}_{\alpha'}}^{regression}\ [GPa]$	$E_{\{211\}_{\alpha'}}^{regression}\ [GPa]$
Average C25	180	323	167	183
Average C30	283	284	163	192
Average C28	180	255	152	205

The average the $E_{\{220\}_\gamma}^{regression}$ values of the C25, C30 and C28 material: 323 GPa, 284 GPa and 255 GPa are used to obtain the carbon concentration under stress. The carbon concentration vs. the engineering stress divided by the yields stress can be seen in figure 4.11 until figure 4.17.

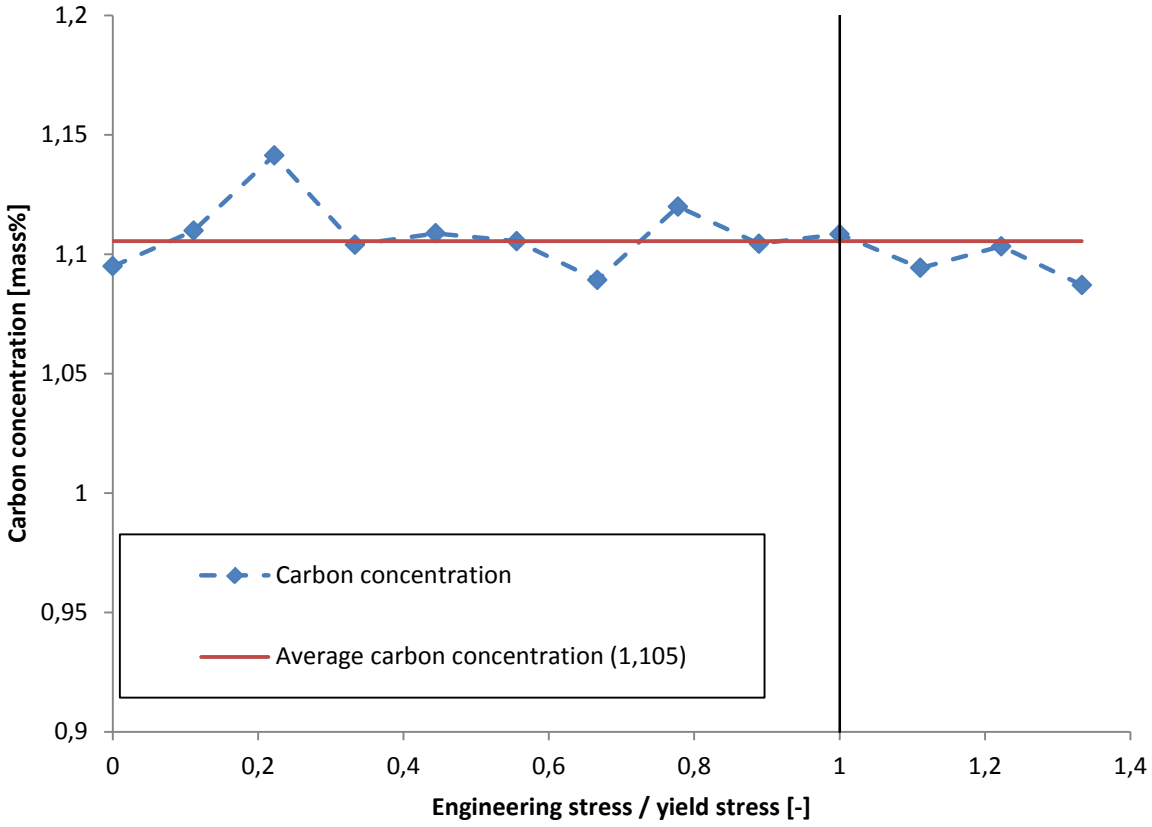

Figure 4.11: Carbon concentration vs. Engineering stress / yield stress of C25-QT244-50

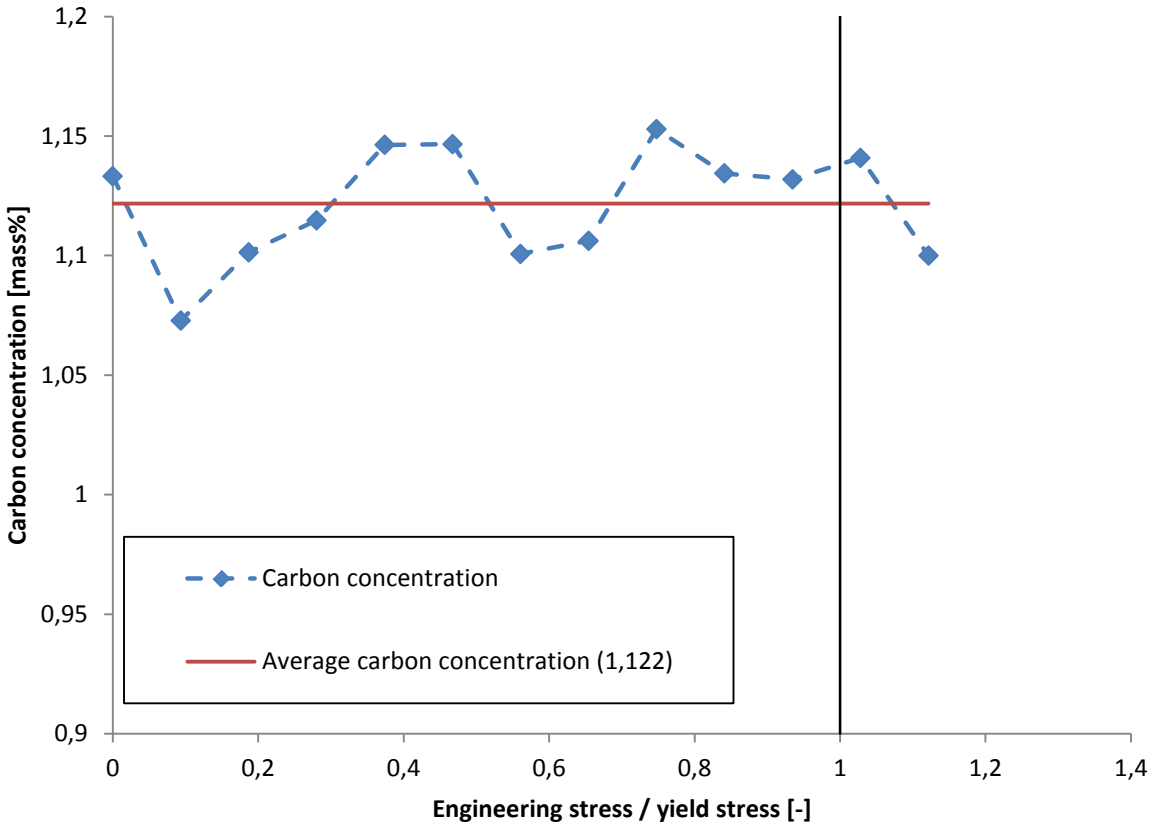

Figure 4.12: Carbon concentration vs. Engineering stress / yield stress of C25-QT224-50

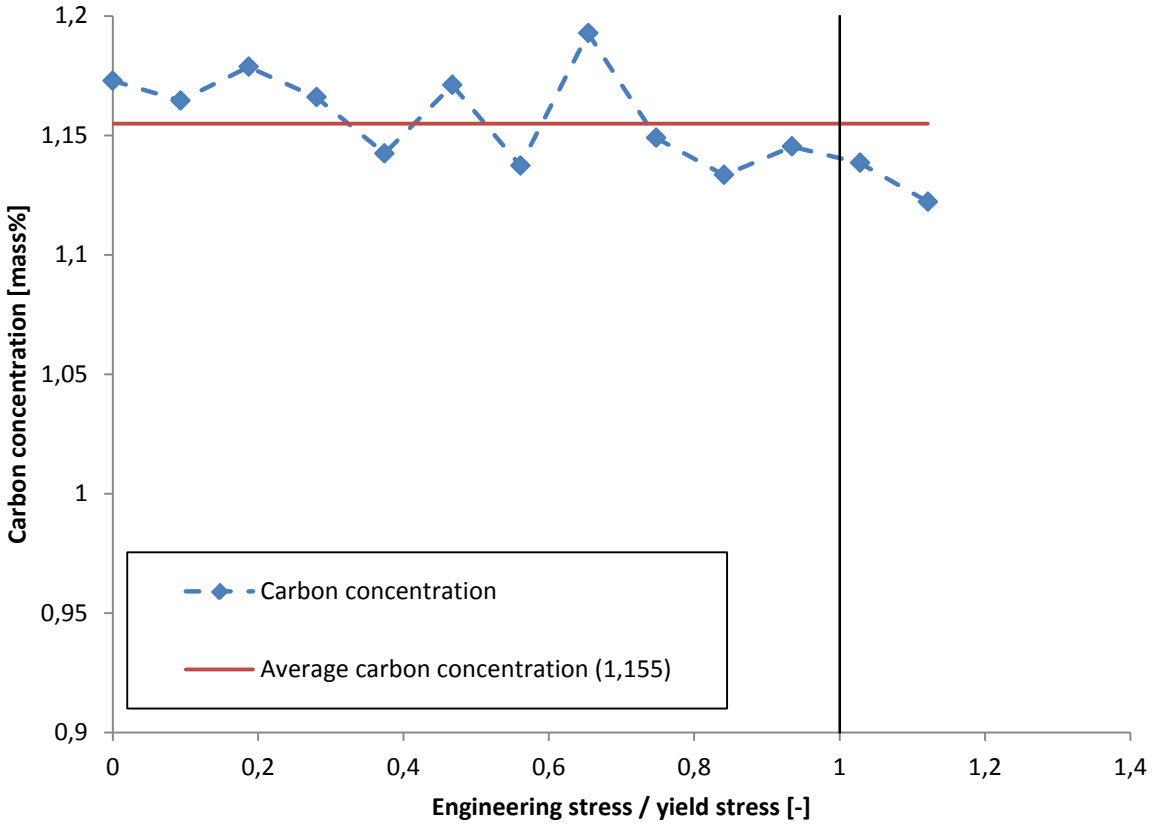

Figure 4.13: Carbon concentration vs. Engineering stress / yield stress of C25-QT244-25

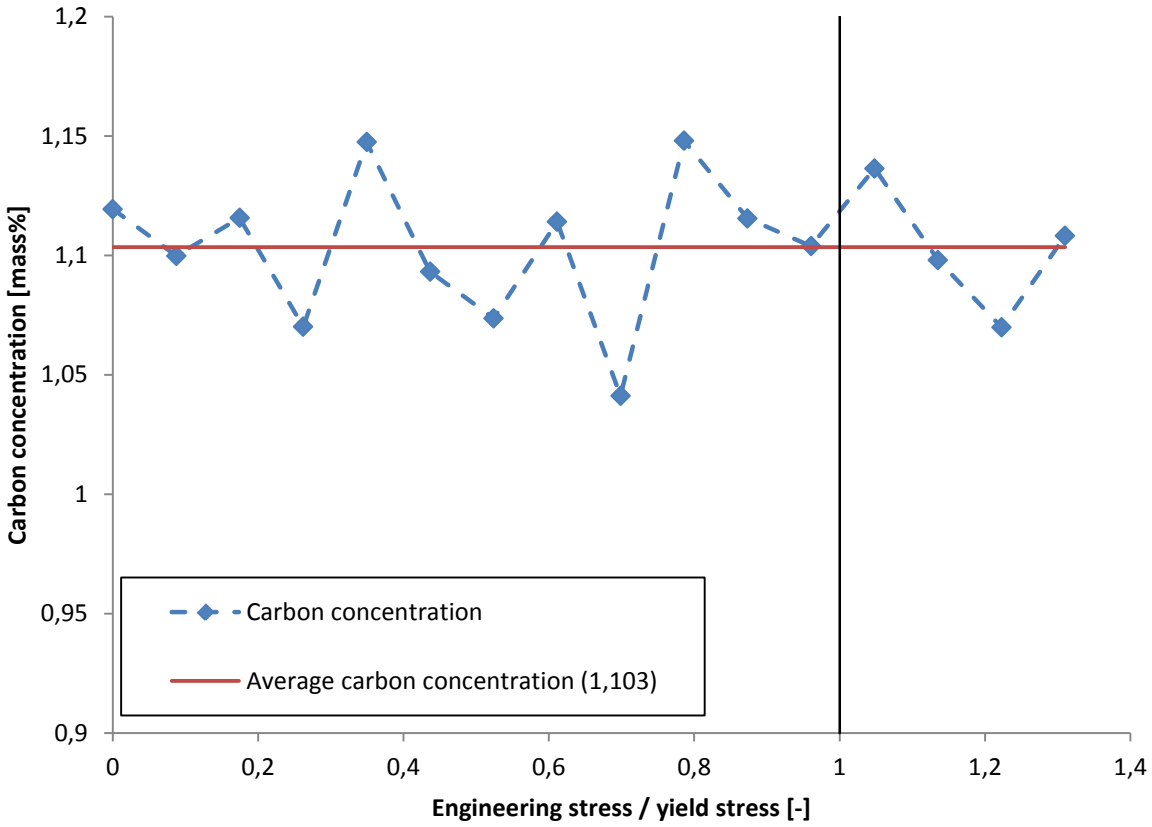

Figure 4.14: Carbon concentration vs. Engineering stress / yield stress of C30-QT237-50

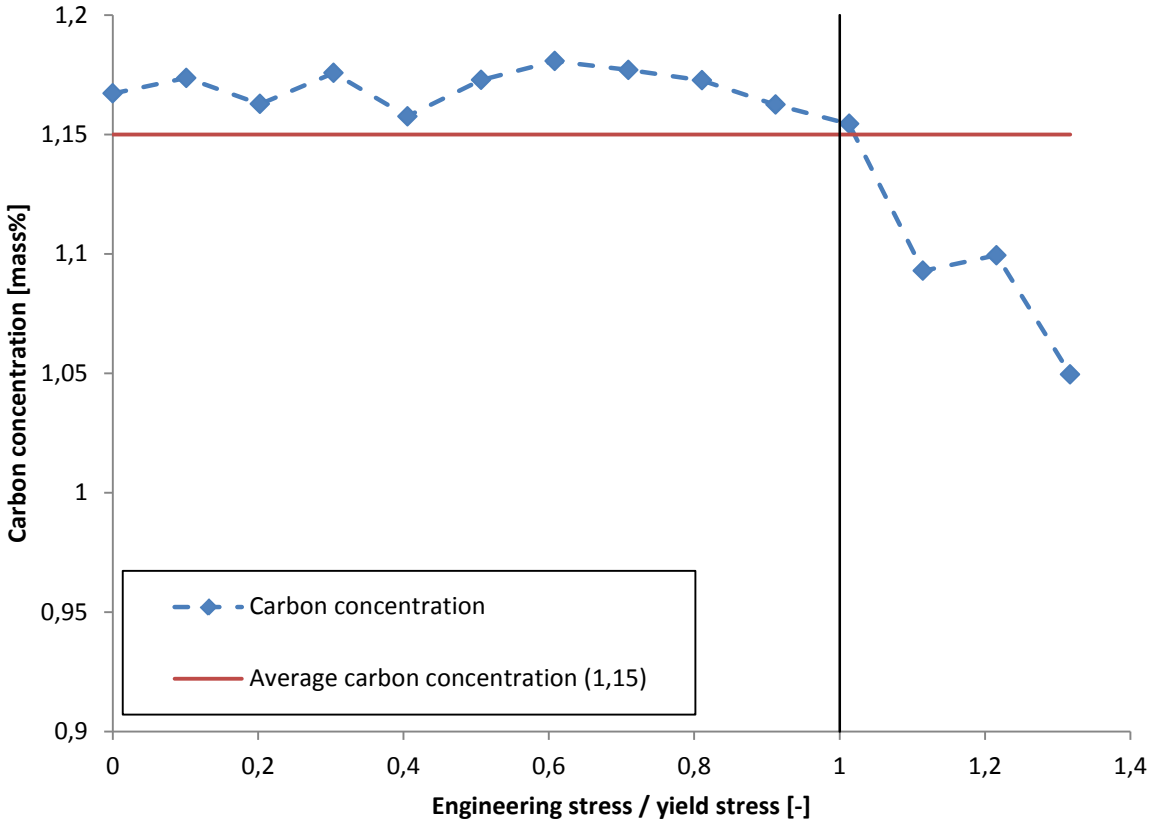

Figure 4.15: Carbon concentration vs. Engineering stress / yield stress of C30-QT217-50

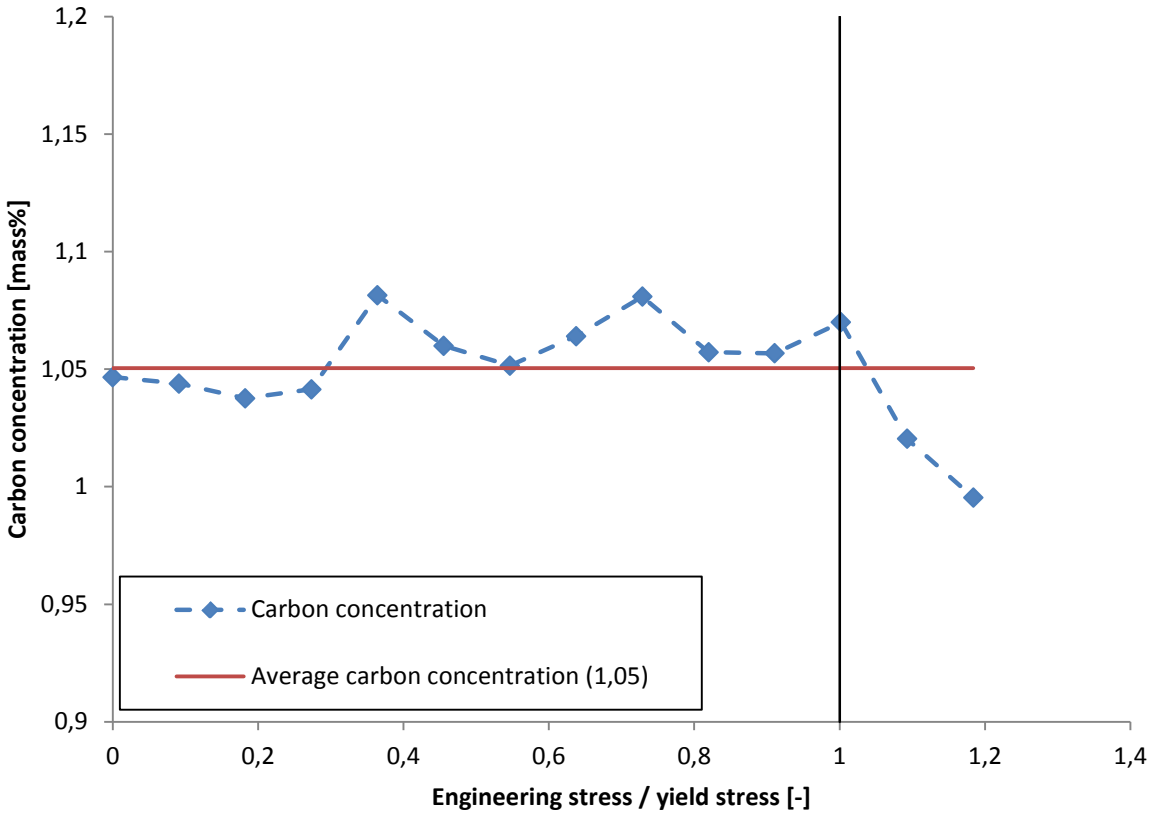

Figure 4.16: Carbon concentration vs. Engineering stress / yield stress of C28-QT240

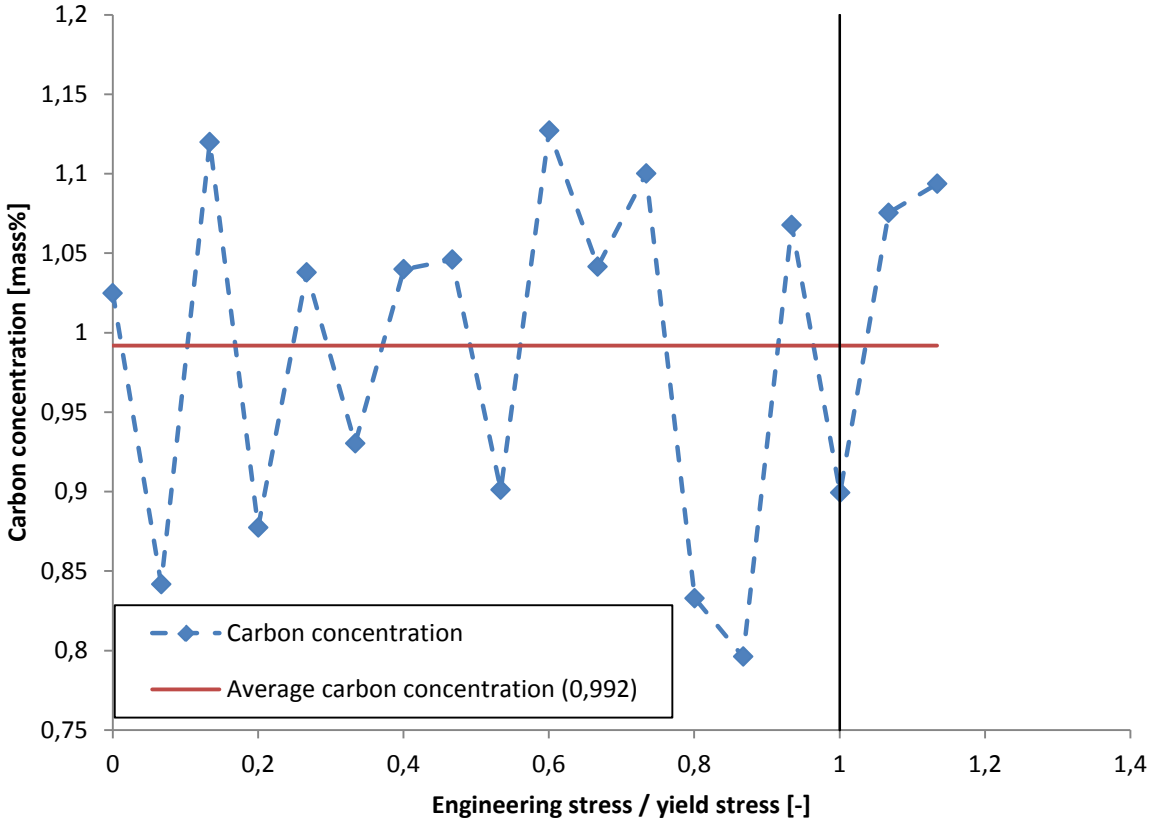

Figure 4.17: Carbon concentration vs. Engineering stress / yield stress of C28-QT280

The carbon concentration of the $\{220\}_\gamma$ austenite phase (figure 4.11 until figure 4.17) are scattered around the average carbon concentration value when an mechanical deformation is applied. For the C25 material there is little difference carbon concentration when mechanical deformation is applied.

For the C30 there is a difference between the two samples. For the C30-QT217-50 the carbon concentration is above the average value and will decrease around the yield stress of the material. Whereas for the C30-Q237-50 the carbon concentration is around the average value even beyond the yield stress of the material.

For the C28 material there is a difference between the two samples. Whereas for the C28-QT240 there is a carbon concentration value near the average values and it decrease around the yields stress of the material. For the C28-QT280 there is a large scatter due to the scatter of the lattice parameter (see Appendix E).

The graphs from figure 4.11 until figure 4.17 give an indication that within the Q&P material the retained austenite phase is stable until the yields stress and sometimes beyond the yield stress. If the retained austenite phase is not stable then a carbon concentration increase is expected. The carbon concentration increase is expected after the yield stress when more stable retained austenite with a higher carbon concentration has a phase transformation to the martensite phase. The idea behind the phase transformation is that retained austenite phase with a higher carbon concentration has a larger crystal lattice distortion and thus chemical driving force (ΔG^{ch}) which must be overcome to have phase transformation [22, 44].

In this case the carbon concentration is stable at larger stress values than the yields stress or the carbon concentration has a decrease. The decrease in carbon concentration after the yield stress is only noticeable with the C30-QT237-50 and the C28-QT240 material. In comparison of C30-QT237-50 with the C30-QT217-50 and the C28-QT240 with C28-QT280 then both of these samples have a high strain at fracture (A_t) value (see figure 4.2). The decrease in carbon concentration at stress values larger than the yields stress of the material can be explained when the measured retained austenite phase has thus low values that the measurement of the carbon concentration (by means of the lattice parameter) in the retained austenite phase is not accurate enough.

4.7. Comparison between the C25, C30 and C28 material

In the C25 material the heat treatment has an influence on the yield-, ultimate tensile strength and on the strain of the material. Decreasing of the partitioning time (Pt) will increase the total strain of the material and increase the yield stress. Whereas decreasing the quenching temperature (QT), the initial retained austenite volume fraction will also decrease (see figure 4.2 and figure 4.4). Remark for the obtained mechanical properties of Young's modulus and UTS, high strain at fracture (A_t) for the C25-QT244-50 tensile sample which can be not representative due to low Young's modulus (see figure 4.2).

In the C30 material the heat treatment has an influence on the yield-, ultimate tensile strength and on the strain of the material. When the quenching temperature (QT) is decreased the yield- and ultimate tensile strength decreases while the strain increases. Also when the quenching temperature (QT) is decreased the retained austenite volume fraction increases which is also more stable due to the slight increasing strain hardening with increasing strain. This can be related to the initial carbon concentration in the C30-QT217-50 material has not reached its equilibrium distribution. So that the inhomogeneity of carbon contribution increases the total strain [44] (see figure 4.2 and figure 4.4).

The C28 material has different mechanical properties due to the heat treatment applied to the samples. The yield-, ultimate tensile strength and the strain are different for both of the C28 material. The retained austenite volume fraction is significantly lower for the C28-QT280 material than for the C28-QT240. The carbon concentration in the retained austenite has little difference between the two C28 material. The mechanical stability of the C28-QT280 has the lowest value of all the tested material, so that high yield-, and ultimate tensile strength is a trade off in relation with the mechanical stability (strain) (see figure 4.2 and figure 4.4).

4.8.The TRIP-effect

The TRIP-effect where there is a phase transformation from the retained austenite phase to the martensite phase under the influence of the applied mechanical deformation can been seen in the three materials. The phase transformation is observed in the range of the yield stress. A distinction between the phase transformation occurs below or above the yield stress this cannot be observed. This can be related to the applied stress steps of 100 MPa which are too large to indicate the difference. The retained austenite volume fraction present in the material is controlling the mechanical properties as can be seen in C28 material. The (inhomogeneous) carbon concentration present in retained austenite phase of the Q&P material is controlling the strain parameter of the mechanical properties as can be seen in C30 material.

5. Conclusion and recommendations

5.1. Conclusions

- The retained austenite is controlling the mechanical of the Q&P steel through the retained austenite volume fraction and (inhomogeneous) carbon concentration present in the retained austenite.
- The TRIP-effect is playing a role of altering the mechanical (strain) properties of the Q&P steel.
- The measurement of the TRIP-effect with (large) stress steps provides less information in the plastic regime of the stress-strain curve.
- Almost all of the material has a preferred orientation (texture) so that the calculated retained austenite volume fraction is depended on the crystal lattice planes.
- For the OCAS Q&P material (C25 & C30) the decrease in retained austenite volume fraction starts at stress levels higher than the yield stress of the Q&P material. For the C25 material the stability of the retained austenite is dependent on the heat treatment applied to the material. Where a decrease of partitioning time (Pt) or quenching temperature (QT) will decrease the initial retained austenite which influence the yield strength and the total strain. For the C30 material the stability of the retained austenite is depended on the heat treatment applied to the material. A decrease in temperature (QT) will decrease the yield strength and ultimate tensile strength but increase the total strain.
- For the Thyssenkrupp Q&P material (C28) the non 'standard' Q&P heat treatment properties can have an influence on the initial retained austenite volume fraction and the decrease of the retained austenite volume fraction when mechanical deformation is applied. For the C28-QT240 Q&P material there is a decrease of the retained austenite volume fraction when the mechanical deformation has reached the yield stress of the Q&P material. For the C28-QT280 Q&P material the difference between the initial and the final retained austenite volume fraction is little so that the determination if there is a TRIP-effect is not clear.

5.2. Recommendations

- To acquire more information in the plastic regime of the stress-strain curve the In situ X-ray diffraction experiment needs to be conducted in strain steps or smaller stress steps.
- The Q&P material is measured in the transverse direction (TD) this can have an influence on the mechanical properties so that the measurement can be conducted in the Rolling direction (RD).
- To acquire a more direct measurement of the strain applied to the tensile specimen a digital imagine correlation (DIC) can be used.

Reference

[1] WorldAutoSteel, *FutureSteelVehicle, Phase 2*, WorldAutoSteel, 2011.

[2] K.W. Andrews, *Empirical Formulae for the Calculation of Some Transformation Temperatures* Journal of the Iron and Steel Institute, 203 (1965) 721-727.

[3] S.M.C. Van Bohemen, *Bainite and martensite start temperature calculated with exponential carbon dependence* Materials Science and Technology, 28 (2012) 487-495.

[4] E. Jimenez-Melero, N.H. van Dijk, L. Zhao, J. Sietsma, S.E. Offerman, J.P. Wright, S. van der Zwaag, *Martensitic transformation of individual grains in low-alloyed TRIP steels* Scripta Materialia, 56 (2007) 421-424.

[5] H.S. Yang, H.K.D.H. Bhadeshia, *Austenite grain size and the martensite-start temperature* Scripta Materialia, 60 (2009) 493-495.

[6] S.J. Lee, K.S. Park, *Prediction of Martensite Start Temperature in Alloy Steels with Different Grain Sizes* Metallurgical and Materials Transactions a-Physical Metallurgy and Materials Science, 44A (2013) 3423-3427.

[7] D.P. Koistinen, R.E. Marburger, *A General Equation Prescribing the Extent of the Austenite-Martensite Transformation in Pure Iron-Carbon Alloys and Plain Carbon Steels* Acta Metallurgica, 7 (1959) 59-60.

[8] J. Speer, D.K. Matlock, B.C. De Cooman, J.G. Schroth, *Carbon partitioning into austenite after martensite transformation* Acta Materialia, 51 (2003) 2611-2622.

[9] N. Zhong, X. Wang, Y. Rong, L. Wang, *Interface migration between martensite and austenite during quenching and partitioning (Q&P) process* Journal of Materials Science and Technology, 22 (2006) 751-754.

[10] M.J. Santofimia, L. Zhao, J. Sietsma, *Model for the interaction between interface migration and carbon diffusion during annealing of martensite-austenite microstructures in steels* Scripta Materialia, 59 (2008) 159-162.

[11] M. De Meyer, D. Vanderschueren, B.C. De Coomaim, *The influence of the substitution of Si by AI on the properties of cold rolled C-Mn-Si TRIP steels* ISIJ Int, 39 (1999) 813-822.

[12] Y. Takahama, M.J. Santofimia, M.G. Mecozzi, L. Zhao, J. Sietsma, *Phase field simulation of the carbon redistribution during the quenching and partitioning process in a low-carbon steel* Acta Materialia, 60 (2012) 2916-2926.

[13] J.H. Ryu, D.I. Kim, H.S. Kim, H.K.D.H. Bhadeshia, D.W. Suh, *Strain partitioning and mechanical stability of retained austenite* Scripta Materialia, 63 (2010) 297-299.

[14] P.J. Jacques, J. Ladrière, F. Delannay, *On the influence of interactions between phases on the mechanical stability of retained austenite in transformation-induced plasticity multiphase steels* Metall Mat Trans A Phys Metall Mat Sci, 32 (2001) 2759-2768.

[15] P.J. Gibbs, E. De Moor, M.J. Merwin, B. Clausen, J.G. Speer, D.K. Matlock, *Austenite stability effects on tensile behavior of manganese-enriched-austenite transformation-induced plasticity steel* Metall Mat Trans A Phys Metall Mat Sci, 42 (2011) 3691-3702.

[16] I.B. Timokhina, P.D. Hodgson, E.V. Pereloma, *Effect of deformation schedule on the microstructure and mechanical properties of a thermomechanically processed C-Mn-Si transformation-induced plasticity steel* Metallurgical and Materials Transactions a-Physical Metallurgy and Materials Science, 34A (2003) 1599-1609.

[17] E. de Moor, S. Lacroix, A.J. Clarke, J. Penning, J.G. Speer, *Effect of retained austenite stabilized via quench and partitioning on the strain hardening of martensitic steels* Metall Mat Trans A Phys Metall Mat Sci, 39 (2008) 2586-2595.
[18] O. Muransky, P. Hornak, P. Lukas, J. Zrnik, P. Sittner, *Investigation of retained austenite stability in Mn-Si TRIP steel in tensile deformation condition* Journal of Achievements in Materials and Manufacturing Engineering, 14 (2006) 26-30.
[19] X.D. Wang, B.X. Huang, Y.H. Rong, L. Wang, *Microstructures and stability of retained austenite in TRIP steels* Materials Science and Engineering: A, 438–440 (2006) 300-305.
[20] J.H. Ryu, D.-I. Kim, H.S. Kim, H.K.D.H. Bhadeshia, D.-W. Suh, *Strain partitioning and mechanical stability of retained austenite* Scripta Materialia, 63 (2010) 297-299.
[21] S.O. Kruijver, L. Zhao, J. Sietsma, E.M. Lauridsen, H.F. Poulsen, S.E. Offerman, N.H. Dijk, van,, L. Margulies, S. Grigull, S. Zwaag, van der; , *The mechanical stability of austenite in TRIP steel observed by 3D X-ray microdiffraction*, 2003.
[22] S. Van Der Zwaag, L. Zhao, S.O. Kruijver, J. Sietsma, *Thermal and mechanical stability of retained austenite in aluminum-containing multiphase TRIP steels* ISIJ Int, 42 (2002) 1565-1570.
[23] S.O. Kruijver, L. Zhao, J. Sietsma, E. Offerman, N. van Dijk, L. Margulies, E. Lauridsen, S. Grigull, H. Poulsen, S. van der Zwaag, *In situ observations on the austenite stability in TRIP-steel during tensile testing* Steel Research, 73 (2002) 236-241.
[24] J. Mola, B.C. De Cooman, *Quenching and partitioning (Q&P) processing of martensitic stainless steels* Metall Mat Trans A Phys Metall Mat Sci, 44 (2013) 946-967.
[25] L. Wang, J. Speer, *Quenching and Partitioning Steel Heat Treatment* Metallogr. Microstruct. Anal., 2 (2013) 268-281.
[26] X.C. Xiong, B. Chen, M.X. Huang, J.F. Wang, L. Wang, *The effect of morphology on the stability of retained austenite in a quenched and partitioned steel* Scripta Materialia, 68 (2013) 321-324.
[27] C. Garcia-Mateo, F.G. Caballero, J. Chao, C. Capdevila, C. Garcia De Andres, *Mechanical stability of retained austenite during plastic deformation of super high strength carbide free bainitic steels* J Mater Sci, 44 (2009) 4617-4624.
[28] H.L. Yi, K.Y. Lee, H.K.D.H. Bhadeshia, *Mechanical stabilisation of retained austenite in δ-TRIP steel* Materials Science and Engineering A, 528 (2011) 5900-5903.
[29] J.R.C. Guimarães, P.R. Rios, *Microstructural analysis of the martensite volume fraction* Metall Mat Trans A Phys Metall Mat Sci, 44 (2013) 147-151.
[30] A. Dimatteo, G. Lovicu, M. Desanctis, R. Valentini, A. Solina, *Microstructures and properties of Transformation Induced Plasticity steels* Metallurgia Italiana, 98 (2006) 37-41.
[31] A.D. Talapatra, J.; Bandhyopadhyay N.R., *Structure-Properties Relationship of TRIP-assisted Steels by Non-destructive Testing Method* Chemical and Materials Engineering, 1 (2013) 10.
[32] Q. Furnémont, M. Kempf, P.J. Jacques, M. Göken, F. Delannay, *On the measurement of the nanohardness of the constitutive phases of TRIP-assisted multiphase steels* Materials Science and Engineering A, 328 (2002) 26-32.

[33] S. Lee, S.J. Lee, B.C. De Cooman, *Austenite stability of ultrafine-grained transformation-induced plasticity steel with Mn partitioning* Scripta Materialia, 65 (2011) 225-228.
[34] K. Ren, Y. Kang, S. Zhu, *Effect of partitioning time on the microstructure and mechanicalproperties of Q&P steels*, 749 2013, pp. 303-307.
[35] C.Y. Wang, J. Shi, W.Q. Cao, H. Dong, *Characterization of microstructure obtained by quenching and partitioning process in low alloy martensitic steel* Materials Science and Engineering a-Structural Materials Properties Microstructure and Processing, 527 (2010) 3442-3449.
[36] M.J. Santofimia, L. Zhao, J. Sietsma, *Overview of Mechanisms Involved During the Quenching and Partitioning Process in Steels* Metallurgical and Materials Transactions a-Physical Metallurgy and Materials Science, 42A (2011) 3620-3626.
[37] C. Wang, Y. Zhang, W. Cao, J. Shi, M. Wang, H. Dong, *Austenite/martensite structure and corresponding ultrahigh strength and high ductility of steels processed by Q&P techniques* Science China Technological Sciences, 55 (2012) 1844-1851.
[38] G.B. Olson, M. Cohen, *A mechanism for the strain-induced nucleation of martensitic transformations* Journal of The Less-Common Metals, 28 (1972) 107-118.
[39] D.E. Laughlin, N.J. Jones, A.J. Schwartz, T.B. Massalski, *Thermally activated martensite: Its relationship to non-thermally activated (athermal) martensite*, 2009, pp. 141-144.
[40] S. Curtze, V.T. Kuokkala, M. Hokka, P. Peura, *Deformation behavior of TRIP and DP steels in tension at different temperatures over a wide range of strain rates* Materials Science and Engineering A, 507 (2009) 124-131.
[41] S. Chatterjee, H.K.D.H. Bhadeshia, *Transformation induced plasticity assisted steels: stress or strain affected martensitic transformation?* Materials Science and Technology, 23 (2007) 1101-1104.
[42] M.Y. Zhang, F.X. Zhu, D.S. Zheng, *Mechanical Properties and Retained Austenite Transformation Mechanism of TRIP-Aided Polygonal Ferrite Matrix Seamless Steel Tube* Journal of Iron and Steel Research International, 18 (2011) 73-78.
[43] D.a.K. Brandon, W. D., Microstructural Characterization of Materials, 2nd ed., J. Wiley & Sons, Ltd, West Sussex, England, 2008.
[44] L. Zhao, N.M. Van Der Pers, J. Sietsma, S. Van Der Zwaag, *In situ X-ray diffraction measurements of deformation-induced austenite to martensite transformation in a multiphase TRIP steel*, 500-501 2005, pp. 379-386.
[45] A. Itami, M. Takahashi, K. Ushioda, *Plastic stability of retained austenite in the cold-rolled 0.14%C-1.9%Si-1.7%Mn sheet steel* ISIJ Int, 35 (1995) 1121-1127.
[46] X. Wei, M. Hua, Z. Xue, Z. Gao, J. Li, *Evolution of friction-induced microstructure of SUS 304 meta-stable austenitic stainless steel and its influence on wear behavior* Wear, 267 (2009) 1386-1392.
[47] F. Hajy Akbary, M.J. Santofimia, J. Sietsma, *Elastic Strain Measurement of Miniature Tensile Specimens* Experimental Mechanics, (2013) 1-9.
[48] J.R. Davis, Tensile Testing Second Edition, ASM International, 2004.
[49] C.F. Jatczak, *Retained austenite and its measurement by X-ray diffraction* SAE Technical Papers, (1980).
[50] M.J. Dickson, *The significance of texture parameters in phase analysis by X-ray diffraction* Journal of Applied Crystallography, 2 (1969) 176-180.

[51] C.J. Ball, P.M. Kelly, *X-RAY METHOD FOR DETERMINATION OF RETAINED AUSTENITE IN STEELS WITH PRONOUNCED TEXTURE*, 16 1982, pp. 332-334.
[52] E.-i. Furubayashi, H. Miyaji, M. Nobuki, *SIMPLE MODEL OF PREDICTING THE TRANSFORMATION TEXTURES IN THERMOMECHANICALLY PROCESSED STEELS* Transactions of the Iron and Steel Institute of Japan, 27 (1987) 513-519.
[53] R.K. Ray, J.J. Jonas, *Transformation textures in steels* International Materials Reviews, 35 (1990) 1-36.
[54] R. Delhez, *The volume fraction Austenite, in a two-phase steel from X-ray diffration (XRD) measurements and the standard deviation causted by the counting statistical errors*, TU Delft, 2012, pp. 7.
[55] P. Hilkhuijsen, H.J.M. Geijselaers, T.C. Bor, *The influence of austenite texture on the martensitic transformation of an austenitic stainless steel* Journal of Alloys and Compounds, 577, Supplement 1 (2013) S609-S613.
[56] D. Ludwigson, J.A. Berger, *Plastic behaviour of metastable austenitic stainless steels* J Iron Steel Inst, 207 (1969) 63-69.
[57] J.R. Patel, M. Cohen, *Criterion for the action of applied stress in the martensitic transformation* Acta Metallurgica, 1 (1953) 531-538.
[58] G.N. Haidemenopoulos, A.N. Vasilakos, *On the thermodynamic stability of retained austenite in 4340 steel* Journal of Alloys and Compounds, 247 (1997) 128-133.
[59] M.J. Santofimia, L. Zhao, R. Petrov, C. Kwakernaak, W.G. Sloof, J. Sietsma, *Microstructural development during the quenching and partitioning process in a newly designed low-carbon steel* Acta Materialia, 59 (2011) 6059-6068.
[60] H.A. Hoff, G.L. Waytena, J.W. Glesener, V.G. Harris, D.P. Pappas, *Critical thickness of single crystal fcc iron on diamond* Surface Science, 326 (1995) 252-266.

Appendix A. Tensile specimen drawing

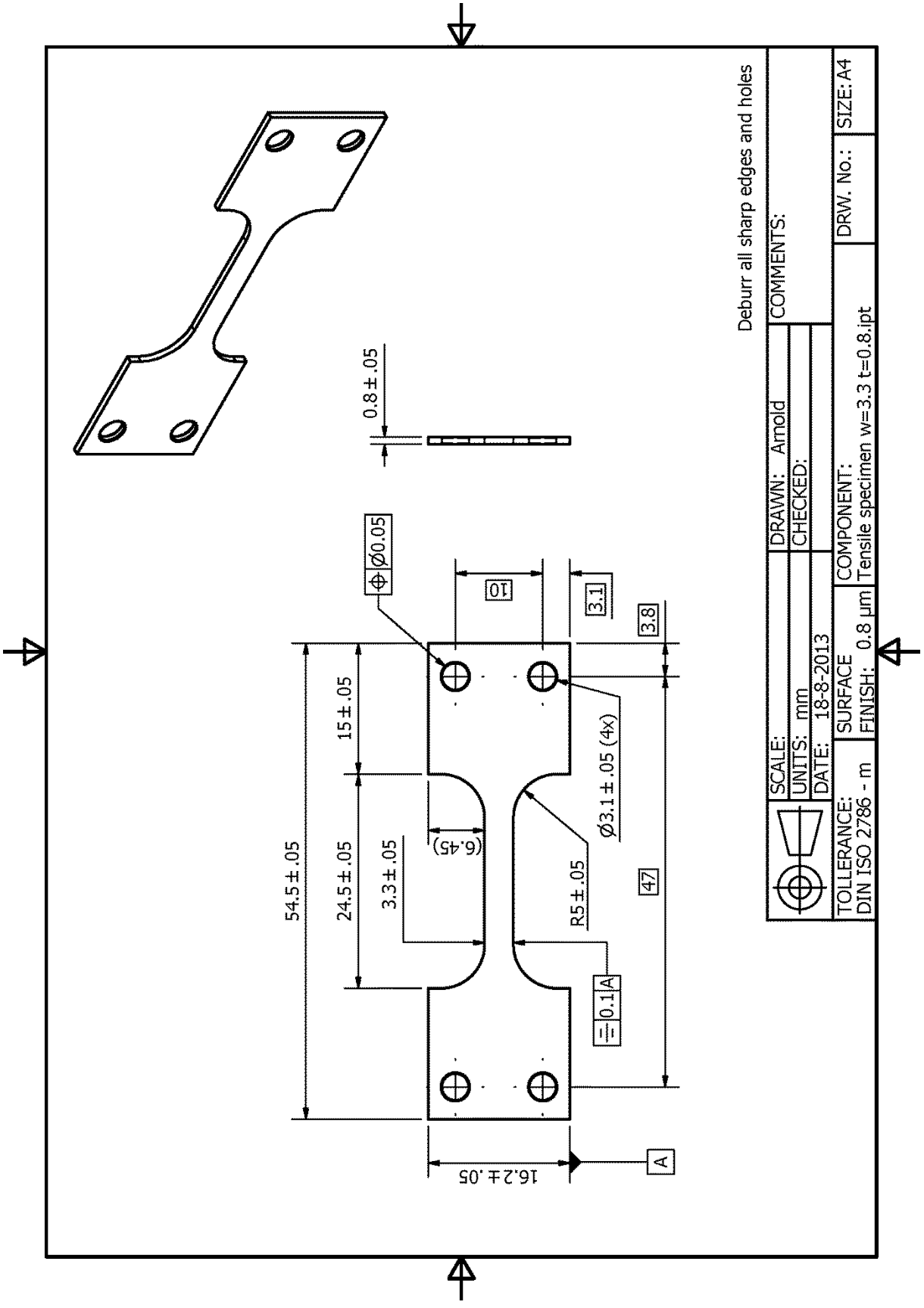

Appendix B. Counting Statistical Error

The Counting Statistical Errors(CSE)[54] are a applied statistic method to analysis the counting errors of X-ray diffraction. The counting in X-ray diffraction are the number of counts per second(cps) at a certain Bragg 2θ angle also called the Intensity(I) of diffraction. The Counting Statistical Errors(CSE) are in relation with the retained austenite volume fraction.

First the standard deviation of the Intensities of retained austenite and martensite needs to be calculated with the following equation.

$$\sigma_{\gamma}^2 = \frac{\sum_{i=1}^{n}\left(I_{\gamma,hkl}-\mu\right)^2}{n} \text{ and } \sigma_{\alpha'}^2 = \frac{\sum_{i=1}^{n}\left(I_{\alpha',hkl}-\mu\right)^2}{n} \qquad \text{(A.1 and A.2)}$$

Where $I_{\gamma,hkl}$ and $I_{\alpha',hkl}$ is the Intensity of the retained austenite or martensite at a certain hkl plane, μ is the mathematic average of the population and n is the number of counts of the population.

Then the concentration of the measured intensity(I) and the calculated intensity(R) need to calculated.

$$I_{R,\gamma} = \frac{I_{\gamma,hkl}}{R_{\gamma,hkl}} \text{ and } I_{R,\alpha'} = \frac{I_{\alpha',hkl}}{R_{\alpha',hkl}} \qquad \text{(A.3 and A.4)}$$

Where $I_{\gamma,hkl}$ and $I_{\alpha',hkl}$ are the measured intensities of retained austenite or martensite with specific hkl and $R_{\gamma,hkl}$ and $R_{\alpha',hkl}$ are the retained austenite or martensite calculated intensities with specific hkl plane.

After that the standard deviation of the Instensity standard deviation of retained austenite and martensite is calculated.

$$\sigma^2\left(I_{R,\gamma}\right) = \frac{\sigma_{\gamma}^2}{R_{\gamma,hkl}{}^2} \text{ and } \sigma^2\left(I_{R,\alpha'}\right) = \frac{\sigma_{\gamma}^2}{R_{\alpha',hkl}{}^2} \qquad \text{(A.5 and A.6)}$$

The last equation is used to calculate the CSE in relation with the retained austenite volume fraction.

$$\sigma_{CSE}(f^{\gamma}) = f^{\gamma} * (1 - f^{\gamma}) * \sqrt{\frac{\sigma^2\left(I_{R,\gamma}\right)}{I_{R,\gamma}{}^2} + \frac{\sigma^2\left(I_{R,\alpha'}\right)}{I_{R,\alpha'}{}^2}} \qquad \text{(A.7)}$$

Appendix C. R-value

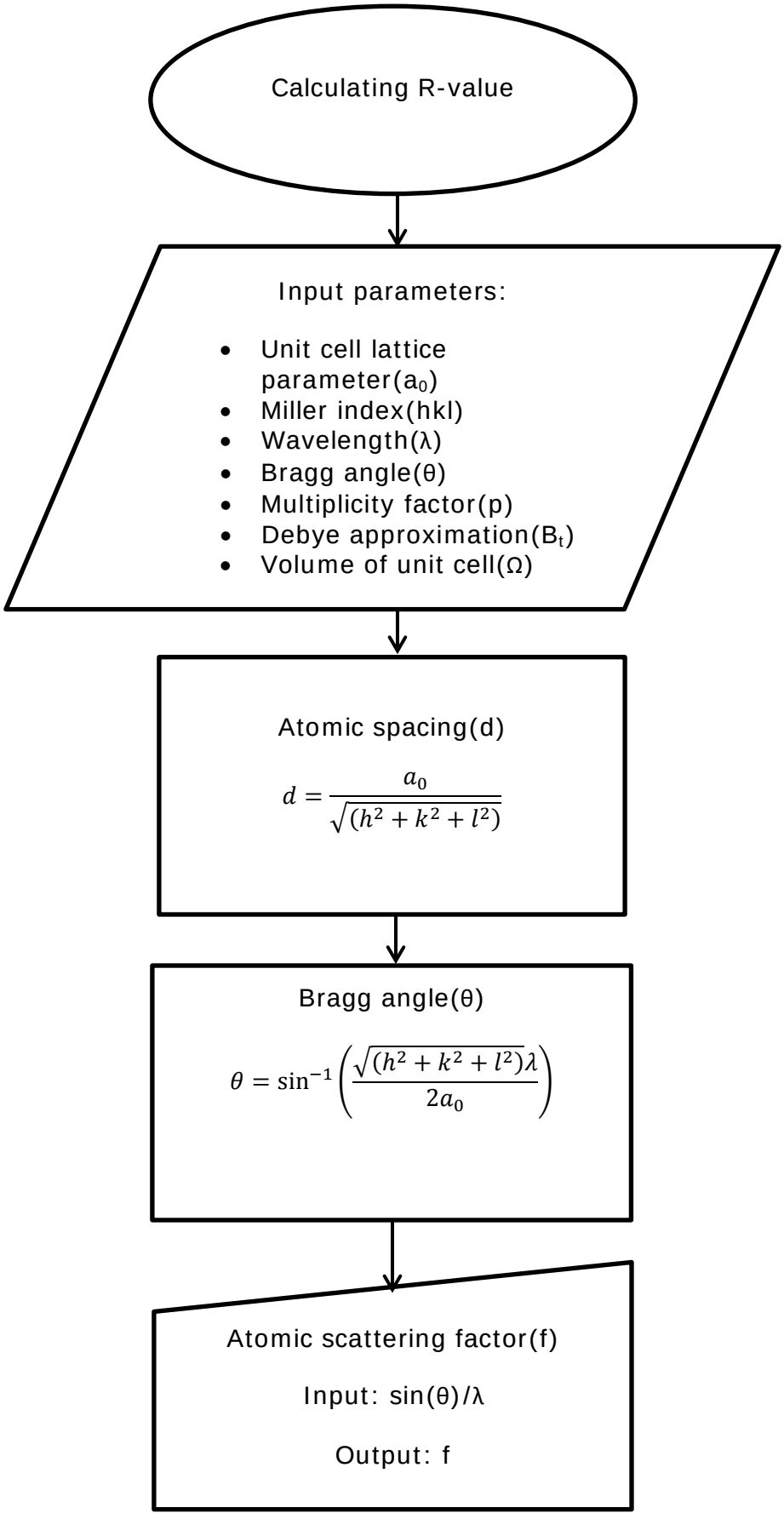

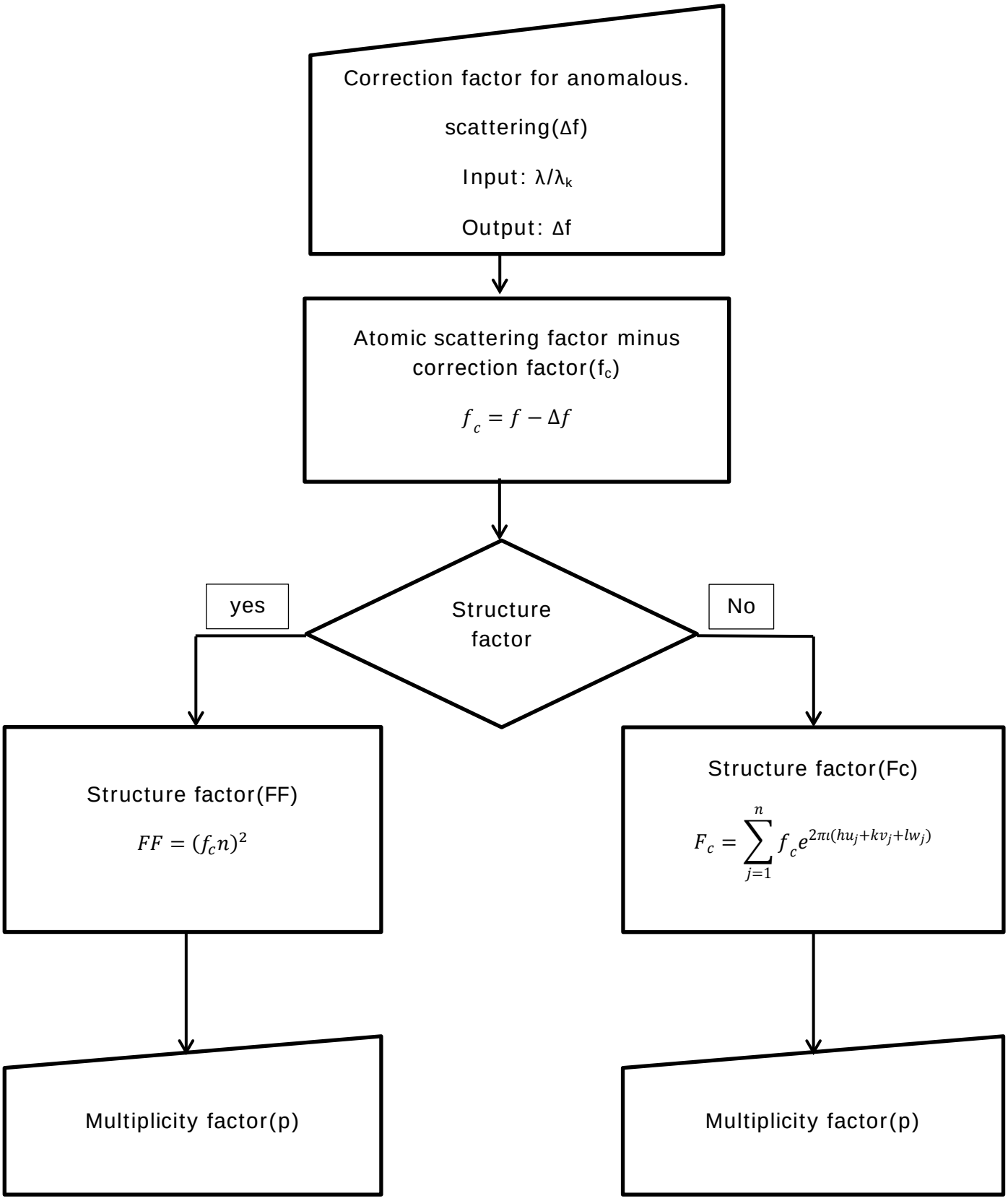
Correction factor for anomalous.
scattering(Δf)
Input: λ/λk
Output: Δf
Atomic scattering factor minus correction factor(fc)
$f_c = f - \Delta f$
Structure factor
yes
No
Structure factor(FF)
$FF = (f_c n)^2$
Structure factor(Fc)
$F_c = \sum_{j=1}^{n} f_c e^{2\pi\iota(hu_j+kv_j+lw_j)}$
Multiplicity factor(p)
Multiplicity factor(p)

Lorentz - polarization factor(Lp)

$$Lp = \frac{1 + \cos^2 2\theta}{\sin^2 \theta \cos \theta}$$

↓

Debye–Waller factor(e^{2Mt})

$$M_t = B_t \left(\frac{\sin \theta}{\lambda}\right)^2$$

↓

R-value

$$R = [FF^2 pLp] \frac{e^{-2M_T}}{\Omega^2}$$

Lorentz - polarization factor(Lp)

$$Lp = \frac{1 + \cos^2 2\theta}{2 \sin^2 \theta \cos \theta}$$

↓

Debye–Waller factor(e^{2Mt})

$$M_t = B_t \left(\frac{\sin \theta}{\lambda}\right)^2$$

↓

R-value

$$R = [|F_c|^2 pLp] \frac{e^{-2M_T}}{\Omega^2}$$

Appendix D. Texture parameter

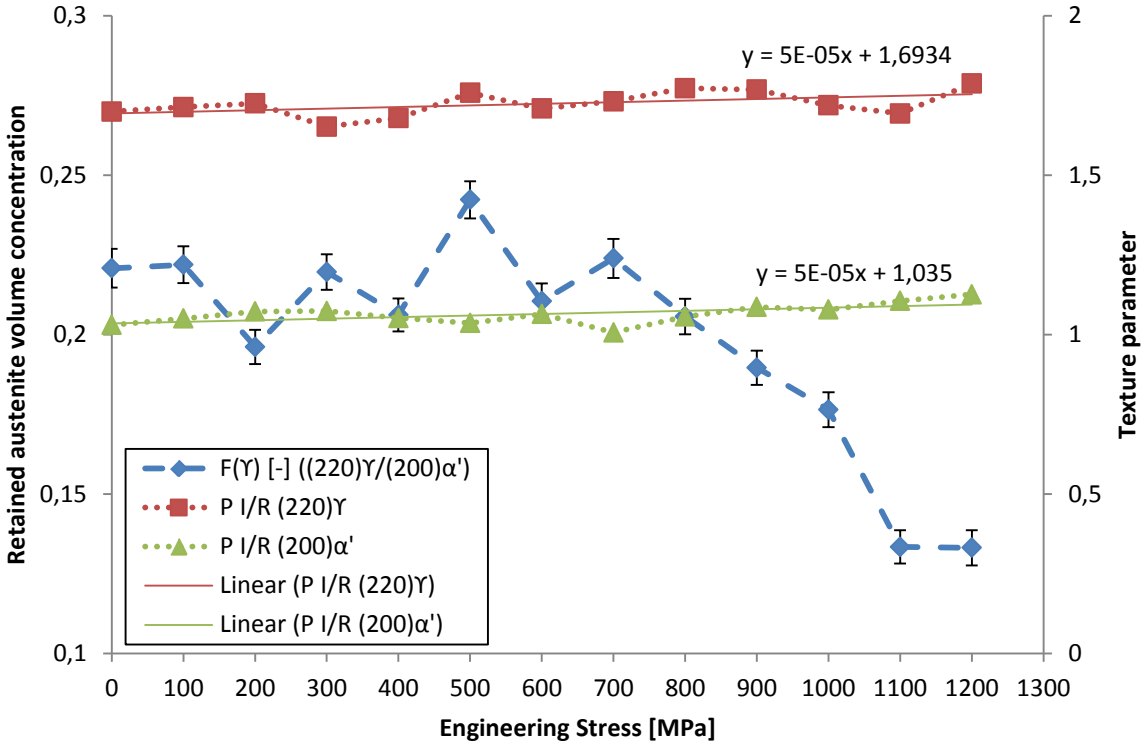

Figure D.1: RA volume fraction vs. texture parameter of C25-QT244-50

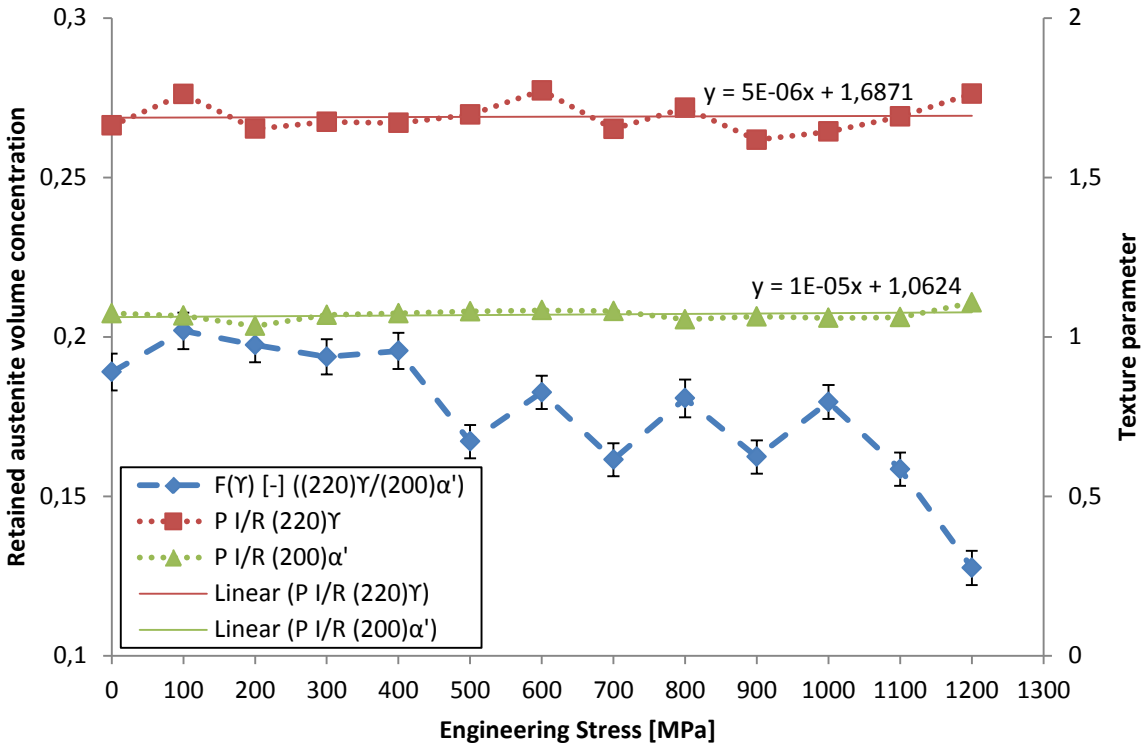

Figure D.2: RA volume fraction vs. texture parameter of C25-QT224-50

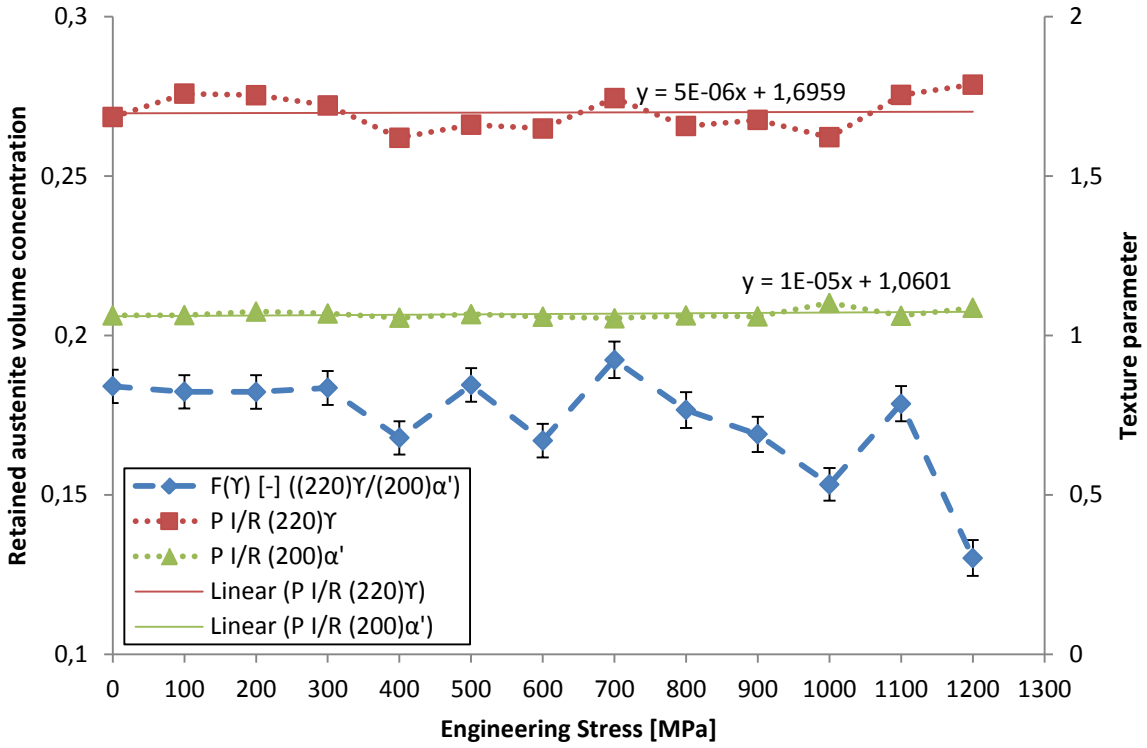

Figure D.3: RA volume fraction vs. texture parameter of C25-QT244-25

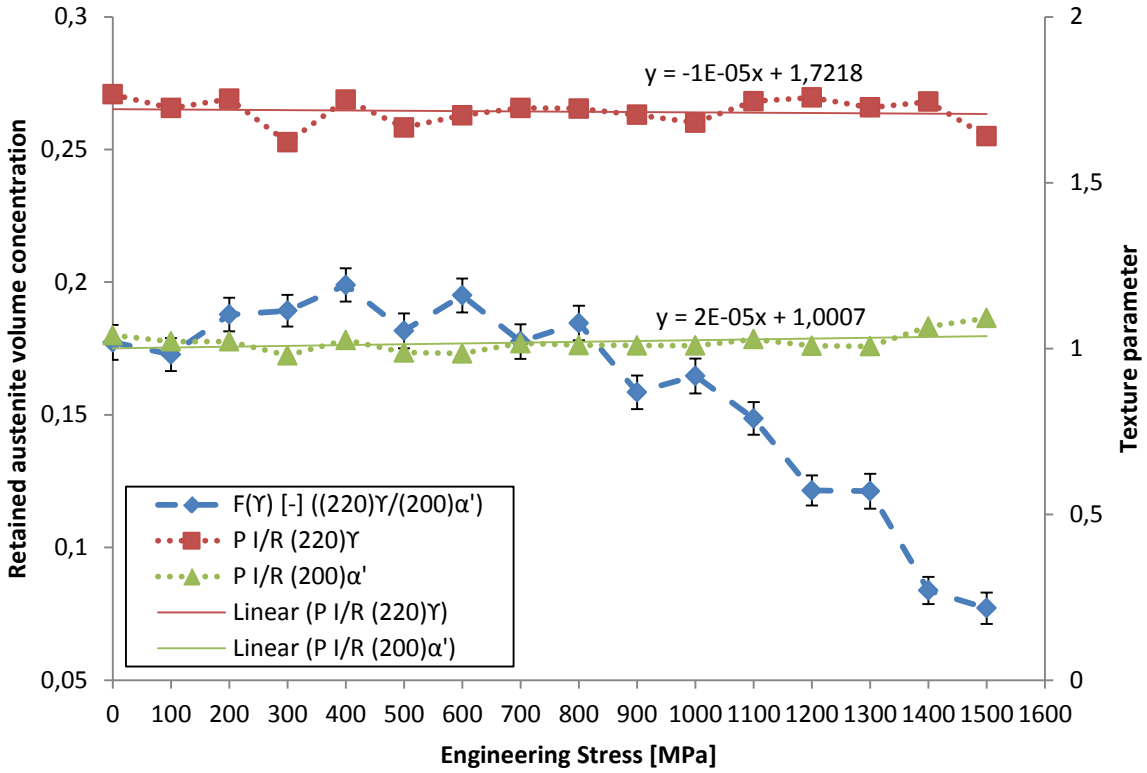

Figure D.4: RA volume fraction vs. texture parameter of C30-QT237-50

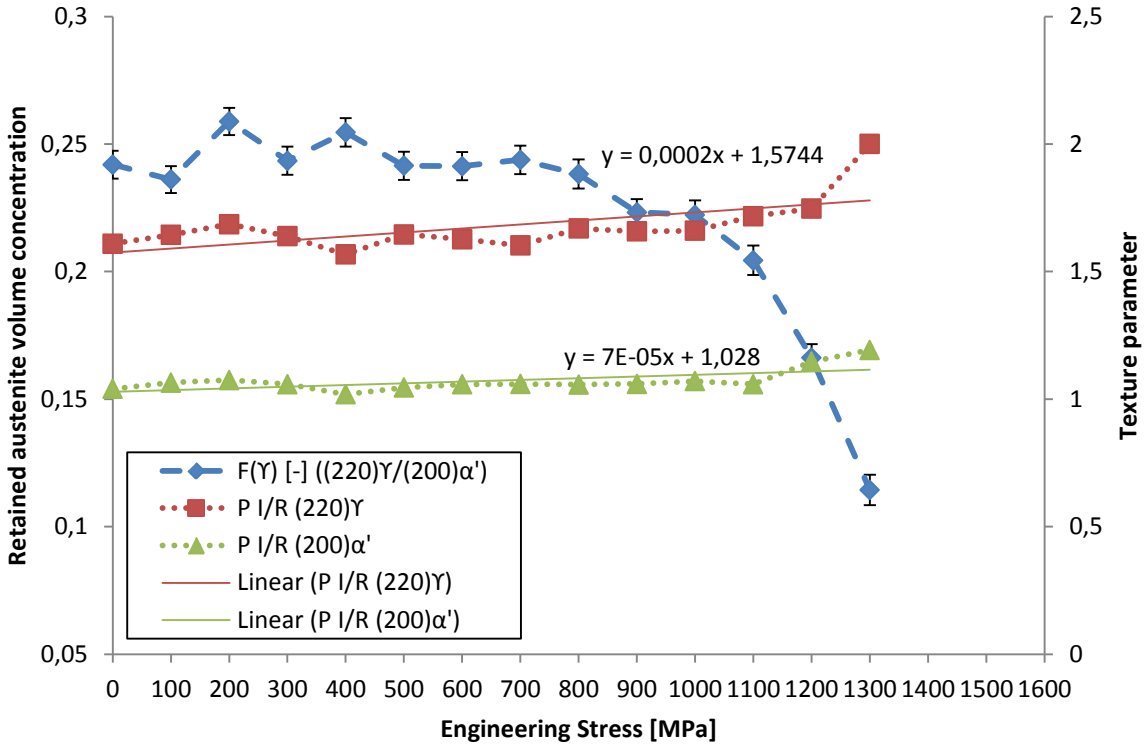

Figure D.5: RA volume fraction vs. texture parameter of C30-QT217-50

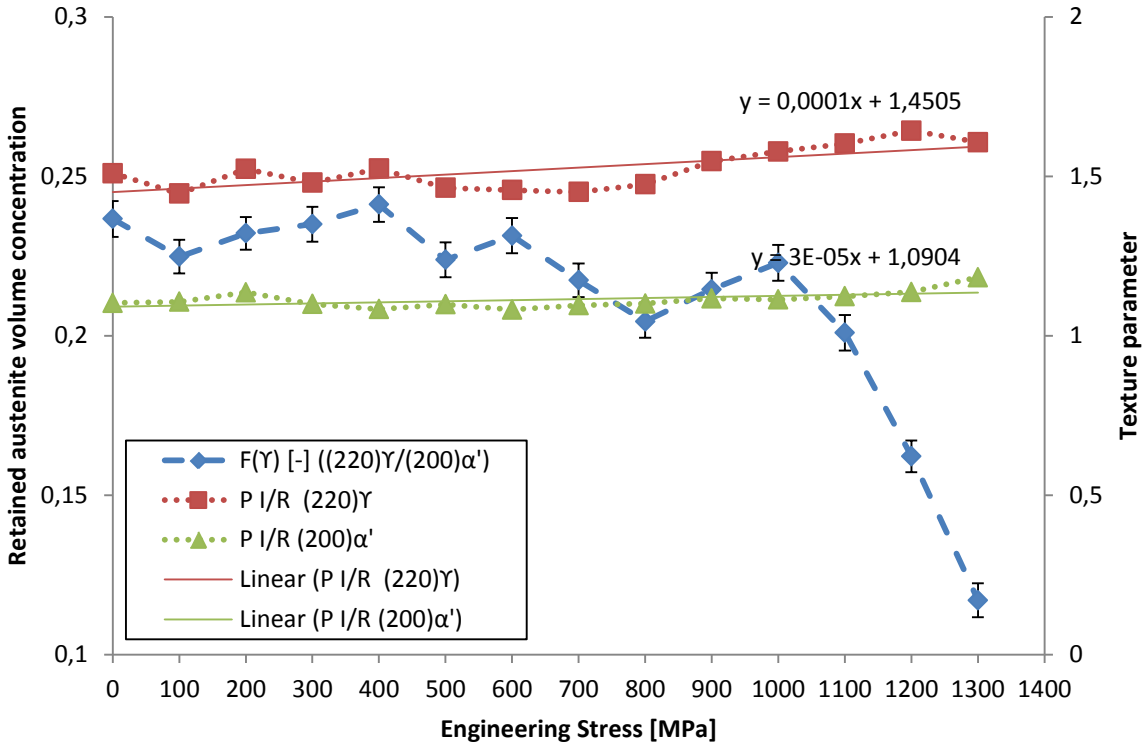

Figure D.6: RA volume fraction vs. texture parameter of C28-QT240

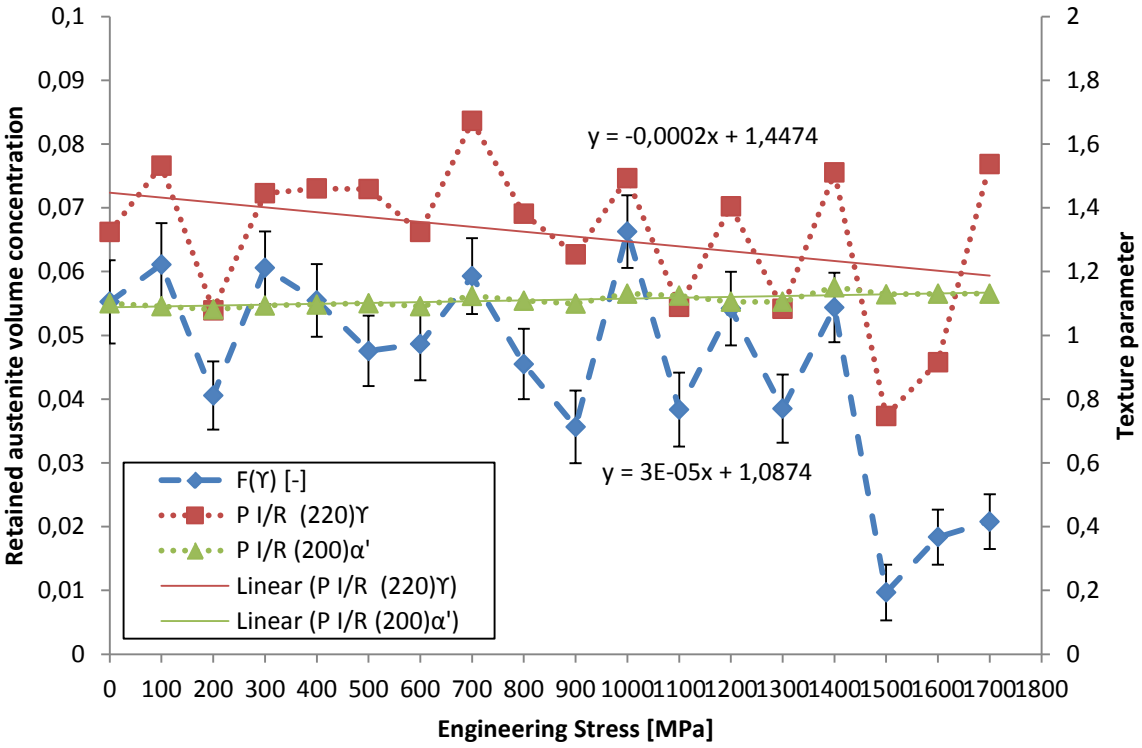

Figure D.7: RA volume fraction vs. texture parameter of C28-QT280

Appendix E. Young's modules regression line

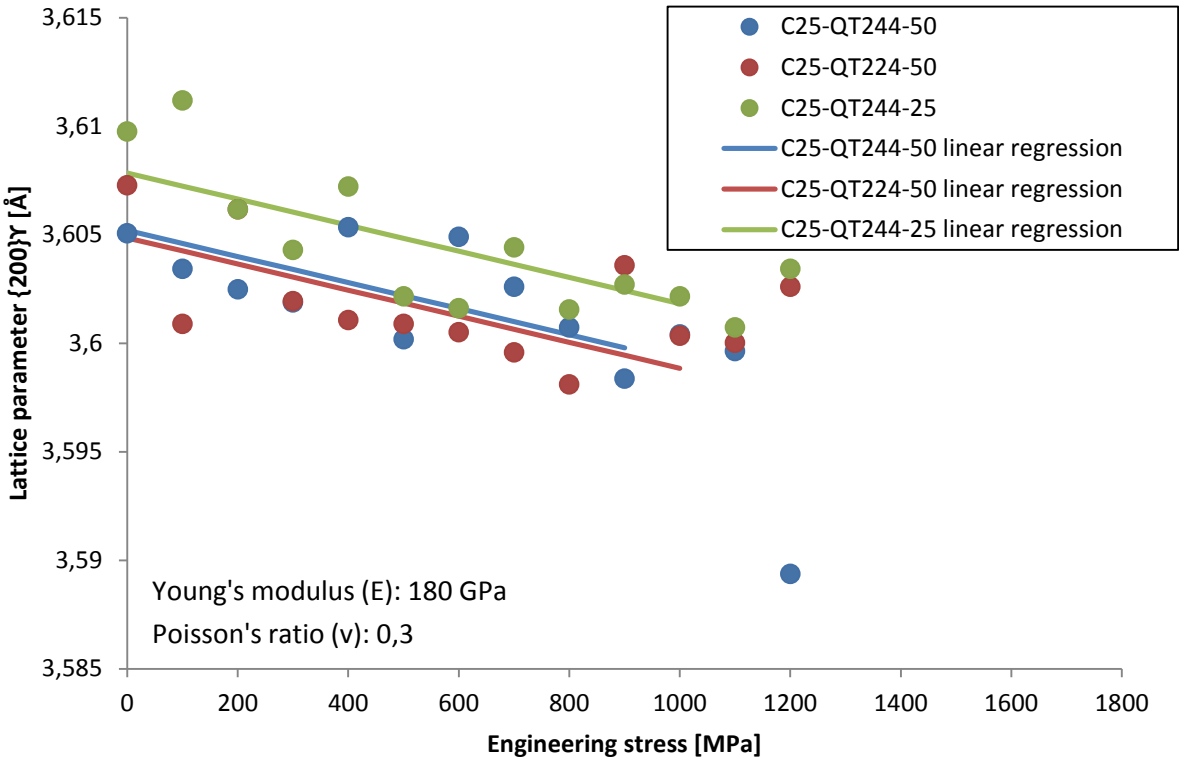

Figure E.1: Young modulus calculation of C25 material, $\{200\}_\gamma$ plane (fcc)

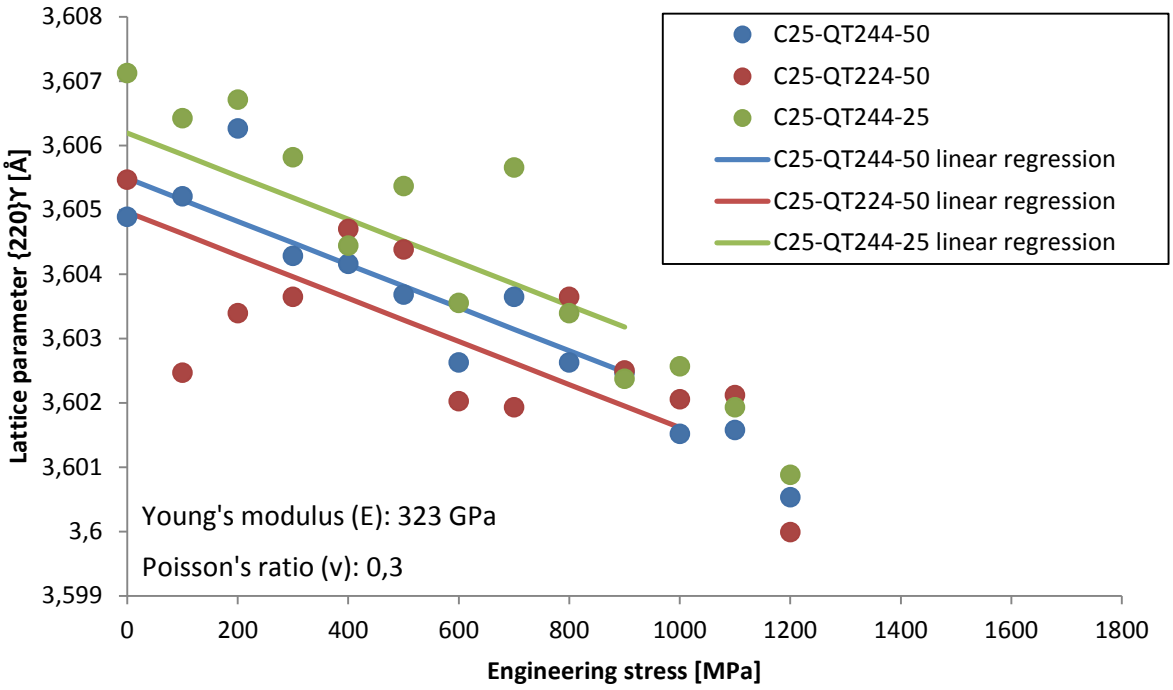

Figure E.2: Young modulus calculation of C25 material, $\{220\}_\gamma$ plane (fcc)

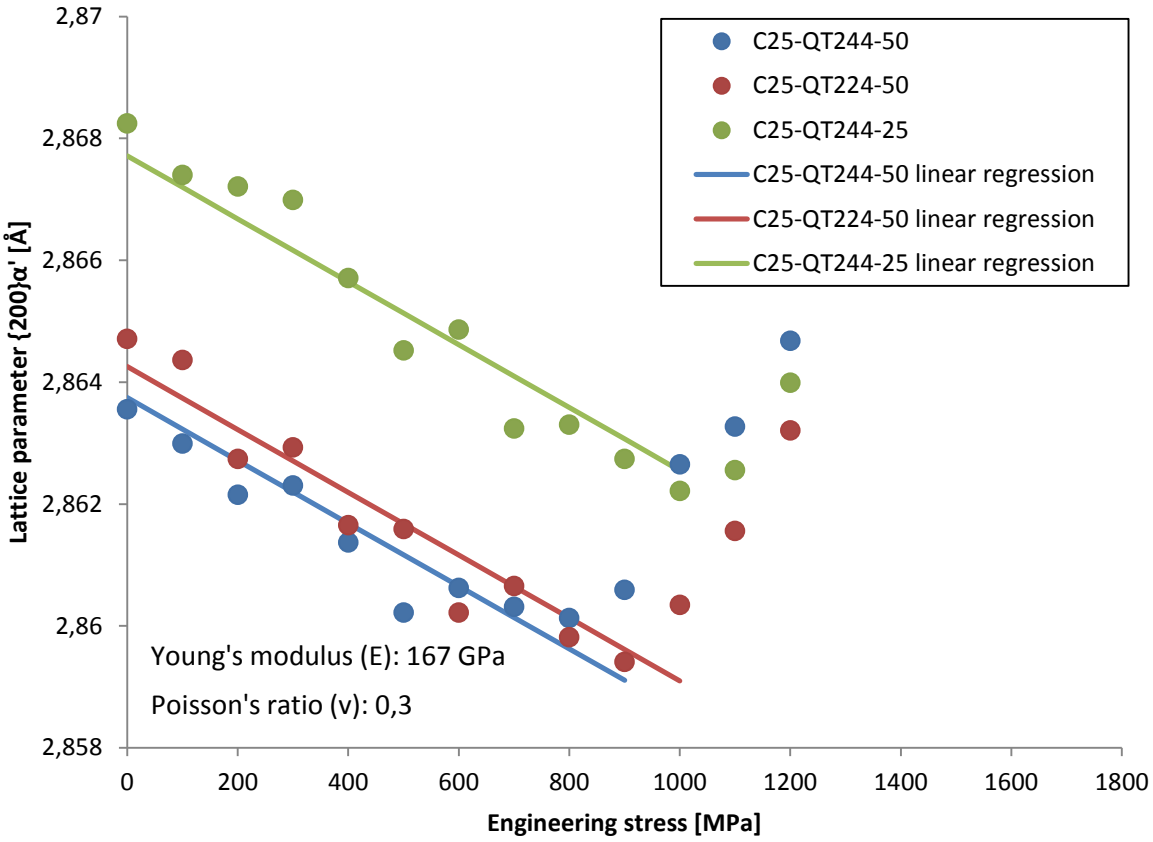

Figure E.3: Young modulus calculation of C25 material, $\{200\}_{\alpha'}$ plane (bcc)

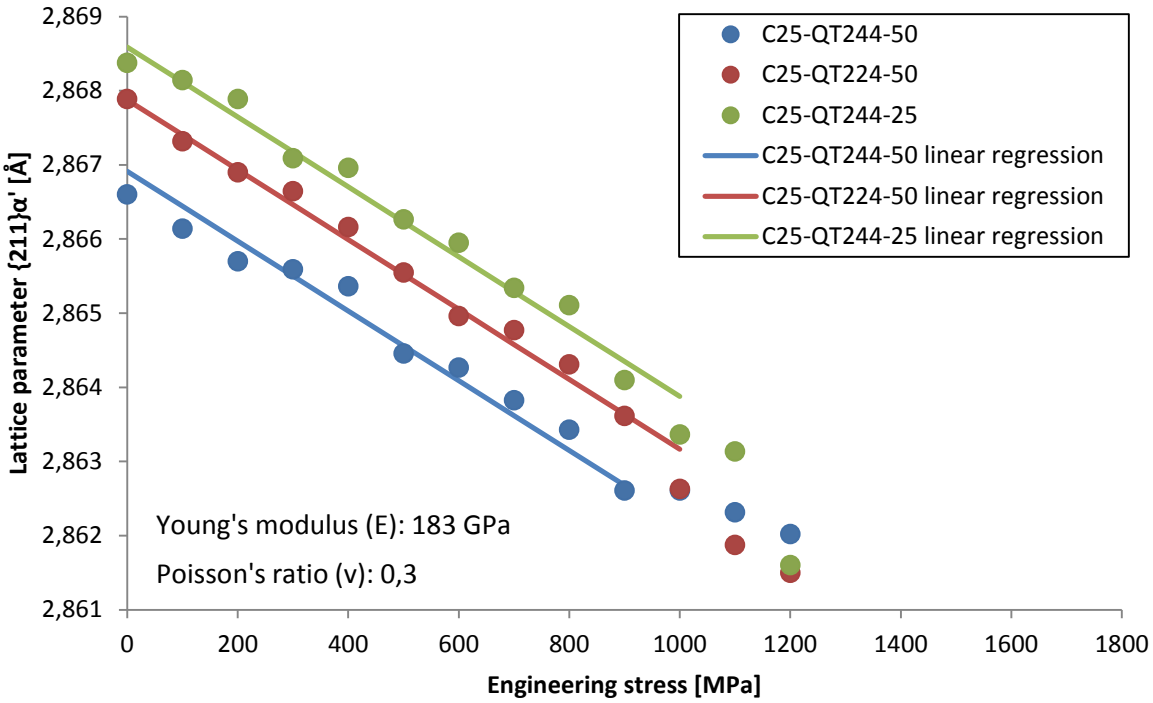

Figure E.4: Young modulus calculation of C25 material, $\{221\}_{\alpha'}$ plane (bcc)

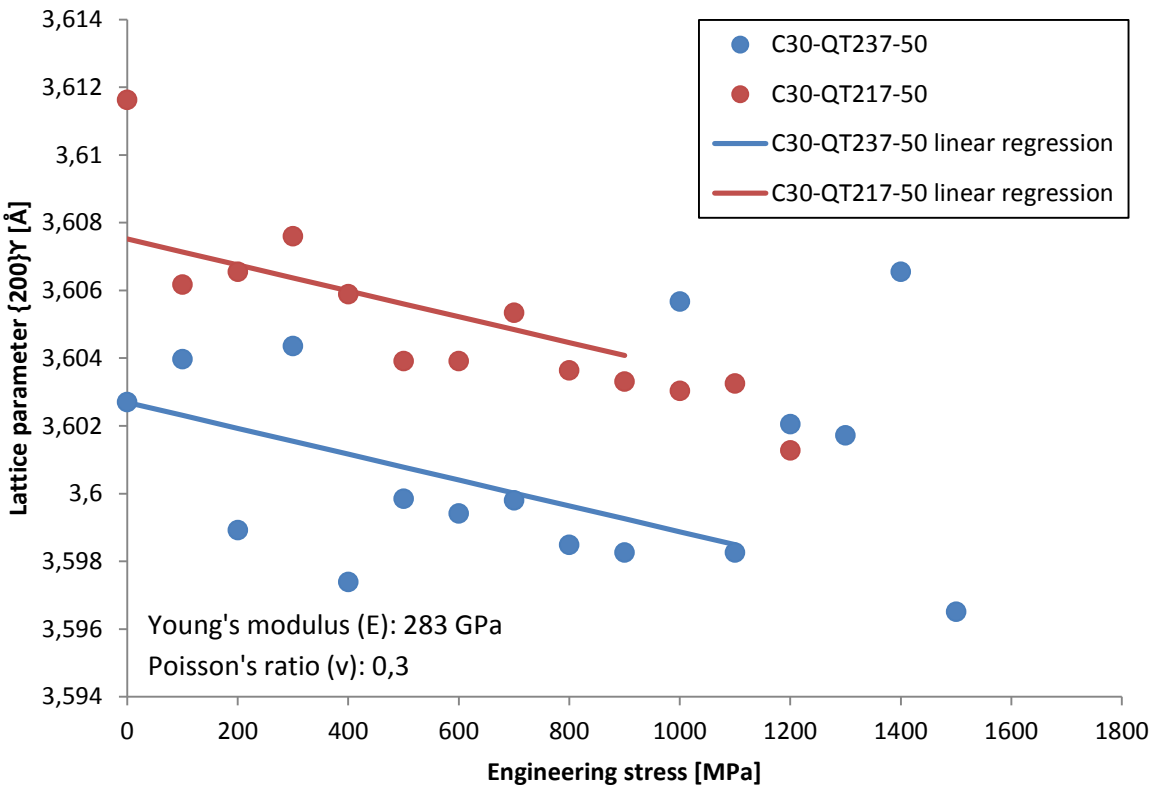

Figure E.5: Young modulus calculation of C30 material, $\{200\}_\gamma$ plane (fcc)

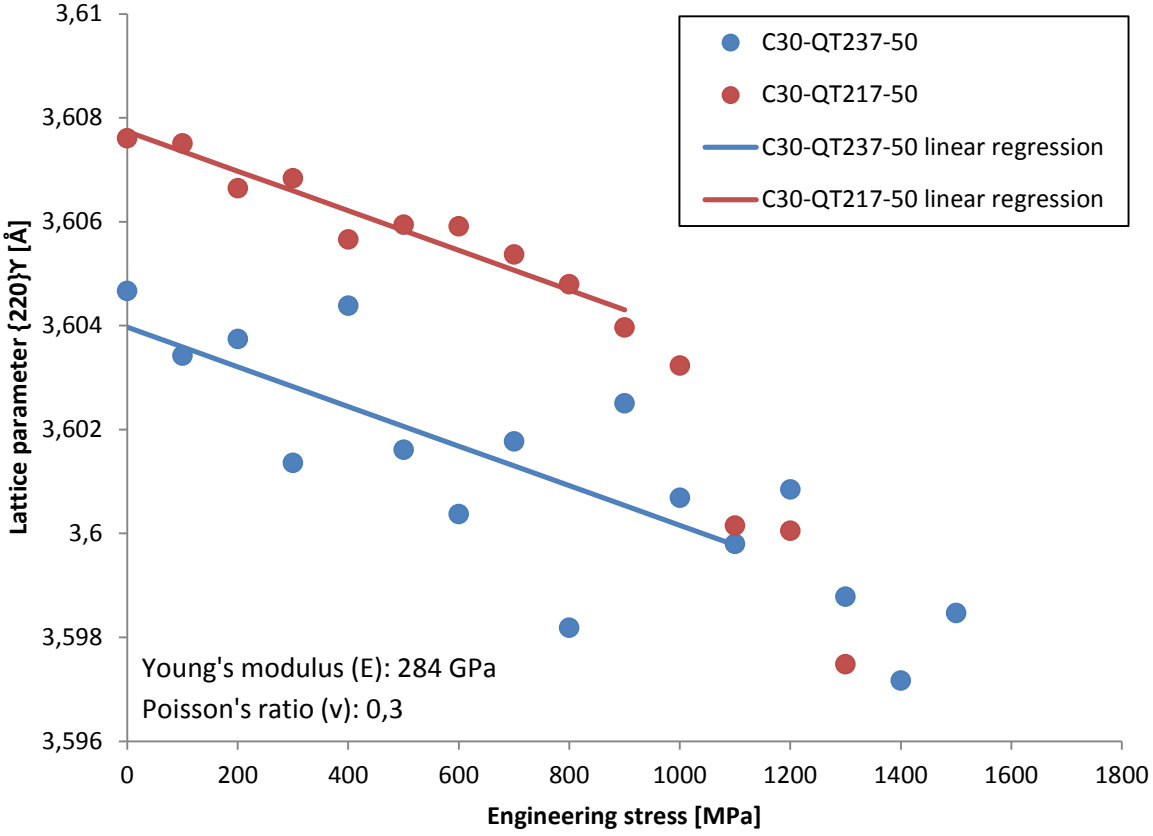

Figure E.6: Young modulus calculation of C30 material, $\{220\}_\gamma$ plane (fcc)

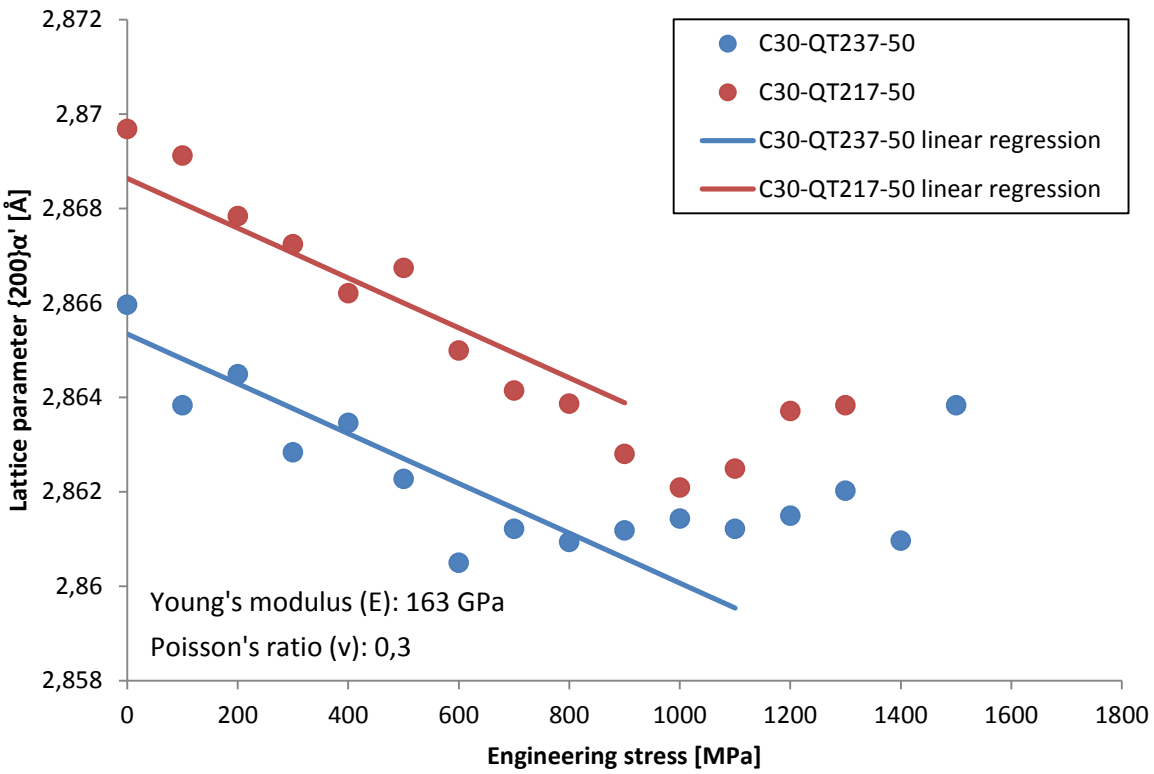

Figure E.7: Young modulus calculation of C30 material, $\{200\}_{\alpha'}$ plane (bcc)

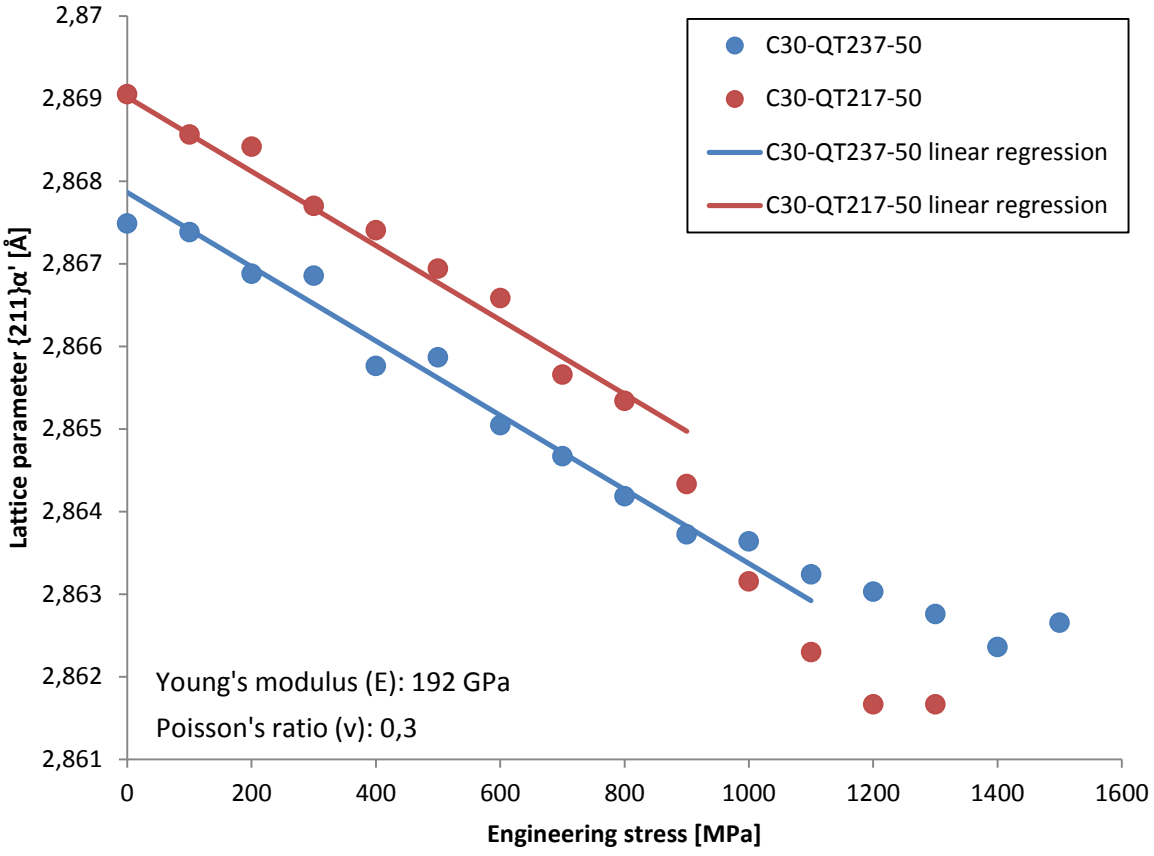

Figure E.8: Young modulus calculation of C30 material, $\{221\}_{\alpha'}$ plane (bcc)

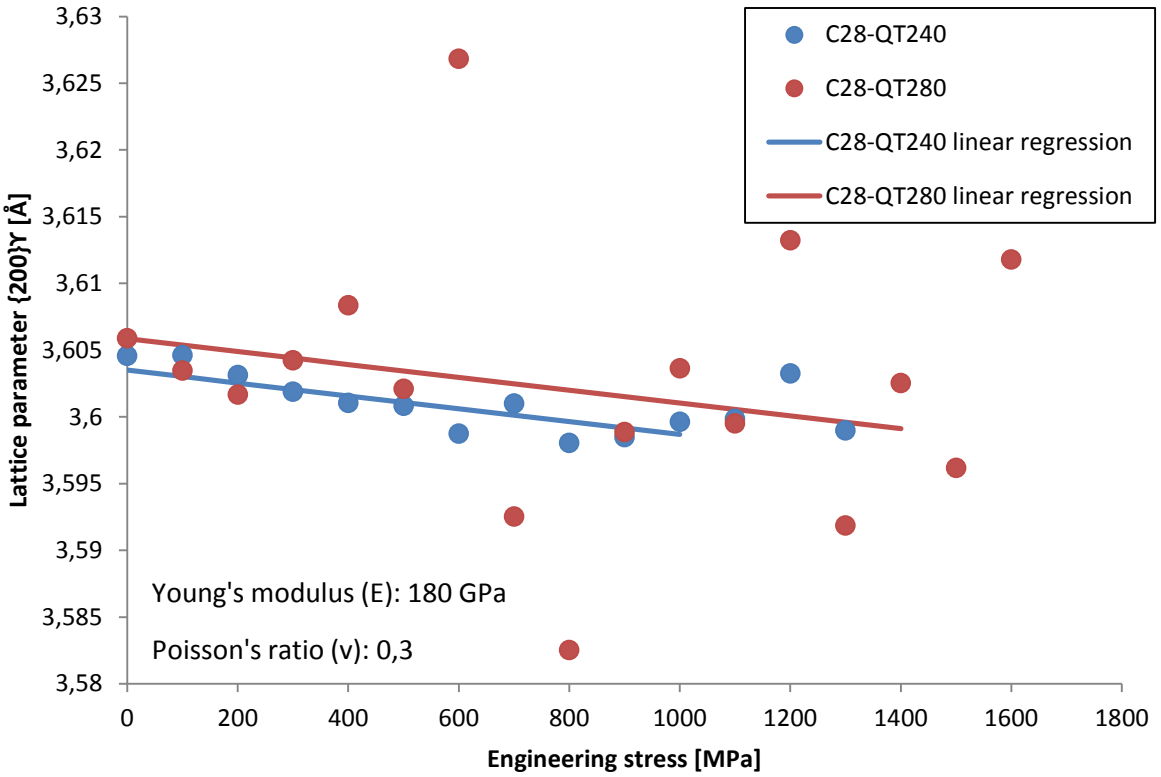

Figure E.9: Young modulus calculation of C28 material, $\{200\}_Y$ plane (fcc)

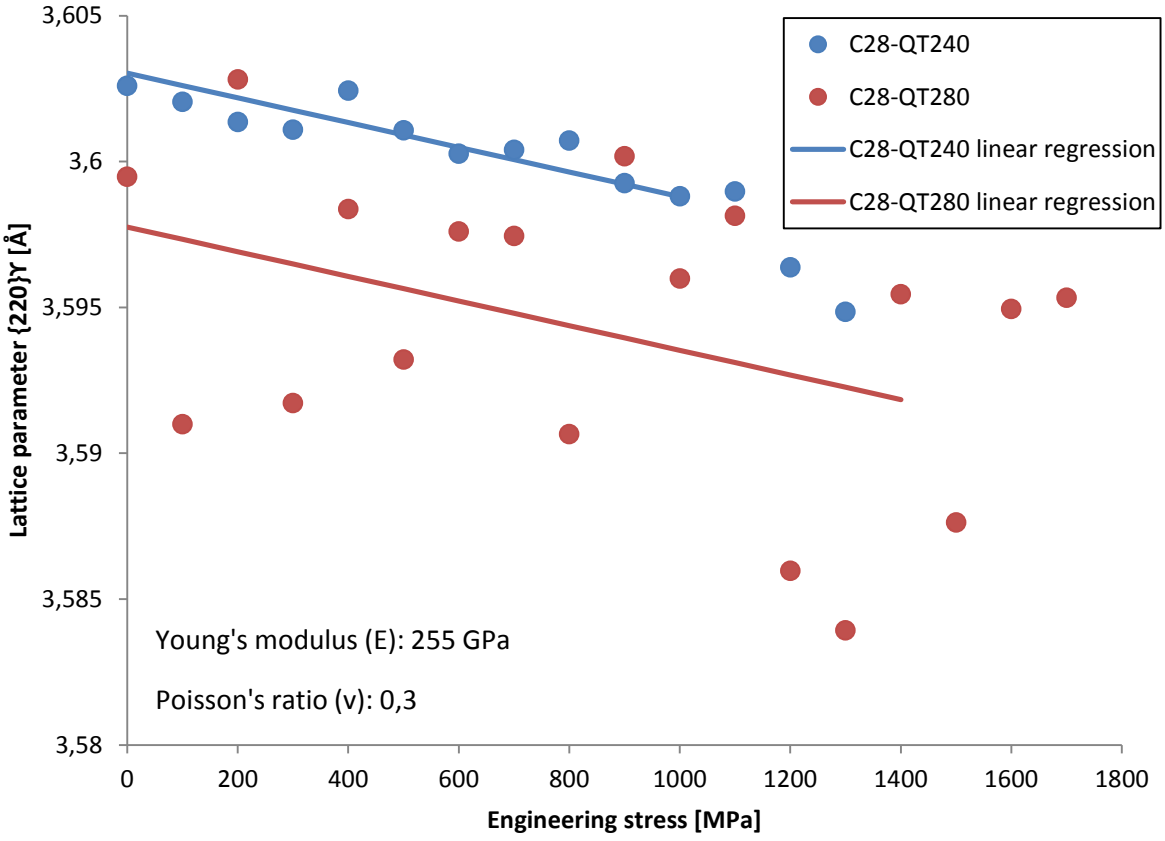

Figure E.10: Young modulus calculation of C28 material, $\{220\}_Y$ plane (fcc)

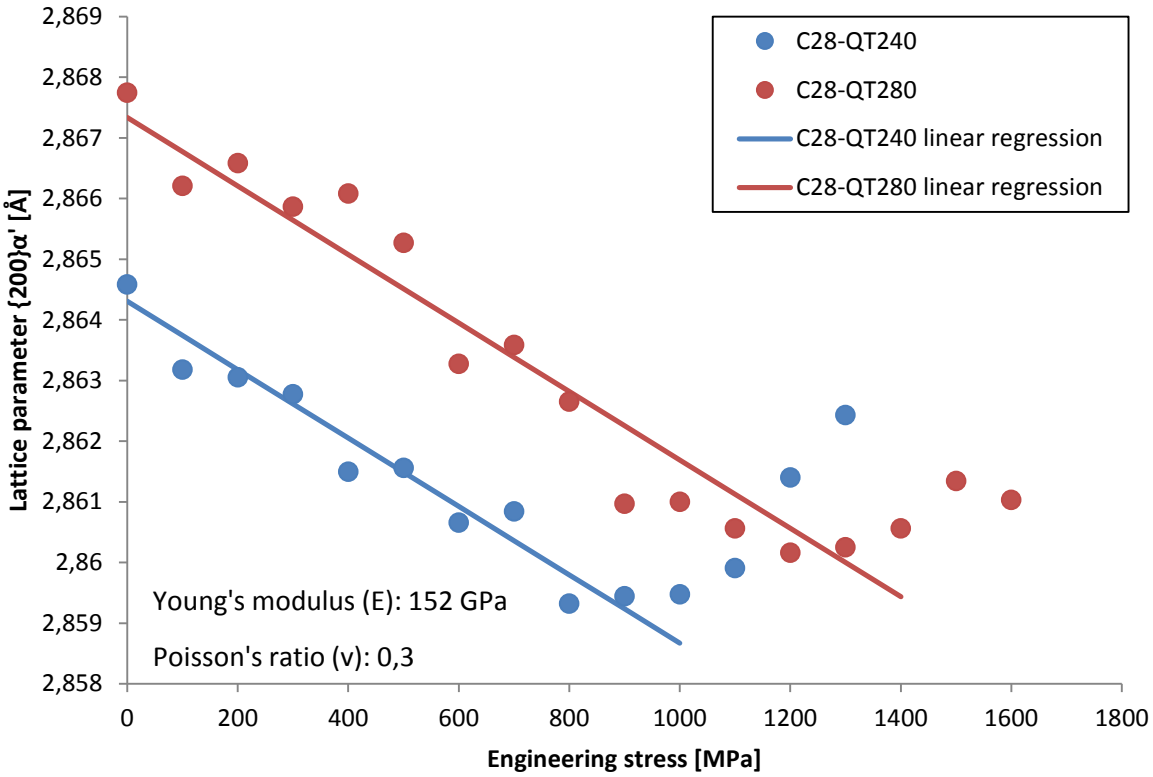

Figure E.11: Young modulus calculation of C28 material, $\{200\}_{\alpha'}$ plane (bcc)

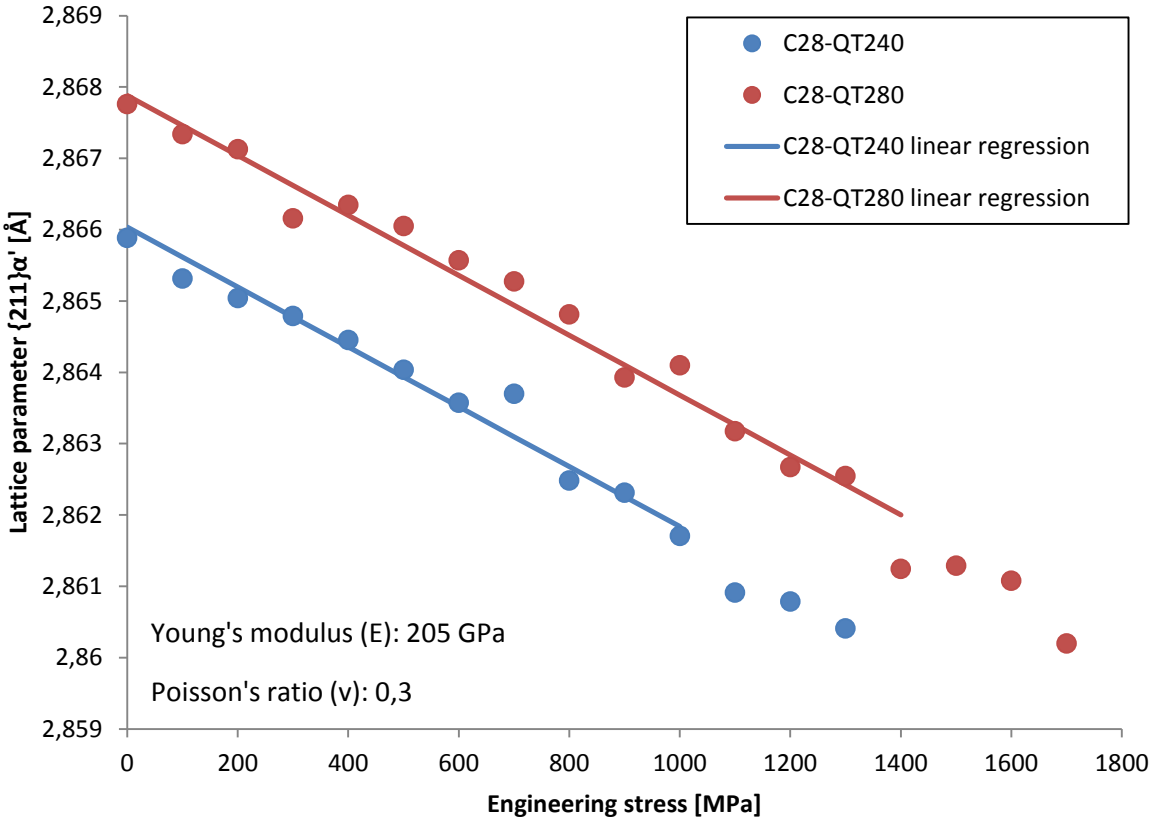

Figure E.12: Young modulus calculation of C28 material, $\{221\}_{\alpha'}$ plane (bcc)